

# **Statistical analysis of the spatial and temporal variability of polarimetric weather radar signals in the Alps**

**Thèse N° 7203**

**Présentée le 29 juillet 2019**

**à la Faculté de l'environnement naturel, architectural et construit  
Laboratoire de télédétection environnementale  
Programme doctoral en génie civil et environnement**

**pour l'obtention du grade de Docteur ès Sciences**

**par**

**Floortje Elisabeth Maria VAN DEN HEUVEL**

**Acceptée sur proposition du jury**

**Prof. F. Golay, président du jury  
Prof. A. Berne, Dr M. Gabella, directeurs de thèse  
Dr H. Leijnse, rapporteur  
Prof. E. Morin, rapporteuse  
Prof. P. Molnar, rapporteur**

**2019**





# Acknowledgements

Although a thesis features the name of a single author, it is actually built on the foundation of numerous scientific and non-scientific contributions from many different people. Some of whom I would like to mention explicitly here. First of all, this thesis gave me the opportunity to work in two amazing teams; the LTE laboratory at EPFL and MeteoSwiss in Locarno. I am therefore thankful to Bertrand Calpini and Urs Germann for their parts in setting up this wonderful collaboration. I thank my supervisors Alexis Berne and Marco Gabella, for their excellent guidance and for their unwavering confidence, support, kindness and patience. This thesis has allowed me to travel to many beautiful (outdoor) places, and I am immensely grateful for having had these opportunities as well as for the flexibility of my supervisors. Thanks to all my brilliant colleagues at LTE and MeteoSwiss for their help and advice, bits of code, participation in field campaigns and many coffee, lunch or beer breaks. I am particularly grateful to Jacopo Grazioli and Maurizio Sartori for sharing with me their knowledge of and experience with radar, to Loris Foresti, Nikola Besic and Daniele Nerini for their many insightful explanations and to Daniel Wolfensberger and Jordi Figueras i Ventura for their immensely helpful programs and code. Thanks to Alina and Denis for their invaluable technical support at LTE. I am grateful to my friends in the Netherlands, whose faithful friendship has withstood my frequent absences. And to my friends in Switzerland, especially Aline and Michel; EPFL would not have been the same without you! A very special thought, with love, goes to Victorine, for her love and support, for keeping me focused and for being there when I most need it. Finally, an immense thanks to my family for their love and encouragement; to my brother Pieter, my sister Marieke and my brother-in-law Roland. I am so very grateful to my parents, whose courage, optimism and perseverance will always be an inspiration to me.

*Lausanne, 1 July 2019*

F. v.d. H.

# Abstract

The accurate estimation of precipitation quantities arriving at the ground in complex terrain such as the Alps is complicated by many factors. The orography interacts with atmospheric flow and thus influences the spatial and temporal distribution as well as the microphysics of precipitation. Although weather radar can provide high-resolution measurements of precipitation, their view is sometimes blocked by the relief in which case measurements from higher altitudes need to be extrapolated to the ground level. When extrapolating the radar measurements aloft for quantitative precipitation estimation (QPE) at the ground, these must first be corrected for the vertical change of the radar echo caused by the growth and transformation of precipitation (VPR correction). Many existing operational algorithms for QPE and VPR correction assume the vertical structure of precipitation to be spatially and temporally homogeneous. However, given the variable nature of precipitation this assumption may not hold, especially in mountainous areas. This thesis aims to contribute to the improvement of QPE by radar in the Alps through the analysis of the spatio-temporal variability of the polarimetric radar signals. More specifically, this is done through contributions to questions on radar monitoring and stability, the characterisation of the spatio-temporal variability of the melting layer and the study of the potential for the inclusion of polarimetric radar variables in a more localised vertical profile correction approach. A method based on spectral analysis is used to provide some new perspectives on radar hardware monitoring using the polarimetric signals returned by a single bright scatterer. It is shown that valuable information on the state and stability of the radar hardware can be obtained if different scales of variability and several polarimetric variables are considered. The same approach is used for the characterisation and comparison of the spatio-temporal variability of the melting layer on the relatively flat Swiss plateau and in a large inner Alpine valley in the Swiss Alps. Based on the results of this study it appears that the smaller spatial scales contribute more to the total spatial variability of the melting layer in the case of the Alpine environment. Finally, building on the availability of polarimetric data and a hydrometeor classification algorithm, a new framework for the application of machine learning methods to study the vertical structure of precipitation in Switzerland as well as a more localised vertical profile correction method is proposed. It is shown that models which include information on hydrometeor proportions better represent the observed patterns of vertical change in precipitation and that these models can predict from altitudes between 500 to 1000 metres higher than models based on only reflectivity data.

Key words: QPE, polarimetric radar, spatio-temporal variability, remote sensing

## Résumé

L'estimation précise des quantités de précipitations arrivant au sol dans des régions avec une topographie complexe tels que les Alpes est compliquée par de nombreux facteurs. L'orographie interagit avec les flux atmosphériques et influence donc la distribution spatiale et temporelle ainsi que la microphysique des précipitations. Bien que les radars météorologiques puissent fournir des mesures à haute résolution des précipitations, leur visibilité est parfois bloquée par le relief, auquel cas les mesures prises à des altitudes plus élevées doivent être extrapolées au niveau du sol. Lorsqu'on extrapole les mesures radar d'altitude pour une estimation quantitative des précipitations (QPE) au sol, celles-ci doivent d'abord être corrigées pour tenir compte de la variation verticale de l'écho du radar causée par la croissance et la transformation des précipitations (correction VPR). De nombreux algorithmes opérationnels existants pour le QPE et la correction VPR supposent que la structure verticale des précipitations est homogène dans le temps et dans l'espace. Cependant, étant donné la nature variable des précipitations, cette hypothèse pourrait être remise en question, particulièrement dans des régions montagneuses. Ce thèse a pour objectif de contribuer à l'amélioration du QPE par radar dans les Alpes à travers l'analyse de la variabilité spatio-temporelle des signaux polarimétriques. Ceci a permis de contribuer aux questions relatives à la surveillance du radar, la caractérisation de la variabilité spatio-temporelle de la couche de fusion et l'étude du potentiel de l'inclusion des variables polarimétriques dans une approche plus localisée de correction du profil vertical. Une méthode basée sur l'analyse spectrale est utilisée afin de fournir de nouvelles perspectives sur la surveillance du radar hardware utilisant les signaux polarimétriques renvoyés par une seule cible de forte rétrodiffusion. Il est montré que des informations précieuses sur l'état et la stabilité du radar hardware peuvent être obtenues si différentes échelles de variabilité et plusieurs variables polarimétriques sont prises en compte. La même approche est utilisée pour la description et la comparaison de la variabilité spatio-temporelle de la couche de fusion sur le plateau suisse, peu accidenté, et dans une grande vallée intra-alpine. D'après les résultats de cette étude, les plus petites échelles spatiales contribuent davantage à la variabilité spatiale totale de la couche de fusion en environnement alpin. Enfin, tirant profit de la disponibilité des données polarimétriques ainsi que d'un algorithme de classification des hydrométéores, un cadre pour l'application de méthodes d'apprentissage automatique permettant d'étudier la structure verticale des précipitations et une méthode de correction de profil vertical plus localisée sont proposées. Il est montré que les modèles qui incluent des informations sur les proportions des hydrométéores représentent mieux les tendances de changement vertical des précipitations observées et qu'ils peuvent fournir des

## Résumé

---

prédictions depuis des altitudes variant entre 500 à 1000 mètres supérieures aux modèles basés uniquement sur des données de réflectivité.

Mots clefs : estimations quantitatives des précipitations, radar polarimétrique, variabilité spatio-temporelle, télédétection

# Samenvatting

De nauwkeurige schatting van de hoeveelheid neerslag die op de grond valt in regio's met een gevarieerd reliëf zoals de Alpen wordt gecompliceerd door vele factoren. Door hun effect op atmosferische luchtstromingen beïnvloeden bergen de ruimtelijke en temporele verdeling evenals de microfysica van neerslag. Hoewel weerradars neerslag metingen met hoge resolutie kunnen bieden, wordt hun zicht soms geblokkeerd door het reliëf in welk geval de metingen van grotere hoogtes naar het grondniveau moeten worden geëxtrapoleerd. Bij het extrapoleren van de radarmetingen van bovenaf voor kwantitatieve neerslag schatting (QPE) op de grond, moeten deze eerst worden gecorrigeerd voor de verticale verandering van de radarecho als gevolg van de groei en transformatie van neerslag (VPR correctie). Veel bestaande algoritmes voor QPE en VPR correctie nemen aan dat de verticale structuur van neerslag spatieel en temporeel homogeen is. Gezien de variabele aard van neerslag kan deze veronderstelling echter niet altijd en overal geldig zijn, en in het bijzonder niet in bergachtige gebieden. Dit proefschrift heeft als doel bij te dragen aan de verbetering van neerslag schattingen door weerradar in de Alpen door middel van de analyse van de spatio-temporele variabiliteit van de polarimetrische radarsignalen. Dit wordt gedaan door middel van bijdragen aan kwesties omtrent het monitoren van de stabiliteit van radar hardware en de karakterisering van de spatio-temporele variabiliteit van de smeltlaag en door een studie van het potentieel van polarimetrische radar variabelen in een meer gelokaliseerde methode voor verticale profiel correctie. Een methode op basis van spectrale analyse van de polarimetrische signalen die worden geretourneerd door één enkel helder doelwit, wordt gebruikt om een aantal nieuwe perspectieven te bieden op het gebied van radar hardware monitoring. Er wordt aangetoond dat waardevolle informatie over de toestand en stabiliteit van de radar hardware kan worden verkregen als verschillende schalen van variabiliteit en verschillende polarimetrische variabelen in acht worden genomen. Dezelfde techniek wordt gebruikt voor de karakterisering en vergelijking van de spatio-temporele variabiliteit van de smeltlaag op het relatief platte Zwitserse plateau en in een breed dal in de Zwitserse Alpen. Op basis van de resultaten van dit onderzoek lijkt het erop dat de kleinere spatiële schalen meer bijdragen aan de totale ruimtelijke variabiliteit van de smeltlaag in het bergachtige gebied. Ten slotte wordt, voortbouwend op de beschikbaarheid van polarimetrische variabelen en een algoritme voor de classificatie van hydrometeoren, een nieuw raamwerk voor de toepassing van kunstmatige intelligentie voor het bestuderen van de verticale structuur van neerslag in Zwitserland evenals een meer gelokaliseerde methode voor verticale profiel correctie gepresenteerd. Het wordt aangetoond dat modellen die informatie bevatten over proporties van hydrometeoren de waargenomen

## **Samenvatting**

---

patronen van verticale verandering in neerslag beter weergeven en dat deze modellen kunnen voorspellen vanaf hoogtes tussen 500 tot 1000 meter hoger dan modellen op basis van alleen reflectiviteit.

Sleutelwoorden: Kwantitatieve neerslag schatting, polarimetrische radar, spatio-temporele variabiliteit, teledetectie

# Contents

<b>Acknowledgements</b>	<b>i</b>
<b>Abstract (English/Français/Nederlands)</b>	<b>ii</b>
<b>Contents</b>	<b>vii</b>
<b>List of important symbols</b>	<b>ix</b>
<b>List of important acronyms</b>	<b>xi</b>
<b>List of figures</b>	<b>xiii</b>
<b>List of tables</b>	<b>xvii</b>
<b>1 Quantitative precipitation estimation in an Alpine context</b>	<b>1</b>
1.1 Measurement of precipitation by polarimetric weather radar . . . . .	3
1.1.1 A short overview of radar hardware . . . . .	3
1.1.2 Basic radar measurements and the radar equation . . . . .	5
1.1.3 Polarimetric radar observables . . . . .	9
1.1.4 Relating reflectivity to rain rate . . . . .	12
1.1.5 Relating polarimetric variables to hydrometeor classes . . . . .	13
1.1.6 Polarimetric variables and the Melting Layer (ML) . . . . .	13
1.2 Vertical profile correction . . . . .	14
1.3 Building tools for the analysis of the spatio-temporal variability of radar data .	17
1.3.1 Development of a spatial data base and tools . . . . .	17
1.3.2 Spectral analysis and the fraction of variance explained by component .	19
1.4 Thesis outline . . . . .	22
<b>2 Temporal monitoring of dual-polarisation weather radar</b>	<b>25</b>
2.1 Summary . . . . .	26
2.2 Introduction . . . . .	27
2.3 Data and Methods . . . . .	29
2.3.1 Fractions of variance explained by component . . . . .	32
2.4 Data analysis and results . . . . .	34
2.4.1 Event and sub-daily variability . . . . .	35

## Contents

---

2.4.2	Typical scales of variability . . . . .	38
2.5	Discussion . . . . .	44
2.5.1	Possible correction of the diurnal cycle . . . . .	47
2.6	Conclusions . . . . .	48
<b>3</b>	<b>Characterisation of the melting layer variability</b>	<b>51</b>
3.1	Summary . . . . .	52
3.2	Introduction . . . . .	53
3.3	Dataset description . . . . .	55
3.3.1	Data PaRaDIso campaign . . . . .	55
3.3.2	Valais 2016-2017 campaign . . . . .	57
3.4	Methodology . . . . .	59
3.4.1	Pre-processing . . . . .	59
3.4.2	Calculation of the power spectra of melting layer variables . . . . .	60
3.5	Results . . . . .	62
3.5.1	Evaluation of the method . . . . .	62
3.5.2	Melting layer statistics . . . . .	64
3.5.3	Spatial variability . . . . .	67
3.5.4	Spatio-temporal coherence of the melting layer variability . . . . .	70
3.6	Conclusions . . . . .	73
<b>4</b>	<b>Learning about the vertical structure of radar reflectivity</b>	<b>74</b>
4.1	Summary . . . . .	75
4.2	Introduction . . . . .	76
4.3	The vertical cone database . . . . .	77
4.3.1	Radar data pre-processing . . . . .	77
4.3.2	Vertical cone extraction . . . . .	78
4.3.3	Selection of precipitation events . . . . .	81
4.4	Neural network and experimental setup . . . . .	81
4.5	Exploratory data analysis and results . . . . .	84
4.5.1	EDA: Vertical profiles of hydrometeor proportions . . . . .	84
4.5.2	Results: ANN predictions of growth and decay . . . . .	85
4.6	Conclusions . . . . .	96
<b>5</b>	<b>Conclusions and outlook</b>	<b>98</b>
5.1	Summary . . . . .	98
5.2	Contribution of this thesis . . . . .	99
5.3	Perspectives . . . . .	100
<b>A</b>	<b>Calculation of refractivity</b>	<b>103</b>
	<b>Bibliography</b>	<b>116</b>
	<b>Curriculum Vitae</b>	



# List of important symbols

Symbol	Units	Description
$a$	$[\text{kg mm}^{-b}]$	Intercept in the power-law mass-diameter relation
$\mathbf{A}$		Array of spatial or temporal measurements
$b$	$[-]$	Exponent in the power-law mass-diameter relation
$c$	$[\text{ms}^{-1}]$	Speed of light
$C_r$	$[-]$	Radar constant
$D$	$[\text{mm}]$	Particle diameter (or reference size)
$E_A(n_c)$		Discrete spectral energy of $\mathbf{A}$ for frequency $n_c$
$\mathbf{F}_A(n_c)$		Complex Fourier transform of $\mathbf{A}$ for frequency $n_c$
$f$	$[\text{Hz}]$	Frequency
$f_n$	$[\text{Hz}]$	Nyquist frequency
$f_r$	$[\text{Hz}]$	Pulse repetition frequency
$f_t$	$[\text{Hz}]$	Frequency shift caused by a moving target
$G$	$[-]$	Radar gain
$h$	$[\text{m}]$	Altitude above sea level
$h_b$	$[\text{m}]$	Altitude above sea level vertical cone base
$h_p$	$[\text{m}]$	Pulse length
$ K ^2$	$[-]$	Dielectric constant of scatterers
$K_{dp}$	$^{\circ} \text{ km}^{-1}$	Specific differential phase shift upon propagation
$n$	$[-]$	Refractive index of the atmosphere
$n_c$		Frequency $n_c$ of $N$ frequencies
$N(D)$	$[\text{mm}^{-1} \text{m}^{-3}]$	Drop size distribution or particle size distribution
$n_f$	$[\text{Hz}]$	Index $n_c$ of Nyquist frequency $f_n$
$o_i$		Output of neural network neuron $i$
$P$	$[\text{W}]$ or $[\text{mW}]$	Power
$P_t$	$[\text{W}]$ or $[\text{mW}]$	Power transmitted by a radar
$P_r$	$[\text{W}]$ or $[\text{mW}]$	Power received by a radar
$r$	$[\text{m}]$ or $[\text{km}]$	Range distance
$r_{max}$	$[\text{m}]$	Maximum unambiguous range
$r_a$	$[\text{m}]$	Radius
$s_{hh}$	$[\text{m}]$ or $[\text{cm}]$	Complex backscattering amplitude, horizontal polarisation

## Contents

---

$s_i$		Input signal of neural network neuron $i$
$\mathbf{S}_A(n_c)$		Spectral energy density of $A$ for frequency $n_c$
$V$	[m <sup>3</sup> ]	Radar resolution volume
$V_{\text{rad}}$	[m s <sup>-1</sup> ]	Radial velocity of targets
$\mathbf{w}$	[-]	Neural Network weights
$\mathbf{W}$	[-]	Belltaper window height
$Z_{DR}$	[dB]	Differential reflectivity
$Z_e$	[dBZ] or [mm <sup>6</sup> m <sup>-3</sup> ]	Radar reflectivity factor
$Z_h$	[mm <sup>6</sup> m <sup>-3</sup> ]	Horizontal reflectivity factor
$Z_H$	[dBZ]	Horizontal reflectivity factor
$\beta$	[-]	(Spectral) slope
$\delta_{co}$	[°]	Backscattering phase delay
$\eta$	[m <sup>-1</sup> ]	Radar reflectivity
$\theta_{3dB}$	[°]	3dB beamwidth of the radar antenna (elevation)
$\lambda$	[m] or [cm] or [mm]	Wavelength or radar wavelength
$\rho$		Correlation coefficient
$\rho_{HV}$	[-]	Copolar correlation coefficient
$\sigma^2$		Variance
$\sigma^b$	[m <sup>2</sup> ] or [cm <sup>2</sup> ]	Radar backscattering cross section
$\tau$	[s]	Pulse duration
$\phi$	[rad]	Phase of an EM wave
$\phi_{dp}$	[°]	Differential phase shift upon propagation
$\phi_{3dB}$	[°]	3dB beamwidth of the radar antenna (azimuth)
$\Psi_{dp}$	[°]	Total differential phase shift
$\Omega$	[rad s <sup>-1</sup> ]	Angular frequency

# List of important acronyms

Acronym	Description
AG	Aggregates (hydrometeor type)
ANN	Artificial Neural Network
CR	Ice Crystals (hydrometeor type)
DPP	Dual Pulse Pair (mode)
DX50	Mobile X-band radar
EDA	Exploratory Data Analysis
FFT	Fast Fourier Transform
GD	Growth and Decay (of precipitation)
GIS	Geographic Information System
GWT	GrossWetterTypes
HC	Hydrometeor Class
IF	Intermediate Frequency
ITSG	Internal Test Signal Generator
LDR	Linear Depolarisation Ratio
LNA	Low Noise Amplifier
LO	Local Oscillator Frequency
LR	Light Rain (hydrometeor type)
LTE	Laboratoire de Télédétection Environnementale
ML	Melting Layer
MLA	Machine Learning Algorithm
MLP	MultiLayer Perceptron
MXPol	Mobile X-band Polarimetric
NC	No Classification (hydrometeor classification type)
NMHS	National Meteorological and Hydrological Service
NWP	Numerical Weather Prediction
PaRaDIso	PAyerne RADar and ISOtopes
PPI	Plan Position Indicator (scan)
PRF	Pulse Repetition Frequency
QPE	Quantitative Precipitation Estimation
radar	radio detection and ranging

## Contents

---

RCB	Radar Control Card
RCS	Radar Cross Section
RF	Radio Frequency
RHI	Range-Height Indicator (scans)
RMSE	Root Mean Squared Error
RN	Rain (hydrometeor type)
RP	Rimed Particles (hydrometeor type)
SNR	Signal-to-Noise Ratio
SwissMetNet	Swiss Meteorological (ground) Network
TR	Transmit / Receive (switch)
VI	Vertically-oriented ice crystals (hydrometeor type)
VPR	Vertical Profile of Reflectivity
WS	Wet Snow (hydrometeor type)
WGS84	World Geodetic System 1984

# List of Figures

1.1	AMR-radar system block diagram taken from <a href="#">Vollbracht et al. (2014)</a> . . . . .	3
1.2	Illustration of the electric field of oscillation at horizontal (blue) and vertical (red) polarisation. . . . .	10
1.3	Schematic illustration of a radar measuring above the melting layer (left) and an idealised vertical profile of reflectivity in stratiform precipitation (right) at close (black curve) and further ranges (grey curves) from the radar. . . . .	14
1.4	A schematic overview of the interactions between the spatial data base and the toolboxes. . . . .	18
1.5	Challenges and processes related to precipitation in mountainous regions and the contributions of the individual chapters. . . . .	23
2.1	The location of the Cimetta tower (a) and its immediate surroundings (b). The blue line indicates the azimuth of the center of the radar bin under study and the red lines indicate the ranges. . . . .	30
2.2	Theoretical path of the center of the beam (-0.2 degrees elevation) for normal propagation conditions (orange line), with the 3 dB beam width in shaded orange. The blue line gives the top of the 3 dB beam (0.3 degrees elevation) under sub refractive conditions and the red line the bottom of the 3 dB beam (-0.7 degrees elevation) under super refractive conditions. . . . .	32
2.3	Top: fraction of variance explained by component for example signals. Bottom: folded spectra of the same signals. . . . .	34
2.4	Violin plots for $Z_{DR}$ (top panel) and $Z_H/Z_V$ (bottom panel) on an event basis. Boxplots of the combined $Z_H/Z_V$ data are represented in black inside the violin plots with a white dot indicating the median value, the box indicating the interquartile range (IQR) and the black lines representing the whiskers extending towards 1.5*IQR. . . . .	35
2.5	Violin plots for events (top to bottom), $Z_{DR}$ , $Z_V/Z_H$ (left to right) and specific time periods (x-axes). . . . .	37
2.6	Stem plots of the amounts of variance in the $Z_{DR}$ (top) $Z_H$ (middle) and $Z_V$ (bottom) measurements explained by each temporal lag, for all of the events. . . . .	39

## List of Figures

---

2.7	Timeseries of $Z_{DR}$ , $Z_V$ , $CAL_{dr}$ signal, Outside temperature and $\rho_{HV}$ for 6-9 March 2015, 18-21 January 2017 and 25-28 January 2017. The outside temperature values for the March time series had a constant bias and have been corrected with values from a nearby station. . . . .	40
2.8	Stem plots of the fractions of variance explained for all of the signals under study, for all of the selected events. . . . .	43
2.9	Calculated refractivity time series (left) and their corresponding fraction of variance explained by component (right). . . . .	46
2.10	Variance explained by each temporal lag for original and corrected $Z_{DR}$ time series for the January 2017 events (top) and the time series for the corrected $Z_{DR}$ (bottom). . . . .	48
3.1	Locations of the study areas (Payerne and Martigny) within Switzerland (top left panel) and the scan directions for the RHI scans during the Valais campaign (lower left panel). . . . .	56
3.2	Meteorological conditions in Payerne during the campaign compared to climatology; with the average number of days with precipitation for each month (left panel), the number of retained scans with a detected melting layer (middle panel) and a climatogram (right panel). . . . .	57
3.3	Meteorological conditions in Sion (~20 km from MXPOL) during the campaign compared to climatology; with the average number of days with precipitation for each month (left panel), the number of retained scans with a detected melting layer (middle panel) and a climatogram (right panel). . . . .	59
3.4	Melting layer detection algorithm output superimposed on the reflectivity values (left upper panel) and on copolar correlation coefficient values (left lower panel) and the extracted and derived variables (right) indicated for an idealised vertical profile of reflectivity (VPR). The bending of the melting layer towards the ground is probably related to the trapping of cold air in the valley and the observed negative temperature gradient towards the East (in the direction of the scan). . . . .	61
3.5	Examples of observed melting layer tops (a), their corresponding fractions of variance explained by component (b), the cumulated fractions of variance explained (c) and one original melting layer with the reconstituted melting layer from the first ten components (d) from the Valais campaign (green), from the Payerne campaign (red) and for a constructed melting layer consisting of white noise with a drift (blue). The vertical dashed line in panel c indicates the location of the scaling break at wavelengths of 500 m and the horizontal dashed line indicates the location where 50% or more of the total variance is explained. . . . .	63
3.6	Box plots illustrating the effects of median filtering, de-trending and tapering on the original melting layer tops for Payerne data (purple) and Valais data (green). . . . .	64
3.7	Distributions of the characteristic melting layer variables. . . . .	66

3.8	Fractions of variance explained by component for the melting layer tops (left panel) and the melting layer depths (right panel) for the DX50 (red), MXPOL in Payerne (purple) and MXPOL in the Valais (green) (fractions of individual melting layers have been binned based on their corresponding frequency values). . . .	67
3.9	Distribution of the binned spatial component with the highest fraction of explained variance per scan for the DX50 (red), MXPOL in Payerne (purple) and MXPOL in the Valais (green). . . . .	68
3.10	Parallel coordinates plots illustrating the intra and inter event variability of the fractions of variance explained by component of the melting layer tops, for the MXPOL in Payerne (top panel) and the MXPOL in the Valais (bottom panel); highlighted for a single event (number 7, indicated in pink on the first y-axis, and event lines are orange for Payerne and yellow for Valais) and highlighted for 10% of the explained variance for the second component (indicated in pink on the third y-axis). . . . .	69
3.11	Box plots of the fractions of variance explained by component (binned) for the melting layer tops of the selected events for MXPOL data in Payerne (left panel) and MXPOL data in the Valais (right panel). Spatial components are in purple and green and temporal components are in orange for the Payerne data and in hues of red for the Valais data to distinguish the different time periods of 1, 2 and 3 hours. . . . .	71
3.12	Box plots of the fractions of variance explained by component (binned) for the ten transects extracted from the DEM data in the direction of the RHI scans ( $\pm 5$ degrees azimuth) with in the right hand panels the first and last transect of the DEM in clockwise direction (measurement direction $-5^\circ$ and measurement direction $+5^\circ$ azimuth). . . . .	72
4.1	Location of the Albis radar within Switzerland and the regular grid for the vertical cone extraction. . . . .	77
4.2	Cones are extracted in well-visible regions of the radar and used to train the ANN. The trained ANN model can then be used to extrapolate to the ground level in regions with reduced visibility. . . . .	79
4.3	Example of a multi-input single-output MLP model and set-up as used in this study. The number of input variables $M$ equals the number of $V$ variables (reflectivity, HC proportions) $\times H$ height levels used. . . . .	82
4.4	Examples of vertical profiles of hydrometeor proportions for three different events. The thick lines show the average value and the shading represents the quartiles calculated over the entire spatial domain for a single 30 minute time step.	85
4.5	RMSE and Pearson correlation coefficient for dBZ only-models and HC + dBZ-models trained with data starting from increasing altitude levels. The thick lines indicate the average values and the shading the quartiles calculated over ten model runs using different combinations of events for the training, validation and testing datasets. . . . .	86

## List of Figures

---

4.6	2D histogram for observed (x-axes) and predicted (y-axes) GD for the HC + dBZ-models (top row) and dBZ-only models (bottom row) trained with data starting from higher altitude levels and aloft (columns). The number of points in each bin is indicated in colour. . . . .	87
4.7	2D histogram matrices for 1500 m a.s.l. (top row) and 2500 m a.s.l. (bottom row) for observed data (left), HC + dBZ-model (center) and dBZ-only model (right). The colour of each bin is based on the average GD value. . . . .	89
4.8	2D histogram error matrices from 1500 m a.s.l. for HC + dBZ-model (left) and dBZ-only model (right). The colour of each bin is based on the difference between the observed binned average and the binned average of the model output. . . . .	90
4.9	2D histogram error matrices from 2500 m a.s.l. for HC + dBZ-model (left) and dBZ-only model (right). The colour of each bin is based on the difference between the observed binned average and the binned average of the model output. . . . .	91
4.10	2D histogram matrices for observed (x-axes) and predicted (y-axes) GD for the HC + dBZ-model (left) and dBZ-only model (right) trained from 1500 m a.s.l. and data aloft. The number of points in each bin is indicated in colour. . . . .	92
4.11	2D histogram matrices for observed (x-axes) and predicted (y-axes) GD for the HC + dBZ-model (left) and dBZ-only model (right) trained from 2500 m a.s.l. and data aloft. The number of points in each bin is indicated in colour. . . . .	93



# List of Tables

1.1	Doppler and polarimetric variables obtained by weather radars . . . . .	12
2.1	Daily variances of $Z_{DR}$ , $Z_H$ and $Z_V$ as well as for CAL signal H, V and H-V. For all events, and ranking of event in <b>Poor</b> ( $>3.8$ ), <i>Intermediate</i> ( $>2.2$ ) or Good. . . . .	31
2.2	$dN/dh$ calculated between Cimetta and Matro, median, standard deviation and quartiles. . . . .	32
2.3	Correlation coefficients $Z_{DR}/Z_V$ , $Z_V/CAL_{dr}$ , $Z_V/temperatures$ and $Z_V/Z_H$ . . .	41
3.1	Characteristics of the MXPOL radar and scanning strategy during the Valais campaign. . . . .	58
3.2	Statistics of the polarimetric variables related to the melting layer for the DX50 and MXPOL in the Payerne and Valais campaigns. . . . .	66
4.1	Median number of pixels for 500 m height intervals (boundaries in first column) at increasing distances from the radar based on geometry for a single volume scan and a cone with 4 km radius at the base and a 10 km radius at the top. The altitudes given in the first two columns are in metres above sea level. . . . .	80
4.2	Statistics for the precipitation events used in this study. Daily precipitation sums and wind speeds are from the ground station Cham at approximately 15 km distance from the Albis radar. For the GWT weather type classification (Weusthoff, 2011), LP, HP and FP represent High Pressure, Low Pressure and Flat Pressure situations respectively, the other acronyms are abbreviations of GWTWS flow directions. The letters A and C indicate advective or convective types. . . . .	81
4.3	RMSE and <b>Pearson correlation coefficient</b> scores for various VPR correction techniques applied to an independent test dataset of 3884 cones. . . . .	95



# 1 Quantitative precipitation estimation in an Alpine context

Precipitation constitutes a key meteorological parameter for ecosystems and societies, both as a primary input for freshwater resources and (in deficit or excess) as a potential threat to human lives and infrastructure. Economic activities such as agriculture, hydropower and (mountain) tourism depend critically on precipitation patterns (Arent et al., 2014; Kohler et al., 2014). While water, precipitation and floods are embedded in many cultural and religious aspects of societies. Conflicts over water usage are therefore not uncommon from the local up to international scales (Gleick and Heberger, 2014).

Mountain regions such as the Alps, through their impact on atmospheric flow, influence the spatial distribution of precipitation (Frei and Schär, 1998; Roe, 2005; Houze, 2012; Colle et al., 2013) as well as precipitation growth processes and microphysics (Yuter and Houze, 2003; Colle et al., 2005b; Stoelinga et al., 2013). But mountain climates and vegetation also control runoff, water storage and glacier mass-balance (Beniston, 2005). Notably, the Swiss Alps have been referred to as the "water tower of Europe" as they are the source region for 50% of the water flowing through the Rhine, the Rhone and the Po rivers (Mountain Agenda, 1998; Beniston et al., 2011). Thus, Alpine precipitation amounts and intensity not only affect the Alpine area, but also the populated lowland regions that depend on mountain resources. Recent changes in temperature have had observable impacts on mountain cryosphere and ecosystems (Vaughan et al., 2013; Arent et al., 2014; NCCS, 2018). At the same time, it is considered increasingly likely that climate change will also affect the frequency, intensity and duration of precipitation events (Frei et al., 2006; IPCC, 2018). Accurate observations of precipitation quantities are therefore important at many scales: from short-term predictions to minimise disaster impact, to long term reliable estimations of fresh water resources.

Due to the socio-economic importance of precipitation, its measurement has a long history dating back to antiquity. However, notwithstanding many technological developments, the accurate measurement of precipitation still remains a challenge today, especially in mountainous areas. Rain gauge networks are typically affected by poor spatial representativity, wind-induced errors (especially in the case of solid precipitation (Nitu et al., 2018)) and practical difficulties related to access and maintenance. It was in the aftermath of World War II that

the potential of radars (radio detection and ranging) to observe precipitation was recognised and further developed (Marshall et al., 1947). Since then, radar technology has improved significantly and many weather radars today are equipped with dual-polarisation and Doppler capabilities thus providing additional information on the phase, homogeneity and shape of hydrometeors as well as the radial velocity of the precipitation field.

The high spatial and temporal resolution of radar products, their three dimensional nature as well as the possibility to distinguish precipitation types, gives radar networks significant advantages over rain gauge networks, especially for nowcasting and severe weather warnings (MeteoSwiss, 2016). However, quantitative precipitation estimation (QPE) by radar is still subject to many sources of error such as ground clutter, hardware calibration, visibility reduction due to beam shielding and attenuation in heavy rain to name a few (Germann and Joss, 2004). Some of these errors are even more pronounced in mountainous terrain, where beam shielding by relief allow weather echoes only to be detected at high altitudes. This, combined with the shallow depth of precipitation during cold seasons implies that the radar can only measure hydrometeors aloft, and not what is actually arriving at the ground level (Germann and Joss, 2004; Koistinen et al., 2004; Gabella et al., 2014).

For areas with reduced visibility it is common practice to use the radar measurements made higher up in the atmosphere to estimate precipitation quantities at the ground. The extrapolation of these high altitude measurements requires that these must first be corrected for the vertical profile of precipitation in order to account for changes in size, phase and fall speed of hydrometeors. Because these vertical profile corrections are typically based on and applied to a single radar variable called *reflectivity*, this technique is called vertical profile of reflectivity (VPR) correction. Moreover, the existing VPR correction schemes used in the operational radar chains of most National Meteorological and Hydrological Services (NMHS) assume spatio-temporal homogeneity of the vertical structure of precipitation. However, the VPR shape is dependent on microphysical processes such as riming and aggregation (Fabry and Zawadzki, 1995; Bell, 2000) as well as the vertical profiles of temperature and humidity (Matsuo and Sasyo, 1981; Roe, 2005; Stoelinga et al., 2013) which may vary considerably in both space and time. As such, the vertical structure of precipitation and thus the VPR profiles may be expected to vary as well, especially in mountainous areas (Boodoo et al., 2010; Campbell and Steenburgh, 2014).

In order to increase the availability of radar information, particularly in the inner Alpine regions, MeteoSwiss has recently extended its operational weather radar network with two polarimetric C-band radars at high-altitude locations in the Swiss Alps (MeteoSwiss, 2016). This poses a new challenge for the applicability of existing vertical profile correction techniques to these high-altitude measurements but at the same time it also provides new opportunities to use polarimetric radar variables for the improvement of QPE in these regions. This thesis seeks to contribute to the improvement of QPE by radar in the Alps through the analysis of the spatio-temporal variability of the polarimetric radar signals.

### 1.1 Measurement of precipitation by polarimetric weather radar

Because the analyses presented in this thesis are performed on polarimetric radar signals, this section will provide a brief introduction to radar hardware and measurements and how these are used for precipitation observations. This section will focus exclusively on pulsed radars, since the data presented in this work is collected by this type of radar. Furthermore, the term “polarimetric radar” is used in this study to refer to dual-polarisation (pulsed) Doppler radars operating in simultaneous transmission and reception mode. Radars cover a large interval of frequencies, but the work in this thesis is based on measurements by operational C-band radars ( $\sim 5.4$  GHz) and mobile X-band radars ( $\sim 9.41$  GHz).

#### 1.1.1 A short overview of radar hardware

Because of the importance of radar hardware stability for accurate precipitation measurement and because the monitoring of radar hardware is also addressed in this thesis, this section will briefly describe some of the main components the radar system. The main sources for the information presented in this section are the radar user manuals and the textbooks by [Rinehart \(2004\)](#) and [Fabry \(2015\)](#). For more details, the reader may refer to these works.

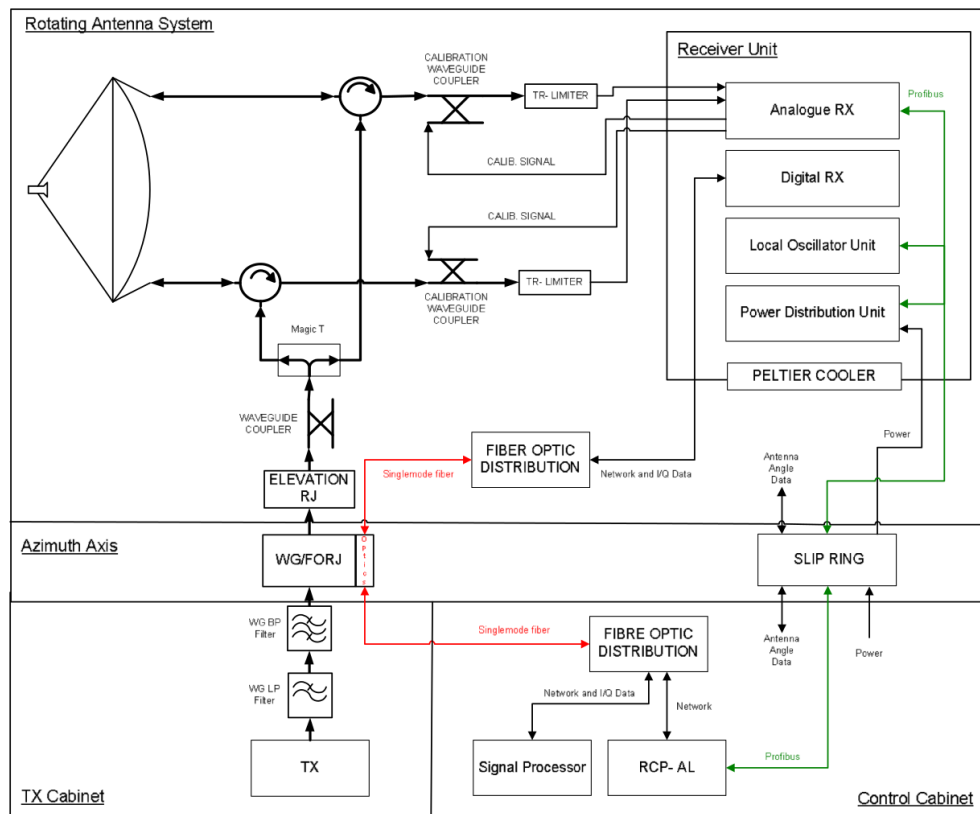


Figure 1.1 – AMR-radar system block diagram taken from [Vollbracht et al. \(2014\)](#).

## Chapter 1. Quantitative precipitation estimation in an Alpine context

---

Figure 1.1 illustrates the system architecture for the Antenna-mounted receiver (AMR) type radars used in the Swiss operational C-band network. The design of C-band radars differs from mobile X-band radars for example, which are much more compact. Unless mentioned otherwise, the components described in this section are common to all types of dual-polarisation (pulsed) Doppler radars.

The key components of the radar system interact in the following way:

1. the *modulator* switches the *transmitter* on and off
2. the *transmitter* generates a microwave signal of short duration and large amplitude
3. this signal is transported through the *waveguide* to the *duplexer*
4. the *duplexer* acts as a switch between the *transmitter* and *receiver* in order to protect the *receiver* from the high power pulses generated by the *transmitter*
5. the signal then travels on through the *waveguide* towards the radar *antenna*
6. the *antenna* focuses the signal in one direction and into the atmosphere
7. the returned echoes from targets, the intensity of which is much smaller than that of the signal which was emitted, are focused back into the radar system by the *antenna*, past the *duplexer*, the *TR-Limiter* and into the radar *receiver*, where the RF signal at intermediate frequency (IF) is digitised for signal processing
8. the *signal processor* then extracts as much raw data as possible from the received signals, while the task of converting the raw data into radar products is usually performed by software on computers not necessarily based at the radar site.

Here follow a few short descriptions of the roles of some of these key components of the radar system:

**Transmitter (consisting of a modulator and a magnetron):** the purpose of the modulator is to switch the transmitter on and off and therefore determines the shape and duration of the transmitted pulse (i.e. the Dual Pulse Pair (DPP) or Fast Fourier Transform (FFT) modes). This controls some important variables which will also be mentioned in the following sections such as the Pulse Repetition Frequency (PRF) and the duration of the transmitted signal in time ( $\tau$ ) or the pulse length in distance ( $h_p$ ).

**Duplexer, TR-Limiter** or transmit / receive (TR) switch: radars can transmit between 1 kW and 1 MW of power. The received power, however, is between  $10^{-4}$  W down to  $10^{-14}$  W. The receiver therefore has to be sensitive to these very weak signals but would be destroyed by the high power of the transmitted signal (a receiver is likely to be close to saturation at power levels

## 1.1. Measurement of precipitation by polarimetric weather radar

---

around  $10^{-4}$  W). The circulator directs the signal to the antenna when the transmitter is on. In order to further protect the receiver during transmission, a TR-tube is placed between the duplexer (circulator) and the receiver. The TR-Limiter acts as a switch, effectively blocking the receiving path during pulse transmission. It is important to note that after pulse transmission, the TR-Limiter needs a certain amount of time to fully reopen the receiver path. This time is called recovery time and may vary between 1 and 10  $\mu$ s which equals the first 150 to 1500 m from the radar.

**(Digital) Receiver:** detects the echo signals in the presence of noise, interference or clutter. Amongst other functions, it amplifies the incoming signal to usable levels, rejects out-of-band interference through the band-select filter and shapes the signals and the noise to gain the maximum signal-to-noise ratio (SNR) (Chen, 2013).

**Analogue receiver and calibration unit:** consists of four low noise amplifiers (LNAs) for the high gain (HI) and low gain (LOW) paths for both polarisations, one or two down converter channels for horizontal and vertical polarisation and two reference sources for calibration: the first is an Internal CW Test Signal Generator (ITSG), used to guarantee receiver linearity between the HI and LOW channels, thus over the entire dynamic range. The second, which is specific to the MeteoSwiss operational C-band radars, is a reference noise source, used for absolute calibration and monitoring.

The reference noise source signal (a stable, white noise reference signal) is injected every 5 minutes into the receiver path and used to correct for temperature dependent variations affecting the analogue receiver components' performance. This is possible due to the higher temperature stability of the noise source used, with respect to the other components of the analogue receiver, including the LNAs. In the MeteoSwiss operational network calibration signals are injected every 5 minutes during higher elevation scans at ranges where no weather echo is expected. More details on the use of noise source reference signals for radar calibration can be found in Vollbracht et al. (2014).

### 1.1.2 Basic radar measurements and the radar equation

Weather radars transmit into the atmosphere electromagnetic (EM) waves at wavelengths which vary from 1 cm to tens of centimetres. When travelling through a precipitation filled medium, this signal is partly backscattered to the radar with an intensity and phase which depends largely on the characteristics of the target (i.e. hydrometeor shape, size and phase) but also on the environmental conditions of the medium through which the EM waves travel (the atmosphere). This section describes how the range and radial velocity of the echoes received by the radar can be obtained and how the *reflectivity factor* can be derived from the received power. More detailed overviews of the principles presented here can be found in the works by Rinehart (2004), Doviak and Zrnić (2006) and Fabry (2015).

## Chapter 1. Quantitative precipitation estimation in an Alpine context

---

For a radar which transmits a pulse at time  $t_0$  which propagates through the atmosphere at the speed of light in air  $c/n$  and arrives back at the radar at time  $t_1$  the **range of the target** corresponding to the returned echo  $i$  can be determined using:

$$r_i = \frac{c(t_1 - t_0)}{2n} \quad (1.1)$$

where  $n$  is the refractive index of the atmosphere (see also appendix A) and  $c/n$  accounts for the speed of light in air. However, since  $n$  is very close to 1 (1.0003) near sea level, it will be omitted in the remainder of this section. After some time ( $f_r^{-1}$ ) the radar transmits a new pulse: the Pulse Repetition Frequency (PRF or  $f_r$ ) determines the maximum unambiguous range ( $r_{\max}$ ) up to which the radar can observe targets since echoes which arrive from further ranges than the  $r_{\max}$  can not be distinguished from echoes which were returned by targets at closer ranges by a subsequent pulse:

$$r_{\max} = \frac{c}{2f_r} \quad (1.2)$$

The phase of the returned signal  $\phi_i$  can be obtained by adding the fraction of wavelength  $((2r/\lambda)2\pi)$  to the initial phase of the transmitted signal  $\phi_0$ :

$$\phi_i = \phi_0 + \frac{4\pi r_i}{\lambda} \quad (1.3)$$

Where  $\lambda$  is the wavelength of the radar pulse which also depends on the transmit frequency ( $\lambda = c/nf_r$ ). Provided the transmit frequency  $f_r$  and the refractive index  $n$  are constant, the phase difference between the transmitted and received pulse can be related to the **radial velocity of the targets**:

$$\frac{\delta\phi}{\delta t} = \frac{4\pi}{\lambda} \frac{\delta r}{\delta t} \quad (1.4)$$

Where  $\delta r/\delta t$  gives the radial velocity  $V_{\text{rad}}$  of the target. The frequency shift  $f_t$  caused by a moving target can then be obtained by expressing the angular frequency as  $\Omega = \frac{\delta\phi}{\delta t} = 2\pi f_t$ :

$$f_t = \frac{2V_{\text{rad}}}{\lambda} \quad (1.5)$$



### 1.1. Measurement of precipitation by polarimetric weather radar

The following equations demonstrate how the reflectivity factor is derived from the power measured by the radar. The measured power in the standard form of the radar range equation for a point target is given by:

$$P_r = \frac{P_t G^2 \lambda^2 \sigma^b}{(4\pi)^3 r^4} \quad (1.6)$$

Where  $P_r$  and  $P_t$  are the received and transmit power in W or mW,  $G$  is the gain of the radar system (mostly the antenna gain),  $\lambda$  is the wavelength of the transmitted pulse in m,  $r$  is the distance to the target in m and  $\sigma^b$  is the radar cross section (RCS) of the target in m<sup>2</sup>. The RCS depends on the size of the target as observed by the radar. For a sphere which is large compared to the wavelength of the radar for example, the RCS can be given by  $\sigma = \pi r_a^2$  where  $r_a$  is equal to the radius of the spherical target. When measuring precipitation however, the radar volume is not filled by a single target but by approximately  $10^9$  to  $10^{12}$  raindrops, and the signal returned is the sum of all backscattering cross-sectional areas within the radar volume:

$$\sigma^b = V \sum_{i=1}^k \sigma_i^b = V \int_{D_{\min}}^{D_{\max}} \sigma^b(D) N(D) d(D) = V\eta \quad (1.7)$$

Where  $N(D)d(D)$  is the expected number of hydrometeors with a diameter between  $D$  and  $D + dD$  per unit volume according to the particle size distribution  $\sigma^b(D)$ ,  $\eta$  is the reflectivity and  $V$  is the resolution volume:

$$V = \pi \frac{r^2 \theta_{3\text{dB}} \phi_{3\text{dB}} h_p}{16 \ln(2)} \quad (1.8)$$

Where  $\theta_{3\text{dB}}$  and  $\phi_{3\text{dB}}$  are the one-way half-power beam widths in elevation and azimuth,  $r$  is again the range distance between the sample volume and the radar and  $h_p$  is the pulse length in space corresponding to the duration  $\tau$  of the transmitted pulse:  $h_p = c\tau$ . The denominator in Eq. 1.8 accounts for the two-way path of the signal and the power distribution within the main lobe of the beam which is approximated to have a gaussian shape  $1/(2\ln(2))$ . It can also be observed from Eq. 1.8 that the resolution volume increases with the square of the range ( $r^2$ ).

Substituting  $\sigma^b$  in Eq. 1.6 with the RCS for distributed targets in a radar volume, the following

radar equation can be obtained:

$$P_r = \frac{P_t G^2 \lambda^2 \pi \theta_{3dB} \phi_{3dB} c \tau \sum \sigma_i^b}{(4\pi)^3 r^2 16 \ln(2)} = \frac{P_t G^2 \lambda^2 \pi \theta_{3dB} \phi_{3dB} c \tau \sum \sigma_i^b}{1024 \ln(2) \pi^3 r^2} \quad (1.9)$$

For most meteorological radars with wavelengths of 3 cm and larger, almost all hydrometeors can be considered small ( $D < \lambda/16$ ) so that scattering occurs in the Rayleigh regime. This means that the RCS of a single hydrometeor increases with the sixth power of its diameter:

$$\sigma_i^b = \frac{\pi^5 |K|^2 D_i^6}{\lambda^4} \quad (1.10)$$

Where  $|K|^2$  is the dielectric constant of scatterers (typically  $|K|^2 \approx 0.93$  in liquid water) and is related to the complex index of refraction of the hydrometeor  $n(\lambda)$  via:  $|K|^2 = |(n(\lambda)^2 - 1)/(n(\lambda)^2 + 2)|^2$ .

Combining Eq. 1.10 with the definition of reflectivity  $\eta$  in Eq.1.7 gives:

$$\eta = \frac{\pi^5 |K|^2}{\lambda^4} \int_{D_{\min}}^{D_{\max}} D^6 N(D) d(D) = \frac{\pi^5 |K|^2}{\lambda^4} Z_e \quad (1.11)$$

Here,  $Z_e$  is defined because of the uncertainty about whether a target is a Rayleigh scatter or not. It is called the *equivalent reflectivity factor* and is expressed in units of  $\text{mm}^6 \text{m}^{-3}$ . Because the equivalent reflectivity factor can span many orders of magnitude, it is more convenient to express it in units of decibels (dB) of  $\text{mm}^6 \text{m}^{-3}$  such that:  $\text{dBZ} = 10 \log_{10}(Z_e)$ .

Again, substituting the Rayleigh equivalent reflectivity factor into the radar equation Eq. 1.9 gives:

$$P_r = \frac{\pi^3 P_t G^2 \theta_{3dB} \phi_{3dB} c \tau |k|^2 Z_e}{1024 \ln(2) r^2 \lambda^2} \quad (1.12)$$

Finally, all parameters associated with a specific radar ( $P_t$ ,  $G$ ,  $\theta_{3dB}$ ,  $\phi_{3dB}$ ,  $\tau$ ,  $\lambda$ ) and all the constants ( $\pi$ ,  $c$ ,  $1024$ ,  $\ln(2)$ ,  $|K|^2$ ) in Eq. 1.12 can be combined into a single constant  $C_r$ , so that

the radar equation can be greatly simplified into:

$$P_r = \frac{C_r Z_e}{r^2} \quad (1.13)$$

The above equations describe the relationship between the power received by the radar ( $P_r$ ), the characteristics of the radar (and constants) ( $C_r$ ) and the characteristics of the target ( $Z_e$  and  $\eta$ ) as a function of the range between the radar and the targets ( $r$ ). However, as the EM waves propagate through the atmosphere, they are both refracted and attenuated. Attenuation of EM waves by liquid clouds and precipitation increases with the frequency of the radar signal, the distance the EM wave travels through the atmosphere and the number of hydrometeors it encounters over that distance. While attenuation may also affect radar QPE it is outside the scope of this study and will not be addressed further. Atmospheric refraction influences the direction of the EM waves as they travel through the atmosphere. The influences of atmospheric refraction on the radar measurements is addressed in more detail in chapter 2 and appendix A.

### 1.1.3 Polarimetric radar observables

An important technological development in weather radar technology has been the addition of dual-polarisation capabilities. Single-polarisation weather radars typically transmit linearly and horizontally polarised EM waves. For such a horizontally polarised wave travelling in the  $x$  direction in a  $(x, y, z)$  space, the electric field oscillates in the horizontal ( $y$ ) direction, while the magnetic field oscillates in the vertical ( $z$ ) direction (Fabry, 2015). Polarimetric weather radars, on the other hand, can (simultaneously) transmit and receive waves at different polarisations. Typically this is an orthogonal couple of horizontal (H) and vertical (V) linearly polarised signals. This dual-polarisation technology is valuable firstly because the interaction of the EM wave with targets occurs via the electric field of the wave, and secondly because hydrometeors are not spherical targets: even raindrops for example, become more oblate with increasing drop sizes (Beard and Chuang, 1987; Beard et al., 2010) and snowflakes have many complex shapes and orientations (e.g. Schneebeli et al., 2013; Praz et al., 2017). Put simply, horizontally polarised echoes are more related to the horizontal dimension of the targets and vertically polarised echoes to their vertical dimension (Fig. 1.2). Many targets have different signatures in the H and V polarised measurements and dual-polarisation can therefore provide additional information on the nature of targets. A more detailed description of the physics and usage of dual-polarisation can be found in for example Bringi and Chandrasekar (2001).

#### Horizontal (Vertical) reflectivity factor

The reflectivity factor  $Z_e$  is related to the received power as expressed in Eq. 1.12, and the horizontal (vertical) reflectivity factors  $Z_H$  ( $Z_V$ ) are the dual-polarisation equivalents of  $Z_e$ .

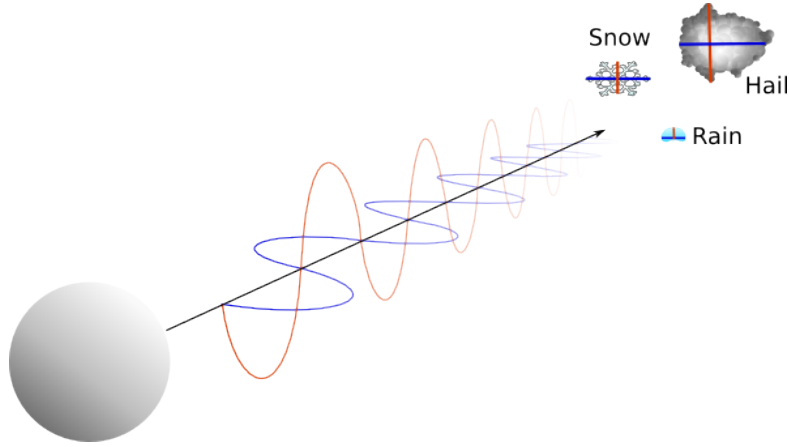


Figure 1.2 – Illustration of the electric field of oscillation at horizontal (blue) and vertical (red) polarisation.

As has been described in the previous section, the reflectivity factor is commonly expressed in dB units or dBZ. Like  $Z_e$ , the values of  $Z_H$  and  $Z_V$  depend on the particle size distribution (proportional to  $D^6$  (Eq. 1.11)), the incident wavelength and the dielectric properties of the hydrometeors (i.e. between liquid water and solid ice,  $|K|^2$  varies by a factor of 5).  $Z_H$  is therefore related to the diameter and concentration of hydrometeors.

### Differential reflectivity

Since the horizontal and vertical reflectivity measurements can give information on the horizontal and vertical dimensions of the targets and many hydrometeors are non-spherical, the most straightforward dual-polarisation variable is the difference between the H and V reflectivity measurements (Seliga and Bringi, 1976). The differential reflectivity ( $Z_{DR}$ ) is the Log-transformed ratio between the copolar reflectivity measured at H and V polarisations in dB:

$$Z_{DR} = 10 \log \left( \frac{Z_h}{Z_v} \right) \quad (1.14)$$

Where  $Z_h$  and  $Z_v$  are the horizontal and vertical reflectivity in linear units. The differential reflectivity is independent of hydrometeor concentrations and can provide information on the shape and orientation of hydrometeors. Typical values in rain are slightly positive and increase with increasing drop size. Values for  $Z_{DR}$  become close to zero when the radar is pointing vertically because falling hydrometeors appear symmetrical to the radar when measured from below.

### Copolar correlation coefficient

The  $Z_H$  and  $Z_V$  values are typically obtained through the averaging of the values of several pulses (how many pulses depends on the PRF and the amount of time the radar points in a single direction). As such, the correlation coefficient between  $Z_H$  and  $Z_V$  calculated over all these individual pulses can provide information on the heterogeneity of the hydrometeors in the measured volume:

$$\rho_{HV} = \frac{\left| \int_{D_{\min}}^{D_{\max}} s_{hh}^*(D) s_{vv}^*(D) N(D) dD \right|}{\sqrt{Z_h * Z_v}} \quad (1.15)$$

Where  $s_{hh}$  and  $s_{vv}$  are the complex backscattering amplitudes of individual hydrometeors at both polarisations in cm.

Thus, if targets in the radar volume have identical shapes, high  $\rho_{HV}$  values may be observed, while if targets in the radar volume have varied shapes the fluctuations in the H and V channels will become dissimilar and result in lower values for  $\rho_{HV}$ . Theoretically  $\rho_{HV}$  may range between 1 (perfect correlation) and 0 (no correlation), though in practice values below 0.75 are rare. The observed  $\rho_{HV}$  values also depend on the signal-to-noise ratio (SNR) of the radar measurements; since a high proportion of noise in the horizontal and vertical channels would also influence the correlation between these. Therefore, before using the  $\rho_{HV}$  measurements, measurements with low SNR values are typically filtered out.

### Specific differential phase shift upon propagation

As opposed to the previous variables, the differential phase shift  $\psi_{dp}$  is not based on the returned power of the targets but on the difference in the phase shift between the two orthogonal polarisation phases. This phase shift occurs because hydrometeors slow down the transmitted EM waves and non-spherical hydrometeors will cause a different phase shift in the two polarisations. The phase shift at a given range is given by:

$$\psi_{dp} = \varphi_{HH} - \varphi_{VV} = \delta_{co} + \Phi_{dp} + \psi_o \quad (1.16)$$

Where  $\delta_{co}$  (the backscattering phase delay) is the difference in delay introduced by the backscattering of the transmitted wave,  $\Phi_{dp}$  is the two-way differential propagation phase and  $\psi_o$  is an offset value equal to the phase difference between the transmitted and received H and V waves at zero range and which depends on the design of each radar.

The specific differential phase shift on propagation ( $K_{dp}$ ) is the one-way rate of increase

of  $\Phi_{dp}$  with range (in  $^{\circ} \text{ km}^{-1}$ ). If  $\delta_{co}$  is constant, derivatives of the smoothed  $\psi_{dp}$  can give accurate  $K_{dp}$  estimates. However, the contribution of  $\delta_{co}$  to the total differential phase shift depends on the incident wavelength and the size of the targets. While this may be negligible at C-band and for rain, at X-band  $\delta_{co}$  may vary considerably in space. For the estimation of  $K_{dp}$  at X-band, the effects of  $\delta_{co}$  and  $\Phi_{dp}$  can therefore be separated through Kalman filtering (e.g. Schneebeli et al., 2014). Given that  $K_{dp}$  is a derivative in range of a difference in polarisation, it is often very small and so difficult to measure accurately. However, since  $K_{dp}$  increases are related to large amounts of liquid water (and the hydrometeor shapes and orientations) it can be related to specific attenuation and rain rate (Zrnica and Ryzhkov, 1999).

Table 1.1 gives a short overview of the polarimetric variables here discussed.

Name	Symbol	Units	Hydrometeor information
reflectivity factor H,V	$Z_{H(V)}$	$\text{mm}^6 \text{m}^{-3}$ or dBZ	diameter, concentration
differential reflectivity	$Z_{DR}$	dB	shape, orientation,
copolar correlation coefficient	$\rho_{hv}$	-	heterogeneity
total differential phase shift	$\Psi_{dp}$	deg	concentration, shape
specific differential phase shift	$K_{dp}$	$\text{deg km}^{-1}$	concentration, shape

Table 1.1 – Doppler and polarimetric variables obtained by weather radars

### 1.1.4 Relating reflectivity to rain rate

Although different radar variables ( $Z_H$ ,  $Z_{DR}$  and  $K_{DP}$ ) can be related to rain intensity, most often and in operational contexts so-called Z-R relationships are used. These are power laws relating the rain intensity  $R$  in  $\text{mm h}^{-1}$  to linear horizontal reflectivity:

$$R = aZ_h^b \quad (1.17)$$

where the parameters  $a$  and  $b$  are obtained by fitting the power law with observational data from rain gauges or disdrometers. Because it was long believed that most of the errors in radar QPE were due to improper Z-R relationships, much research has focused on finding the most suitable Z-R relationship for each precipitation type (solid/liquid or stratiform/convective) (Šálek et al., 2004). The number of existing Z-R relationships is therefore abundant, however the most commonly used relationship is probably  $a = 200$ ,  $b = 5/8$  by Marshall and Palmer (1948) which is valid for mid-latitude stratiform rain.

Since the last two decades of the 20<sup>th</sup> century it has become increasingly clear that the Z-R related error is relatively minor especially compared to errors related to the vertical profile of reflectivity (Joss and Waldvogel, 1990). Indeed, Joss and Lee (1995) noted that a 500 m shift in the vertical profile may result in a larger error than the entire variability in the Z-R relationship. The next section will explain the principles of vertical profile correction in more detail and briefly discuss existing vertical profile correction techniques.

### 1.1.5 Relating polarimetric variables to hydrometeor classes

The information that can be obtained from the polarimetric radar variables can further be used for Radar-based hydrometeor classification. Existing methods can be broadly categorised into supervised, unsupervised and semi-supervised classification. Within the context of this work, the hydrometeor classes are obtained using a semi-supervised classification method from Besic et al. (2016). This approach combines the more classical supervised hydrometeor classification approach based on both fuzzy logic and the presumed electromagnetic behaviour of different hydrometeor types (e.g. Vivekanandan et al., 1999), and a new unsupervised clustering approach (Grazioli et al., 2015). The drawback of the supervised method is its dependency on uncertain scattering simulations, while the unsupervised method lacks the constraints related to hydrometeor microphysics. By combining the two approaches in a way that microphysical hypotheses can, to a degree, adjust the content of the classes obtained statistically from the observations, the semi-supervised method can overcome these disadvantages. The semi-supervised method can be separated into an offline and an online phase: first, the method iteratively compares statistically obtained clusters with presumed polarimetric properties and, where necessary, reiterates the statistical clustering in case of non-identification. The thus obtained centroids of the multi-dimensional polarimetric signatures of each hydrometeor class can then be applied online for the operational labelling of different hydrometeors. For more details on the semi-supervised hydrometeor classification approach, the reader is referred to Besic et al. (2016, 2018).

### 1.1.6 Polarimetric variables and the Melting Layer (ML)

The vertical structure of stratiform precipitation is typically marked by a significant increase in  $Z_H$  also called the bright band which highlights the presence of the melting layer; a transition region from solid to liquid precipitation. This increase in  $Z_H$  is due to the increase in effective dielectric constant as relatively large solid hydrometeors are coated by a thin layer of water. The increased heterogeneity of the hydrometeor types within the melting layer further causes for a drop in  $\rho_{HV}$ . Because the melting layer is characterised by such a pronounced and well-known signature in the polarimetric radar variables, it can be identified by automatic detection algorithms. Most existing algorithms are applicable to Plan Position Indicator (PPI) scans which are 360° azimuth, single elevation scans. The method proposed by Wolfensberger et al. (2016), on the other hand, is specifically designed for application to Range Height Indicator (RHI) scans (constant azimuth, varying elevation angle). The method is based on strong

vertical gradients in  $Z_H$  and  $\rho_{HV}$  and is divided into two parts. Taking the RHI scans projected into Cartesian coordinates as an input, the method first identifies the top and the bottom of the ML by finding the minimum and maximum vertical gradients of the combined, normalised  $Z_H$  and  $\rho_{HV}$  variables:  $IM_{comb} = Z_H \cdot (1 - \rho_{HV})$ . Then, the estimation of the ML top is refined using only the vertical gradient of  $Z_H$ . Small gaps in the detected ML are interpolated using shape-preserving piecewise Hermite interpolation polynomials. More details on the melting layer detection algorithm used for this study can be found in [Wolfensberger et al. \(2016\)](#).

### 1.2 Vertical profile correction

Ground clutter, earth curvature, beam shielding by relief or the height of the radar itself may prevent the radar from directly measuring precipitation close to the ground, thus causing holes in the radar image ([Germann and Joss, 2004](#)). At further ranges from the radar and for areas with reduced visibility it is common practice to use the radar measurements made higher up in the atmosphere to estimate precipitation quantities at the ground. However, changes in the size, phase and fallspeed of hydrometeors cause the radar echo to also change with height. Therefore, the extrapolation of these high altitude measurements to the ground requires that these must first be corrected for the vertical changes in the radar echo. This is called vertical profile correction, and because it often concerns exclusively the horizontal reflectivity measurements of the radar, it is also called vertical profile of reflectivity (VPR) correction.

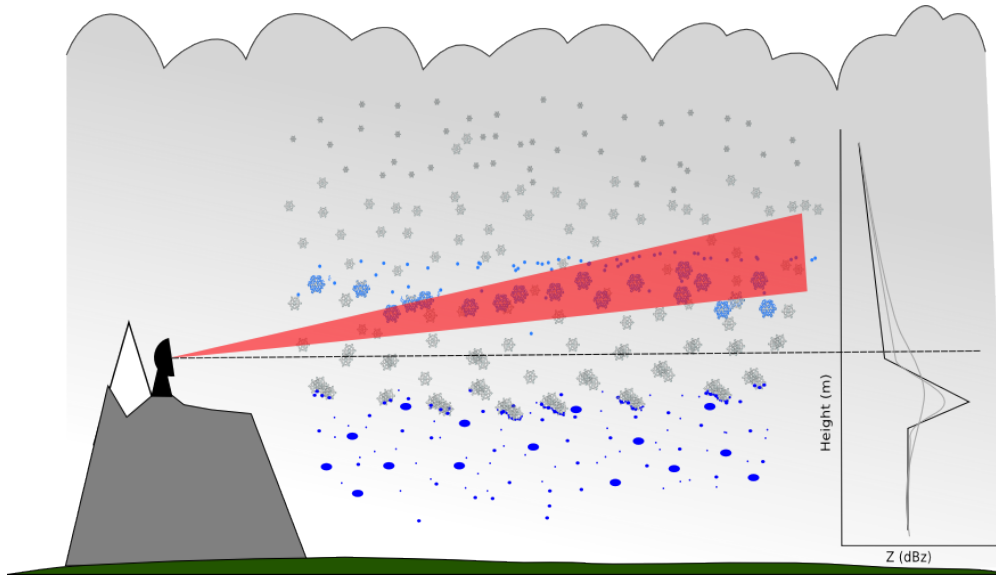


Figure 1.3 – Schematic illustration of a radar measuring above the melting layer (left) and an idealised vertical profile of reflectivity in stratiform precipitation (right) at close (black curve) and further ranges (grey curves) from the radar.

Factors influencing the shape of the VPR include microphysical processes such as riming



and aggregation (Fabry and Zawadzki, 1995; Bell, 2000) as well as the vertical profiles of temperature and humidity (Matsuo and Sasyo, 1981; Roe, 2005; Stoelinga et al., 2013). Most studies distinguish VPRs for stratiform (widespread, lower rainfall intensities) and convective (more localised and with higher rainfall intensities) precipitation types. The typical profile for stratiform precipitation is marked by a significant increase in  $Z_H$  due to the presence of the melting layer (Fig. 1.3). The VPR for convective precipitation on the other hand, typically shows little variability of  $Z_H$  with height: due to the vertical air motions more mixing of the hydrometeors occurs leading to a less stratified vertical structure. This means that in general, little profile correction is needed in convective precipitation and sometimes it is neglected altogether (Zhang and Qi, 2010).

Orography influences the vertical structure and the spatial distribution of precipitation through its various influences on precipitation mechanisms. At the large scale, it may force air masses upwards leading to orographic enhancement of precipitation while at the smaller scales the change in flow influences precipitation growth processes and microphysics (Yuter and Houze, 2003; Colle et al., 2005b; Stoelinga et al., 2013). This is further complicated by the wide range of spatial and temporal scales on which these effects take place. Because VPR corrections are typically based on well-visible regions close to the radar, the effects of orography are often neglected, with the notable exception of the UK Met. Office's Nimrod system which uses a VPR correction scheme which takes into account the anticipated orographic enhancement based on the enhancement fields found by Hill (1983).

Existing VPR correction methods can be subdivided into four broad types (Germann, 2000; Zhang and Qi, 2010) which are based on climatology, spatio-temporal averages, modelled and local VPRs. Climatological VPRs are based on radar data averaged over long time periods (days, years, seasons) and over a certain spatial area (radar volume or well-visible regions) (Joss and Pittini, 1991; Joss and Lee, 1995). Advantages of these type of VPRs are that, once calculated, they are computationally inexpensive, based on actual radar data and always available. However, the climatological VPR assumes both spatial and temporal homogeneity, while in reality important variations may occur. Operationally, the climatological VPR is often used as a default VPR in case the real-time VPR is unavailable.

Compared to the climatological VPRs, spatio-temporally averaged VPRs can better capture the temporal variations in reflectivity since these are based on a few volume scans only and regularly updated. They remain computationally inexpensive and are therefore widely used for operational VPR correction (Koistinen, 1991; Joss and Lee, 1995; Germann and Joss, 2002). In the MeteoSwiss operational network profiles are calculated in well-visible (clutter free) regions around the radar at the meso-beta scale (integrated over a few hours and within a range of 70 km). For the aggregation in space, the polar pixels are weighted by the area of the corresponding pulse volume. For the aggregation in time, a precipitation- and volume weighted exponentially decaying function is applied, with the profile of the most recent precipitation event as a first guess. The aggregation time is variable, such that it is more regularly updated for widespread rainfall while longer time aggregation is performed for intermittent rainfall in order to smooth the profile (Germann and Joss, 2002). This technique has the advantage of

always providing a vertical profile, with smooth transitions between subsequent radar scans and within reasonable processing times.

An alternative method to better account for the spatial variability of profiles is to use a VPR model to obtain a profile at each location (e.g. [Kitchen et al., 1994](#); [Kirstetter et al., 2013](#)). These can be determined using a set of physically based parameters in order to remain computationally inexpensive. The UK Met office for example, uses parameterisations for the melting layer (NWP model freezing level height), orographic growth ([Hill, 1983](#)) and the cloud top height (satellite infrared imagery) ([Harrison et al., 2000](#)). The parameterised vertical profile is then weighed by the reflectivity factor measured just beneath the bright band ([Harrison et al., 2000](#)). Though the VPR model has the advantage of providing a profile at each radar pixel, some disadvantages include its dependency on the availability and quality of information from external sources as well as on a priori assumptions on the shape of the VPR (i.e. the slope of the VPR in the solid layer).

Another more localised VPR correction technique has been proposed by [Vignal et al. \(1999\)](#), which uses the inverse method from [Andrieu and Creutin \(1995\)](#) to retrieve profiles in spatial domains of 20x20 km. This local VPR has been evaluated to be slightly more successful in improving radar-derived QPE than the mean VPRs, but it was also considered computationally expensive and thus difficult to implement operationally ([Vignal et al., 2000](#); [Vignal and Krajewski, 2001](#)). Furthermore, the advantage of this inverse technique is still limited to well-visible regions, while the dominant error in regions with complex terrain rather comes from applying profiles which were identified in a well-visible region to a shielded region ([Germann, 2000](#)). Though the profiles identified with the inverse technique better represent the narrow shape of the bright band, such a profile can cause more error than profiles with smooth bright bands if the height of the melting layer is incorrect. Given the spatial and temporal variability in the melting layer height in the Alps, it would be necessary to apply the inverse technique at a spatio-temporal scale of less than 30 minutes and 10 km ([Germann, 2000](#)).

Existing operational VPR correction schemes therefore often assume spatio-temporal homogeneity of the vertical structure of precipitation. Climatological VPR correction techniques assume that for the same precipitation type (stratiform or convective) the shape of the VPR is always more or less the same. Spatio-temporally averaged VPRs are slightly more elaborate than climatological VPRs, but make the assumption that the VPR observed at a close range to the radar, is also applicable to other (less visible) regions further away from the radar. Finally, VPR models allow for much more localised corrections but either rely on some basic assumptions on the shape of the VPR or on information from external sources. All of these approaches also rely heavily on the horizontal reflectivity measurements, while most operational radar networks, including the Swiss network, now dispose of dual-polarisation capability.

## 1.3 Building tools for the analysis of the spatio-temporal variability of radar data

In this section, some methods which were developed or elaborated within the context of this thesis will be briefly described and discussed. Firstly, the set-up of a spatial data base for the exploitation and combination of data from different instruments, stored in different data formats and measured at different frequencies, time intervals and scales will be described. Although this tool will not be mentioned specifically in the remainder of this work, it constituted a useful inventory for existing relevant data sets, permitted the initial exploration of these data sets and was the basis for many of the subsequently developed tools including (small) contributions to and integration with the Pyrad/Py-ART framework (Helmus and Collis, 2016; Figueras i Ventura et al., 2017). The second part of this section will describe how, in the context of this study, the so-called fraction of variance explained by component is derived from the well-know Fourier method to analyse the spatio-temporal variability of the (polarimetric) radar signals. The framework for the inclusion of information on hydrometeor classes and the application of machine learning algorithms to the study of the vertical structure of precipitation referred to in this thesis is the subject of chapter 4.

### 1.3.1 Development of a spatial data base and tools

An important technical challenge for the realisation of the work presented in this thesis was the combination of data from different sources. These included the five operational MeteoSwiss C-band radars, two mobile X-band (research) radars with changing scan strategies, several disdrometers used during measurement campaigns as well as temperature, humidity and wind speed data from the meteorological stations of the Swiss national ground network (SwissMetNet). In order to facilitate the analysis of data from various instruments, stored in different data formats with different metadata, measured at different frequencies, time intervals and scales, a spatial data base and accompanying toolkit was set up. An important requirement for this framework was that it would easily allow the addition of new instruments, data and functions. The reusability of the program, the modularity of its components as well as the possibility to use the components independently from each other were also important requirements, which is why the choice was made to work with an object oriented, open source programming language (Python).

The implementation consisted roughly of two parts: the creation of a PostgreSQL data base (extended with Geographic Information System (GIS) capabilities) to store (a) information on the instrument locations, spatial extent, timing and types of measurements and (b) the calculated vertical profiles and associated meteorological data, as well as the construction of a Python toolbox to work with the data base and automatise the processes. As part of this Python toolbox for example, a *DataBase* class was created regrouping all of the functions which handle the interactions between the Python toolbox and the PostgreSQL data base (Fig. 1.4). This set up resulted in three important advantages, which also comply with the above mentioned

## Chapter 1. Quantitative precipitation estimation in an Alpine context

requirements. Firstly, the data base can store the instrument metadata in a “standardised” way, thus allowing to perform the same queries for data from different instruments. Secondly, the addition of new instruments is facilitated because it merely requires extending the functions in the *DataBase* class rather than rewriting whole parts of the program. And finally, the functions designed to set up the data base, specifically search for instrument files within the given file paths on the computer or server. This means that the data base can be set up on any computer or server, that data can be easily and automatically added and that only data which is available on the computer or server ends up in the data base, avoiding problems later on in the program.

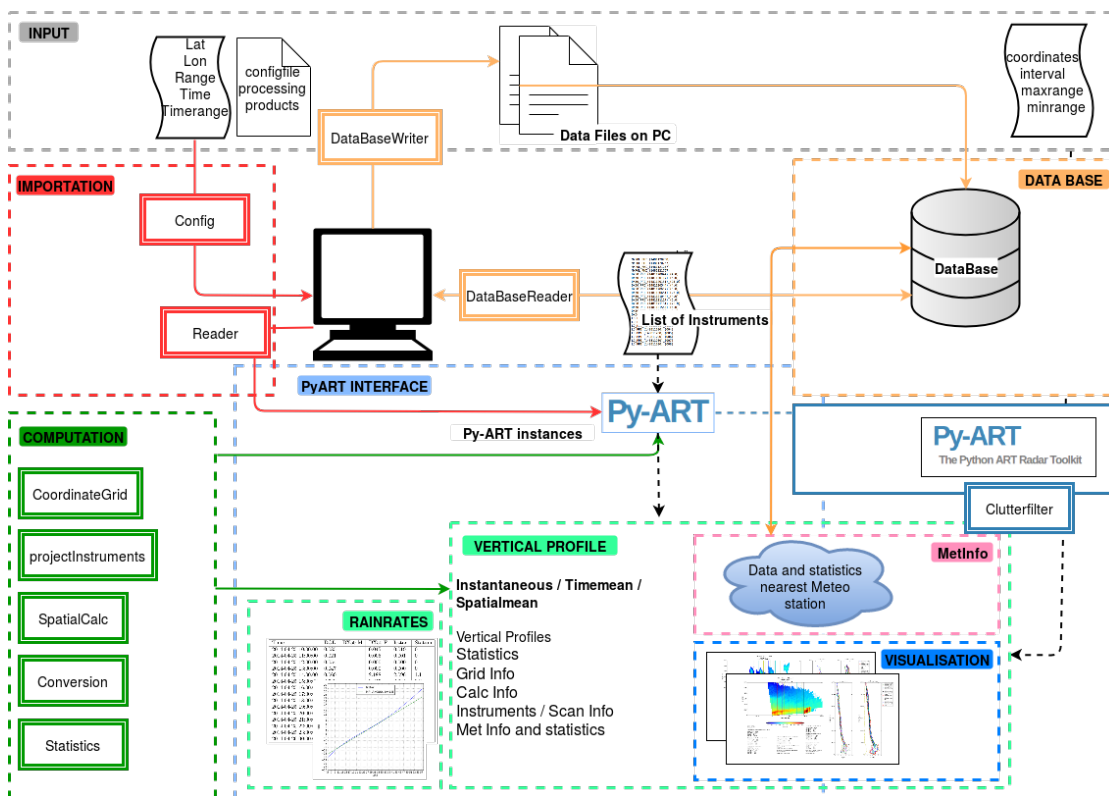


Figure 1.4 – A schematic overview of the interactions between the spatial data base and the toolboxes.

The GIS extension to the data base allows to perform spatial queries. That is, for a given spatial coordinate point, a spatial range or shape around the coordinate point, and for a given time (range), the program will give a list of available instruments and radar scans in the data base. From this list, specific instruments and scans can be selected for further analysis. As Fig. 1.4 further illustrates, using information from the data base, py-ART Radar instances containing data and metadata are created for each of the selected instruments via the *pyARTInterface* class which handles the interaction between the toolbox developed for this study and the py-ART toolbox<sup>1</sup>

<sup>1</sup>The *py-ART ARM Radar Toolkit (py-ART)* is a freely available Python toolbox containing a collection of algorithms and utilities created by the Atmospheric Radiation Measurement (ARM) Climate Research Facility for

---

### 1.3. Building tools for the analysis of the spatio-temporal variability of radar data

---

Finally, the toolbox can extract vertical profiles from the py-ART Radar instances, and based on the initial spatial coordinates and time inputs of the spatial query (Fig. 1.4) average vertical profiles are extracted for specific points, spatial ranges and time intervals.

#### 1.3.2 Spectral analysis and the fraction of variance explained by component

Spectral analysis, similarly to variograms, is a frequently used tool to study the second-order properties of a process. In meteorology, it has been used in fields ranging from boundary layer meteorology (Van der Hoven, 1957; Stull, 1988), radar observations of turbulence (Crane, 1980), the analysis of the spatial representativeness of precipitation forecasts (Harris et al., 2001) to probabilistic nowcasting (Bowler et al., 2006; Nerini et al., 2017). Spectral analysis has also been applied to reveal the scaling behaviour of precipitation over both temporal (Fraedrich and Larnder, 1993) and spatial (Mandapaka et al., 2009) scales as well as the correlation of these (Rysman et al., 2013). And the spectral slope (or  $\beta$  slope) values have been found to be dependent on the underlying meteorological processes; convective rain processes for example, having steeper spectral slopes than stratiform ones (Purdy et al., 2001; Nykanen and Harris, 2003; Nykanen, 2008). In this thesis, spectral analysis, or more specifically, the fraction of variance explained by component obtained from the Fast Fourier Transform (FFT), is used to study the the variability of polarimetric weather radar signals. This section will briefly describe how the fraction of variance explained by component is obtained from the Fourier Transform and how these relate to spectral slopes.

First, the spatial or temporal series of a measured variable are subjected to the one dimensional Fast Fourier transform, such that for each variable  $A$  of length  $N$  the Fourier transform returns  $N$  coefficients of  $F_A(n_c)$  for every frequency  $n_c$ . Any discontinuities in the series have to be padded (filling of data gaps with artificial data points) before applying the transform. The fraction of variance explained by each component  $n_c$  can then be obtained by dividing the square of the norm of the complex Fourier transform by the total variance:

$$\frac{|F_A(n_c)|^2}{\sigma_A^2} \quad (1.18)$$

Where the square of the norm of the complex Fourier transform for any frequency  $n_c$  is obtained by combining the real and imaginary parts:

$$|F_A(n_c)|^2 = F_{\text{Re}}^2(n_c) + F_{\text{Im}}^2(n_c) \quad (1.19)$$

And the total variance of the original series is derived by summing the square of the norm  

---

working with weather radar data.

( $|F_A(n_c)|^2$ ) over  $n_c = 1$  to  $N - 1$  ( $n_c = 0$  is excluded because  $|F_A(0)|$  is the mean value):

$$\sigma_A^2 = \frac{1}{N} \sum_{k=0}^{N-1} (A_k - \bar{A})^2 = \sum_{n_c=1}^{N-1} |F_A(n_c)|^2 \quad (1.20)$$

It should be noted that this is different from the discrete spectral density, which is calculated as:

$$\begin{aligned} E_A(n_c) &= 2 \times |F_A(n_c)|^2, \text{ for } n_c = 1 \text{ to } n_f \text{ with } N = \text{odd} \\ E_A(n_c) &= 2 \times |F_A(n_c)|^2, \text{ for } n_c = 1 \text{ to } (n_f - 1) \text{ with } N = \text{even} \\ E_A(n_c) &= |F_A(n_c)|^2, \text{ at } n_f \end{aligned} \quad (1.21)$$

Where  $n_f$  is the Nyquist frequency. From this, the spectral energy density can be approximated using:

$$S_A(n_c) = \frac{E_A(n_c)}{\Delta n_c} \quad (1.22)$$

For a physical process which is scale-invariant in the space or time domain, the power spectrum  $S(f)$  approaches the power law such that:

$$S(f) \propto f^{-\beta} \quad (1.23)$$

The  $\beta$  value, which is more commonly used in literature, can be found using linear regression of the log-log plot of  $S(f)$  and  $f$  (Davis et al., 1996; Harris et al., 1997; Purdy et al., 2001). Since autocorrelation is the inverse Fourier transform of the power spectral density, the  $\beta$  value shows how fast the autocorrelation decreases with lag. A higher  $\beta$  value corresponds to a steep spectral slope and thus a highly correlated process for which the contribution to the signal of low-frequency components is large in relation to the contribution from high-frequency components. A low  $\beta$  value on the other hand, corresponds to a low spectral slope, fast decreasing autocorrelation and a higher relative contribution from high-frequency components. Theoretically, the  $\beta$  value is 0 for white noise and 2 for pure Brownian noise. However, in the context of this study it was observed that fitting to single spectra of a single realisation of the signal resulted in large uncertainties for the spectral slope values. Whereas the averaging of the signals (i.e. for two-dimensional data typically some azimuthal averaging

### **1.3. Building tools for the analysis of the spatio-temporal variability of radar data**

---

is performed) has the effect of smoothing the power in the low-frequency components leading to spectral slopes which give very little information on the variability of the signal at the larger spatial scales. This is why it was chosen to base the analyses in this study on the fraction of variance explained by component. It has the advantage of summarising the information on the spatial variability into a few components, showing the relative amount of variance explained by each spatial or temporal lag. It thus allows for the comparison of individual signals as well as the aggregation of data, while preserving information on the uncertainty when presented, for example, in box plots. Still, as Eq. (1.22) and Eq. (1.23) demonstrate, the fractions of variance explained by component are related to the spectral slopes, thus facilitating comparison with existing literature.

### 1.4 Thesis outline

The objective of this thesis is to contribute to the improvement of quantitative precipitation estimation at the ground in the Alps, through the analysis of the spatial and temporal variability of polarimetric weather radar signals. This is addressed in three steps: firstly, the topic of radar monitoring and stability is considered, then the spatio-temporal variability of the melting layer in an Alpine valley is characterised and finally, a more localised vertical profile correction approach is proposed.

The accuracy of quantitative precipitation estimates depend on the accuracy and quality of the polarimetric weather radar measurements which, in turn, depend critically on the calibration and stability of the instrument. This stability may be affected by many different factors which is why it is considered good practice to combine a variety of methods and to monitor different parts of the radar chain. Chapter 2 describes a temporal monitoring approach based on the spectral analysis of the polarimetric radar signals returned by a single bright scatterer. Although the dispersion of the differential reflectivity values returned by this target is too large for calibration purposes, it is shown that valuable information on the state and stability of the radar hardware can still be obtained if different scales of variability and other polarimetric variables are considered.

The spectral analysis method used in chapter 2 to analyse the temporal variability of the radar signals, is further applied in chapter 3 to study the temporal and the spatial variability of the melting layer (ML). The ML is a typical feature in radar observations of the vertical structure of stratiform precipitation and designates the transition region from solid to liquid precipitation. It is also characterised by a well-known signature in polarimetric radar variables, facilitating its identification with automatic detection algorithms. The ML is often assumed spatially and temporally homogeneous by algorithms for QPE and vertical profile of reflectivity (VPR) correction, even though its variability remains poorly documented. Based on polarimetric X-band radar scans from two measurement campaigns, chapter 3 characterises and compares the spatio-temporal variability of the ML for summer precipitation on the relatively flat Swiss plateau and for winter precipitation in a large inner Alpine valley in the Swiss Alps. Based on the spectral analysis of the ML variables extracted from the Range Height Indicator (RHI) scans of these two campaigns, it appears that smaller spatial scales contribute more to the total spatial variability of the ML in the case of the Alpine environment.

The relative importance of the contribution of the smaller spatial scales (15 to 10 km) to the total spatial variability of the ML in the Alpine area, further underlines the need to perform vertical profile corrections at smaller scales. Building on the availability of polarimetric data and a hydrometeor classification algorithm, chapter 4 proposes a new framework for the application of machine learning methods to study the vertical structure of precipitation in Switzerland and proposes a more localised vertical profile correction method. It is shown that vertical cones extracted at 10 km intervals on a regular grid around the operational C-band radar located at Albis (938 m a.s.l.) and with a 4 km diameter at the base and 500 m vertical



resolution can well represent the vertical structure of different types (stratiform, convective, snowfall) of precipitation events. Artificial Neural Networks (ANNs) are trained with reflectivity data (dBZ only-model) and hydrometeor proportions (HC + dBZ-model) from the different altitude levels of the extracted cones in order to predict the vertical change in reflectivity. The information from the lower height levels is then gradually removed in order to test the ANN's ability to extrapolate the radar measurements from higher levels in the atmosphere.

Figure 1.5 depicts the challenges and processes related to precipitation in mountainous regions as well as the contributions of the central chapters and how these are related to each other. The final chapter, chapter 5, summarises the main contributions of this thesis and explores perspectives for possible future research.

The presented thesis is a compilation of published or to be submitted articles and therefore may contain small repetitions in the chapters. Some of these, such as the repetition of acronyms or the explanation of variables at their first mention in each chapter, have been preserved on purpose to facilitate the readability of the individual chapters.

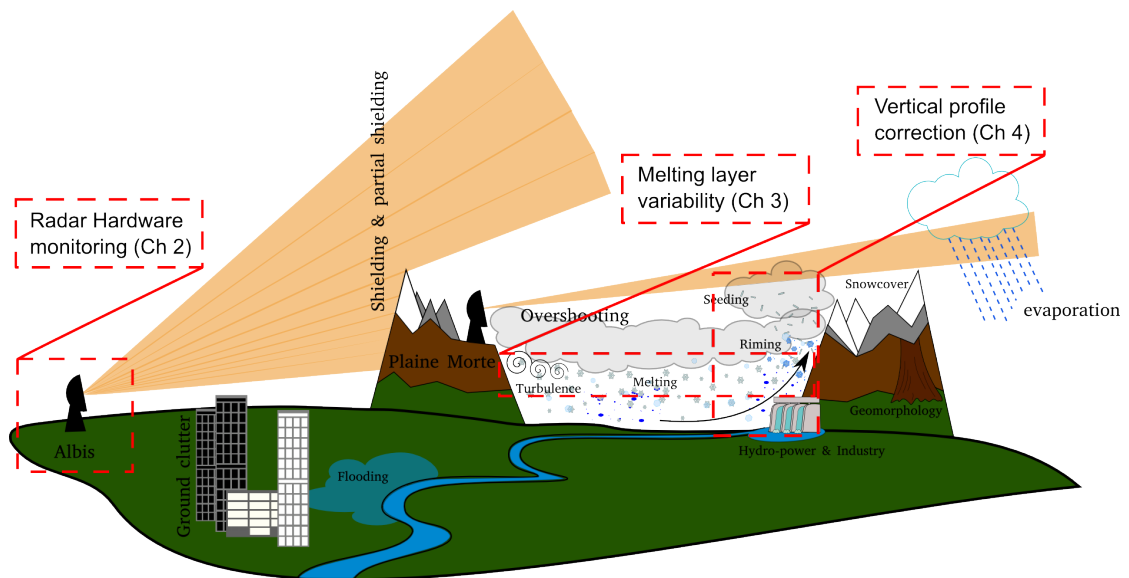


Figure 1.5 – Challenges and processes related to precipitation in mountainous regions and the contributions of the individual chapters.



## 2 Temporal monitoring of dual-polarisation weather radar

This chapter has been adapted from the manuscript:

- van den Heuvel, F., M. Gabella, M. Sartori and A. Berne, 2019: Temporal monitoring of dual-polarisation weather radar using a single bright scatterer. *Journal of Atmospheric and Oceanic Technology*, in revision.

It presents the results of a temporal monitoring approach based on the Fast Fourier Transform which was applied to the polarimetric radar signals returned by a single bright scatterer.



### 2.1 Summary

Because of the multiple factors potentially affecting the stability of a weather radar signal, it is considered good practice to combine a variety of methods to monitor different parts of the radar chain. One such method is based on the use of known values for nearby areas of spatially distributed ground clutter. The advantage of the single bright scatterer used within the context of this study is that it is relatively close to the radar, well-known and subject to little change. This work therefore aims to analyse the temporal variability of the polarimetric signatures of the target in order to identify temporal scales of variability and to assess its suitability for the monitoring of radar hardware. Six events of four consecutive clear-sky days with environmentally stable conditions have been selected for this study and subjected to a Fourier analysis. For one event the high observed variability in differential reflectivity  $Z_{DR}$  could be related to drops in copolar correlation coefficient  $\rho_{HV}$  associated with not hitting the tower correctly due to environmental influences on beam propagation. Two other events with high observed variability in  $Z_{DR}$  also showed distinct diurnal cycles. The study of the horizontal and vertical channels as well as the calibration test signals of these events pointed to an instrumental issue in the receive path of the vertical channel. Based on the calibration signal, the observed variability of the  $Z_{DR}$  values can be compensated in these cases so that it remains within usual limits.

## 2.2 Introduction

The accuracy and quality of polarimetric weather radar measurements and especially their potential use for applications such as quantitative precipitation estimation (QPE) depend critically on the stability of the instrument. Due to the variety of factors (both internal and external to the radar system) that may affect the radar signal, it is considered good practice to combine several methods for testing different points in the radar chain (Melnikov et al., 2003; Germann et al., 2015). Fortunately, the number of off-line and online approaches that are available is abundant, but each has its specific advantages and limitations (Joe and Smith, 2001; Atlas, 2002; Williams et al., 2013).

Some calibration techniques allow to test specific parts of the radar chains such as the offline Sun-tracking which allows to calibrate the receivers (Hubbert et al., 2003; Gabella et al., 2016) or the insertion of test signals at specific parts in the chain (Germann et al., 2015). Other techniques rely on the measurement of a target of which the size and backscattering properties are more or less known. As such, the measured values can be compared with the expected values for the target in question. The calibration of reflectivity ( $Z$ ) and differential reflectivity ( $Z_{DR}$ ) using a metallic sphere suspended from a tethered balloon for example, is a well-known approach though it is also considered a challenging one; requiring the absence of ground clutter, good meteorological conditions and substantial data analysis (Atlas and Mossop, 1960; Joe and Smith, 2001). Furthermore, it is complex and time-consuming to set up and therefore impractical for routine calibration (Melnikov et al., 2017). Within a radar network, it is possible to compare areas where two (or more) radars measure the same precipitation volume. However, this relative calibration method does not guarantee absolute calibration of the  $Z$  values (Melnikov et al., 2017). While absolute calibration could be achieved by the comparison of radar measurements with ground based measurements such as rain gauges, the differences in sampling volumes and the changes in the vertical profile of reflectivity (VPR) are sources of high uncertainty, especially on the short term (Germann and Joss, 2001). Methods which do not depend on any external instrumentation include the comparison of measured  $Z_{DR}$  values with climatological values (for example in light rain) and the performance of vertical scans. The first method requires sufficient past measurements for comparison, can only be performed in similar weather conditions and is sensitive to the presence of a small number of big drops (Melnikov et al., 2017). The vertical scan method is based on the assumption that in light rain and in the absence of strong wind shear, droplets are approximately spherical and thus result, on average, in  $Z_{DR}$  values close to zero when measured at vertical incidence (Gorgucci et al., 1999; Bringi and Chandrasekar, 2001). This method further requires that the radar scans at a 90 degrees inclination, which is often not performed in operational scanning routines (Borowska and Zrnic, 2012; Dixon et al., 2017; Germann et al., 2015). It also requires specific meteorological conditions which, in the case of the Swiss operational network where several of the radars are located at high altitudes, are rarely or never satisfied. A possible alternative to this is the snow method, which assumes the value of  $Z_{DR}$  in snow to be 0.2 dB at  $\sim 60^\circ$  elevation angles (Ryzhkov et al., 2005; Zittel et al., 2014; Dixon et al., 2017). This can then be compared with the observed average measured values (or some chosen percentile)

for  $Z_{DR}$  in identified snow regions. However, this method assumes that the polarimetric data quality is sufficient for the identification of snow regions in the first place. Furthermore, the characteristics of snow particles above the melting layer are not sufficiently well-known to guarantee the accuracy of this approach, and values of snow layers above the melting layer may well exceed 0.2 dB (Melnikov et al., 2017).

The techniques described above aim at correcting both the receiver and the transmitter differential bias. If the radar is sensitive enough it is also possible to separate the biases associated with the transmit and receiver paths by using the solar signal as a reference. Methods for the daily monitoring of the on-reception  $Z_{DR}$  during the operational scan are now running at several national weather services. Holleman et al. (2010) have found for the French Trappes radar a standard deviation of 0.20 dB during a 3-month quiet Sun period in 2008. Modern dual-polarization receivers seem to outperform this benchmark: Gabella et al. (2015) have obtained values of 0.05 dB (Albis radar) and 0.06 dB (La Dôle and Monte Lema radars) in Switzerland for the first 224 days in 2014, which was an active solar period. Using additional quality checks that remove weather echoes which may contaminate solar hits, Huuskonen et al. (2016) found a standard deviation as low as 0.02 dB (this number refers to a 30-day period, namely April 2015).

The identification and removal of ground clutter is an integral part of operational radar processing. Although considered highly undesirable for hydrological applications, ground clutter is increasingly used for radar hardware monitoring (Gabella, 2018). Though the idea of using ground clutter in a constructive manner is not new, it is not a very common technique. Rinehart (1978) was the first to propose the day-to-day and year-to-year monitoring of the radar calibration of reflectivity using an individual ground target which provided returns which were found to be stable within 1 dB. He also proposed an approach based on the statistical properties of multiple targets in order to better cope with changes in radar system timing and range gate spacing. Ground clutter has been subsequently used to study the antenna beam pattern (Rinehart and Frush, 1983), to estimate the attenuation at X-band caused by rainfall (Delrieu et al., 1997), to estimate the refractive index of air (Fabry, 2004) and for the calibration of spaceborne radars (Meneghini et al., 1983, 2000). Improved identification of ground clutter areas thanks to dual-polarisation as well as increased computational power have further opened up the possibility for the use of these for radar system monitoring. Near-real-time relative calibration of reflectivity can be achieved based on probability distributions of the returns from stable clutter areas located close to the radar (Silberstein et al., 2008; Borowska and Zrnic, 2012; Wolff et al., 2015). With the exception of Rinehart (1978), who worked only with reflectivity measurements, current proposed ground-clutter based calibration techniques make use of areas of ground clutter which usually comprise several thousands of radar bins. The advantage of using areas of ground clutter is that this method is more robust to offsets in radar system azimuth pointing, timing and range gate spacing (Rinehart, 1978). A possible disadvantage is that any temporal variability of the changes in the radar system may be masked by the median or average of many, temporally varying scattering objects. Another advantage of using a single bright scatterer is that the variability of the measured values is less influenced by the variability of changes in the clutter reflection coefficient due to variations in foliage or

snow cover for example. Of course, this advantage only holds if the scatterer which is used is itself sufficiently stable. Although Gabella (2018) has shown that the polarimetric signals of the Cimetta tower located in Locarno, Switzerland can be remarkably stable, the study also concluded that the dispersion of the  $Z_{DR}$  values for this single bright scatterer was too large for calibration purposes. The results from the study by Gabella (2018) have motivated the analysis of the temporal variability of the signal returned by the same bright scatterer in order to evaluate whether it is possible 1) to identify periods within the day for which the variability of  $Z_{DR}$  values may be lower, and 2) to use the signal to identify hardware issues. To our knowledge, this is the first study into the temporal variability of the returns of a single ground target.

Section 2.3 will briefly introduce the bright scatterer, the dataset of clear-sky days, the (polarimetric) variables used in this study and the Fourier transform-based method to study the temporal variability of these variables. A first assessment of the event-based variability will be presented in section 2.4 followed by a more in depth analysis of the temporal variability of the signal returned by the bright scatterer with a focus on events for which high variability was observed. The potential of using this target for the identification of radar hardware issues is evaluated in section 2.5 and the conclusions are presented in section 2.6.

## 2.3 Data and Methods

The bright scatterer under study is a metallic tower situated on top of the Cimetta mountain at approximately 1632 m a.s.l. and 18.14 km distance from the Monte Lema radar. The tower is 90 metres high and surrounded by grass (no trees) and a few small buildings. Based on the analysis of five clear sky days, Gabella (2018) found median reflectivity values for the Cimetta tower to be 81.5 (80.5) dBZ for horizontal (vertical) polarisation. Given a reflectivity value of 81 dBZ, the radar cross section (RCS) of the tower can be estimated at 42.2 dB m<sup>2</sup>, or approximately 16600 m<sup>2</sup> which corresponds to an equivalent sphere of 73 m. This value is reasonably close to the height of the tower, considering that it is not a spherical target. As such, it can be considered the predominant target in the radar bin (Fig. 2.1).

For this work, four days out of the dataset of five clear sky days studied by Gabella (2018) (5 January 2015, 9 February 2015, 10 February 2015 and 18 January 2017) have been extended with additional clear-sky days surrounding these, and two new sets of four consecutive clear-sky days have been added, so that the dataset consisted of six sets of four day events. The choice for the four day duration of the events was a trade-off between the need to have sufficiently long samples to perform temporal analyses up to the 24 hour scale and the availability of events with four consecutive days of clear-sky conditions. The events were selected from the historical radar archive based on the criterion of zero precipitation accumulation over 96 hours within the Monte Lema radar umbrella.

The MeteoSwiss dual-polarisation Doppler C-band radar is located at 1625 m a.s.l. at Monte Lema in the vicinity of Lugano (Switzerland). Like the other radars in the MeteoSwiss network,



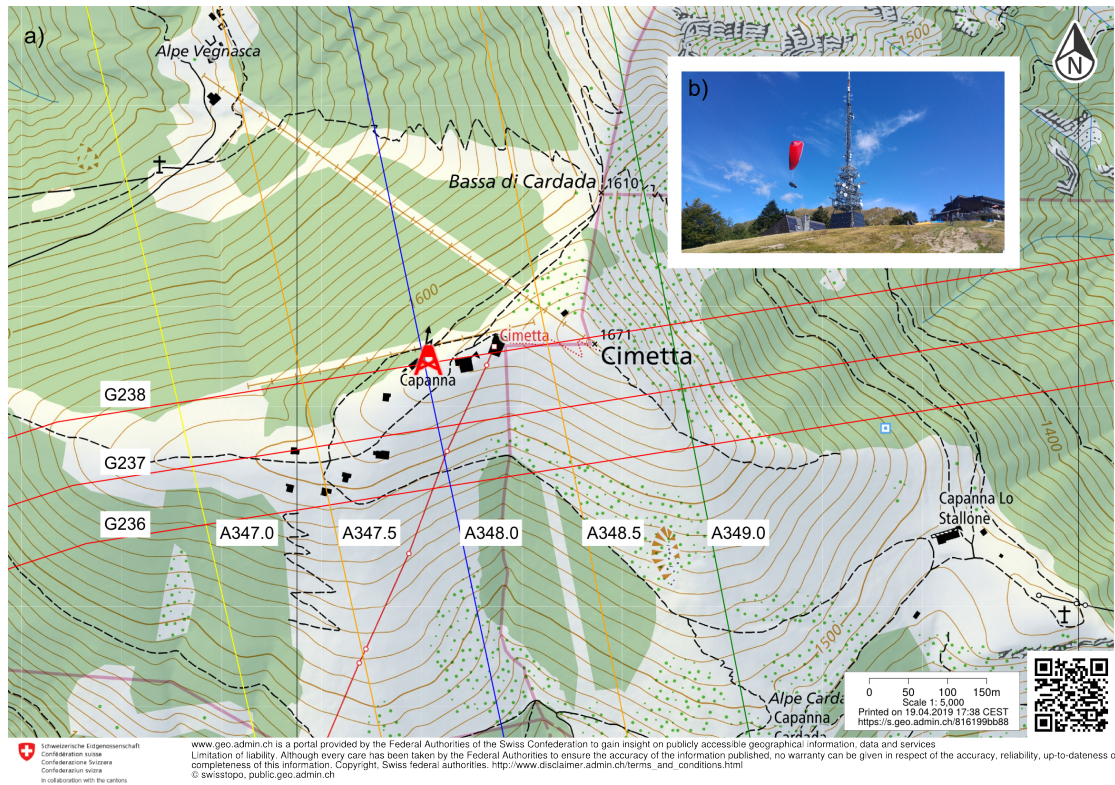


Figure 2.1 – The location of the Cimetta tower (a) and its immediate surroundings (b). The blue line indicates the azimuth of the center of the radar bin under study and the red lines indicate the ranges.

the Monte Lema radar performs 20 plan position indicator (PPI) scans at elevations ranging from  $-0.2^\circ$  to  $40^\circ$  within 5 minutes (Germann et al., 2015). The lowest elevation  $360^\circ$  PPI scan takes 20 s to compute, and the radar points at each  $1^\circ$  azimuth angle for  $1/18$  s. The Cimetta tower is measured by the lowest elevation beam of the radar for which the PRF is 600 Hz which means that every 5 minute observation of the tower is based on the spectral analysis of  $600/18 \approx 33$  pulses (Germann et al., 2015; Gabella, 2018). For this study, the reflectivity measured at the horizontal ( $Z_H$ ) and vertical ( $Z_V$ ) polarisations, differential reflectivity ( $Z_{DR}$ ) and the copolar cross correlation coefficient ( $\rho_{HV}$ ) are used. The  $Z_H$  and  $Z_V$  data are stored with 0.5 dBZ quantisation, while for  $Z_{DR}$  data is stored within a range of 15.751 dB at 0.062 quantisation, centered around 0 dB.

For the monitoring and calibration of the radars in the MeteoSwiss network, several independent sources of information are used. Automatic hardware calibration is partly achieved through the use of a noise source signal which is inserted every 2.5 minutes in the receive path of both polarisation channels (Germann et al., 2015). The measured values of this signal (the noise source power on frontend h and v [dBadu]) as well as their ratio (differential noise source power on frontend [dB]) will also be considered in this study and referred to as the  $CAL_{dr}$  signal. The daily variances of  $Z_{DR}$ ,  $Z_H$  and  $Z_V$  as well as for the the noise source power on frontend h and v and  $CAL_{dr}$  signal for all events are given in Table 2.1. It can be seen that the March 2015



and January 2017 events stand out with a variance of  $Z_{DR}$  which was uncharacteristically high (typically 1 dB for the tower (Gabella, 2018)). More information on the calculation of the radar observables, the scan strategy and operational radar calibration can be found in Vollbracht et al. (2014), Germann et al. (2015) and Gabella (2018).

Event	Polarimetric variables (var)			noise source power on frontend (var * 1000)		
	$Z_{DR}$ [dB <sup>2</sup> ]	$Z_H$ [dBZ <sup>2</sup> ]	$Z_V$ [dBZ <sup>2</sup> ]	CAL <sub>h</sub> [dBadu <sup>2</sup> ]	CAL <sub>v</sub> [dBadu <sup>2</sup> ]	CAL <sub>dr</sub> [dBadu <sup>2</sup> ]
Jan 5-8 2015	0.4	1.1	2.1	2.3	1.4	0.2
	0.4	1.1	1.4	5.2	3.2	0.3
	0.7	1.1	1.6	2.6	1.5	0.2
	0.5	1.0	1.6	3.1	1.6	0.4
Feb 9-12 2015	0.5	0.4	0.7	2.3	0.5	0.9
	0.6	0.5	1.1	6.1	3.6	0.4
	0.5	1.9	1.9	6.6	4.1	0.4
	0.4	0.7	1.1	6.7	4.0	0.5
March 6-9 2015	0.8	1.7	2.7	5.3	1.8	1.1
	3.8	2.9	<b>9.6</b>	1.5	0.3	0.7
	1.3	1.1	3.2	5.5	2.5	0.7
	1.1	<b>6.4</b>	<b>8.2</b>	5.4	2.7	0.5
Jan 18-21 2017	1.0	0.6	1.1	0.6	1.7	0.5
	0.8	0.5	1.0	0.5	1.4	0.4
	0.7	0.7	1.1	0.8	1.8	0.4
	3.7	0.6	2.9	1.1	12.5	6.9
Jan 25-28 2017	<b>3.9</b>	0.7	<b>4.2</b>	1.2	8.6	4.2
	<b>4.2</b>	0.7	<b>4.3</b>	1.3	8.4	4.0
	1.7	1.7	1.9	0.3	2.5	1.2
	<b>4.2</b>	1.3	<b>5.2</b>	0.6	10.2	6.5
Jan 11-14 2018	1.4	0.9	2.5	10.2	10.9	0.1
	0.9	1.0	2.3	0.5	0.2	0.2
	2.5	1.4	<b>4.6</b>	0.9	0.3	0.3
	1.3	1.3	1.7	0.5	0.1	0.3

Table 2.1 – Daily variances of  $Z_{DR}$ ,  $Z_H$  and  $Z_V$  as well as for CAL signal H, V and H-V. For all events, and ranking of event in **Poor** (>3.8), *Intermediate* (>2.2) or Good.

In order to avoid variability in the measurements of the Cimetta tower due to changes in atmospheric refraction, non-normal propagation conditions were avoided as much as possible by choosing clear-sky days and winter events. As Fig. 2.2 illustrates, under normal propagation conditions ( $dN/dh = -40 \text{ km}^{-1}$ , where  $N$  is the refractivity and  $h$  is the height in km; see also the appendix) the top part of the lowest elevation radar beam (-0.2 degrees) is occupied by the tower. At these distances, the shift in the height of the center of the beam would be approximately + 5 metres in the case of sub refraction ( $dN/dh = 0 \text{ km}^{-1}$ ) and -20 metres in the case of super refraction ( $dN/dh = -150 \text{ km}^{-1}$ ). Consequently, in the best case the tower occupies one-third of the height of the beam (beam width diameter equals approximately 316 metres at 18 km distance) and in the very worst case of super refraction one-fifth of the beam height. As such, it may be expected that non-normal propagation should not greatly affect the measured value for the tower. However, to ascertain that changes in the refractive index indeed did not play a role during the selected events,  $dN/dh$  was calculated based on pressure, air temperature and humidity measurements at the meteorological stations of Cimetta and Matro

## Chapter 2. Temporal monitoring of dual-polarisation weather radar

(situated ~26 km North-East of Cimetta, at 2171 m a.s.l.). The median, standard deviation and quartiles of the calculated refractivity are given in Table 2.2 and indicate that normal propagation conditions were predominant during the selected events, with perhaps some sub refraction which could have caused for the center of the radar beam to have hit the tower slightly higher (but much less than 5 metres higher) than under normal conditions.

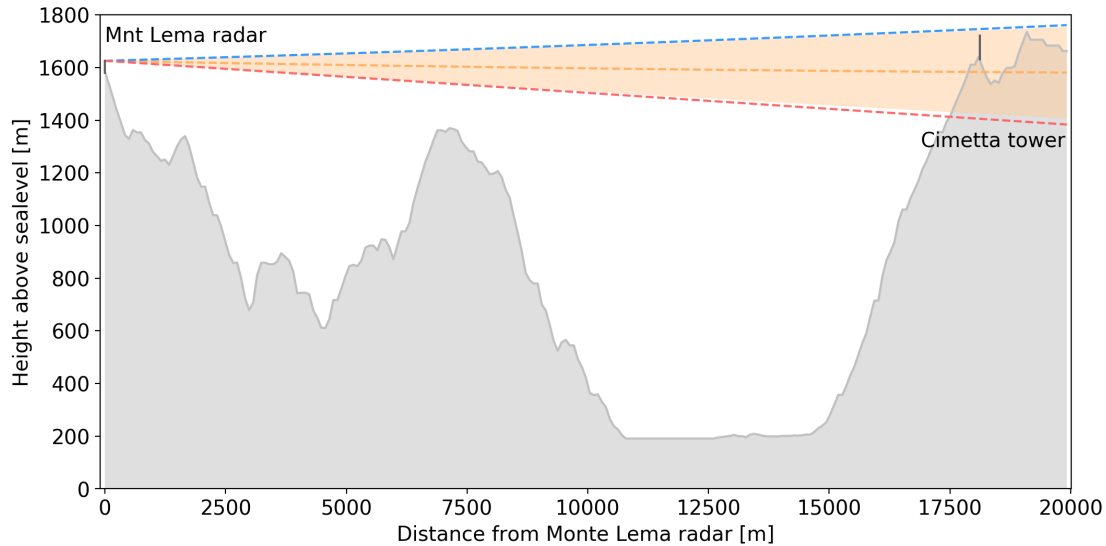


Figure 2.2 – Theoretical path of the center of the beam (-0.2 degrees elevation) for normal propagation conditions (orange line), with the 3 dB beam width in shaded orange. The blue line gives the top of the 3 dB beam (0.3 degrees elevation) under sub refractive conditions and the red line the bottom of the 3 dB beam (-0.7 degrees elevation) under super refractive conditions.

Event	Median	Std	Q1	Q3
Jan 5-8 2015	-31.6	11.6	-41.7	-21.9
Feb 9-12 2015	-27.0	5.9	-32.9	-23.9
March 6-9 2015	-43.2	14.4	-53.5	-26.9
Jan 18-21 2017	-29.0	4.4	-31.9	-26.3
Jan 25-28 2017	-31.5	5.9	-36.1	-28.9
Jan 11-14 2018	-30.9	6.3	-34.6	-24.5

Table 2.2 –  $dN/dh$  calculated between Cimetta and Matro, median, standard deviation and quartiles.

### 2.3.1 Fractions of variance explained by component

For the study of the temporal variability of the Cimetta tower's backscattered signal the fraction of variance explained by component is used. This can be obtained by dividing the square of

the norm of the complex Fourier transform by the total variance of the signal:

$$\frac{|\mathbf{F}_A(n)|^2}{\sigma_A^2} = \frac{\mathbf{F}_{\text{Re}}^2(n) + \mathbf{F}_{\text{Im}}^2(n)}{\sigma_A^2} \quad (2.1)$$

In order to illustrate the type of information obtained from this method, the top panel in Fig. 2.3 shows the fraction of variance explained by component for 6 example signals generated over a period of four days. The signals include 5 artificial signals and one temperature time series measured at the Monte Lema radar for 25-28 January 2017. The artificial signals include a Brownian noise signal which is based on the average of 9 random walks, one white noise signal to which a linear trend was added and one regular white noise signal, one sine wave with 2 periods and one sine wave with four periods. The bottom panel of Fig. 2.3 gives for the same signals the more commonly used power spectra with the fitted spectral slopes ( $\beta$  values), the values of which depend critically on the fitting process and pre-processing of the data. In Fig. 2.3 for example, the slopes have been calculated on the first 12% of the data, while a fit on all of the data would result in  $\beta$  values of  $1.81 \pm 0.05$  for Brownian noise,  $0.56 \pm 0.06$  for white noise with a trend,  $0.08 \pm 0.06$  for regular white noise,  $1.04 \pm 0.16$  for a sine wave with 2 periods,  $0.92 \pm 0.16$  for a sine wave with four periods and  $2.10 \pm 0.06$  for the temperature data. Fitting to the entire spectra reduces the uncertainty of the fit, but also gives more weight to the high frequency values with the effect of flattening the  $\beta$  slope. Similarly, detrending and tapering the data before performing the Fourier transform also have the effect of respectively decreasing the spectral energy in the low / high frequencies and thus of decreasing / increasing the spectral slopes. While it is usually recommended to perform detrending and tapering before performing the spectral analysis (Stull, 1988), it was not deemed necessary for this study since the polarimetric signals of the Cimetta tower showed little to no trend over the course of four clear-sky days. Thus pre-processing the data would incur a risk of introducing artefacts in the signals.

Finally, Fig. 2.3 shows another advantage of using the fraction of variance explained by component over the spectral slope values: while it is immediately clear that the temperature data displays a diurnal cycle, this is not at all apparent from the  $\beta$  value of this signal. The artificial signals have been included for illustration purposes. Brownian noise, for example, typically has a  $\beta$  of 2, while white noise has a  $\beta$  of 0. In the fractions of variance explained by component, the white noise signal displays equal amplitudes across the whole frequency range. The Brownian noise signal (much like a signal with a trend in this case) is considered as a signal with a time period which is longer than the sampling period and is thus fit by the Fourier transform with waves of the fundamental period and shorter. Hence, a spike at the lowest frequency and leakage to higher frequencies can be observed in the fraction of variance explained by component plots. Finally, the two sine waves show how waves with two and four periods appear with a single spike at the second and fourth component.

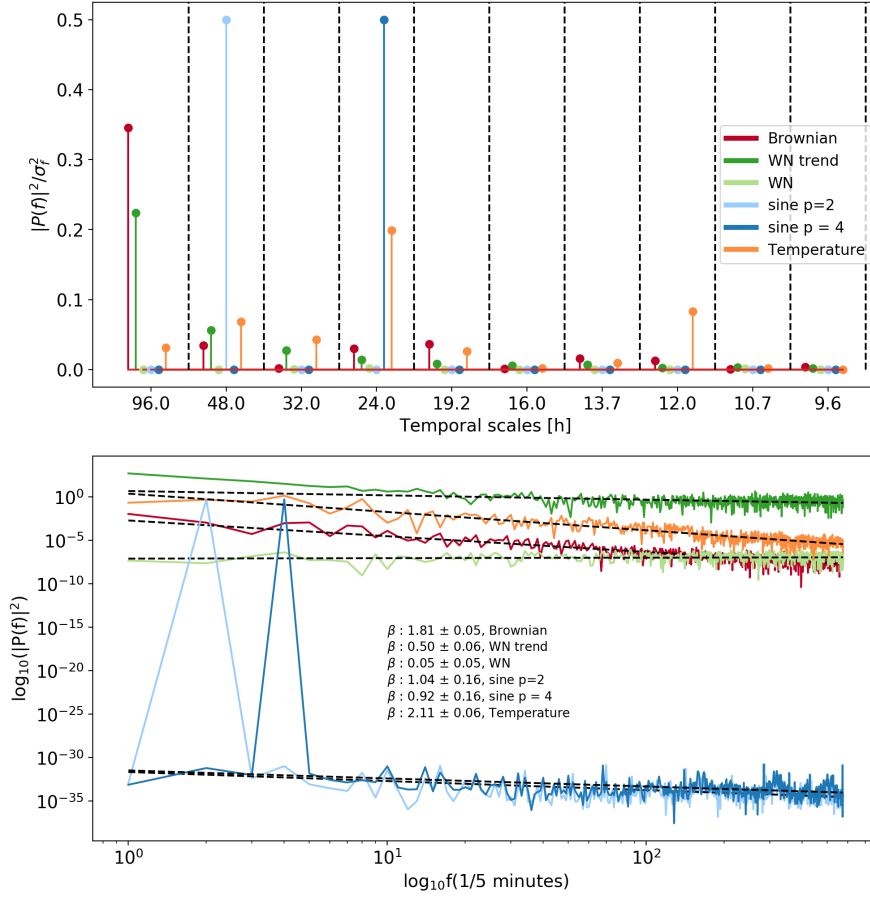


Figure 2.3 – Top: fraction of variance explained by component for example signals. Bottom: folded spectra of the same signals.

This study will also present results using the non-normalised variance explained by component. The reason for this is that there were cases where, for example, the  $Z_{DR}$  demonstrated high variance, and as such the absolute values are also of interest. The non-normalised variance is simply  $|F_A(n)|^2$  or the discrete variance (or energy) spectrum (Stull, 1988). Finally, it should be kept in mind that the first component of the fraction of variance explained by component is based on a single realisation of four days, and thus also has a larger uncertainty than subsequent components.

## 2.4 Data analysis and results

In the first part of this section, the overall distributions of  $Z_{DR}$ ,  $Z_H$  and  $Z_V$  on an event-basis, as well as the more general sub-daily variability will be discussed. The second part will focus specifically on the events displaying large variability.

### 2.4.1 Event and sub-daily variability

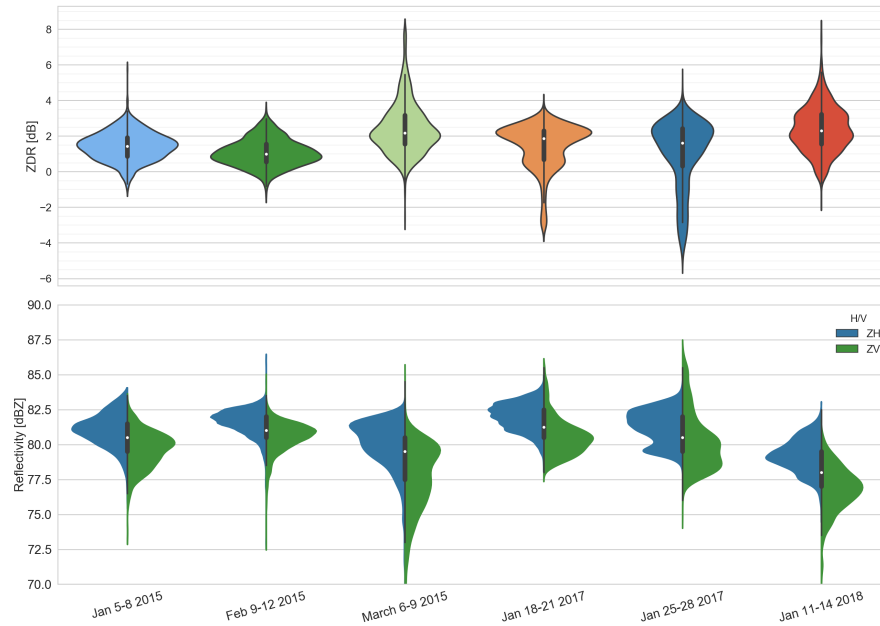


Figure 2.4 – Violin plots for  $Z_{DR}$  (top panel) and  $Z_H/Z_V$  (bottom panel) on an event basis. Boxplots of the combined  $Z_H/Z_V$  data are represented in black inside the violin plots with a white dot indicating the median value, the box indicating the interquartile range (IQR) and the black lines representing the whiskers extending towards  $1.5 \cdot \text{IQR}$ .

The distributions of  $Z_{DR}$ ,  $Z_H$  and  $Z_V$  on an event basis are shown in the violin plots in Fig. 2.4. It appears that the median  $Z_{DR}$  values (top panel) of the Cimetta tower are around 1 dB as reported in Gabella (2018) for the first two events, but higher (around 2 dB) for the last four events. The tails of the distributions in the March 2015 and January 2017 events are longer, with more positive outliers for the March 2015 event and more negative  $Z_{DR}$  values for the January 2017 events. The bottom panel of Fig. 2.4, which shows the separate distributions for the H and V channels, indicates that the variability of the vertical channel is higher overall and especially for March 2015. Since this study seeks to evaluate the potential of using the Cimetta tower for monitoring of the Monte Lema radar hardware, it is important to consider whether there are periods in the day during which the variability of the measurements is higher. Three hour periods were chosen, and because each event consists of four days and the tower is sampled every five minutes, this results in 144 samples for each three hour time period.

Figure 2.5 shows the violin plots for the individual events, subdivided into 3 hour time periods. With the exception of the March 2015 and January 2018 events, the figures show a relatively good stability in the H channel (right-most column, blue plots) with values which remain within 0.9 dB from the median (81.5 dBZ). The double-peakedness in, for example, the 3-6 hours period in the H channel for the 9-12 February 2015 event (Fig. 2.5, 2<sup>nd</sup> row, 2<sup>nd</sup> column) can be attributed to the quantisation of the values. It can also be observed that  $Z_{DR}$  decreases (to around 0 dB and -1.5 dB) for the two January 2017 cases in the periods from midday

to 18:00 hours and in both cases due to an increase in the values measured by the vertical channel, while the horizontal channel remains unchanged (Fig. 2.5 4<sup>th</sup> and 5<sup>th</sup> rows). For the March 2015 and January 2018 cases,  $Z_{DR}$  is higher (2.5 dB) especially in the time period from 09:00 to 21:00 due to a decrease of roughly 3 dB in the vertical channel in these same time periods which is partly (but not completely) offset by a decrease in the values measured in the horizontal channel (Fig. 2.5, on the 3<sup>rd</sup> and 6<sup>th</sup> rows). This is in line with what can also be observed in Table 2.1, and which is expressed in equation 2.2 that if the variability in both channels is high, this can still result in low variability in  $Z_{DR}$  provided that the two channels co-vary. However, if one of the channels performs poorly (high variability) and the other is reasonably stable, covariance between the channels will also be lower and variability in  $Z_{DR}$  will increase.

$$\text{Var}[\mathbf{H} - \mathbf{V}] = \text{Var}[\mathbf{H}] + \text{Var}[\mathbf{V}] - 2\text{Cov}[\mathbf{H}, \mathbf{V}] \quad (2.2)$$

Where  $\mathbf{H}$  and  $\mathbf{V}$  are arrays of discrete temporal series of reflectivity samples in dBZ. The typical values for reflectivity reported by Gabella (2018) were 81.5 dBZ ( $\pm 0.90$  dB) for the horizontal channel and 80.5 dBZ ( $\pm 1.21$  dB) for the vertical channel. The additional data presented here corroborate the higher values for the H channel as well as the higher variability of the V channel. However, though the event medians in Fig. 2.4 indicate that values in the horizontal channel may vary between 79.0 dBZ and 82.0 dBZ and between 77.0 dBZ and 80.5 dBZ in the vertical channel<sup>1</sup>, the within event variability of both channels in Fig. 2.5 shows a more complex picture with periods of low variability ( $\pm 0.9$  dB) and periods of high variability (in the order of  $\pm 3$  dB) within the day. These temporal scales will be investigated in more detail in the following section.

---

<sup>1</sup>the lowest values reported in this study are related to the January 2018 case which was not included in the paper by Gabella (2018)

## 2.4. Data analysis and results

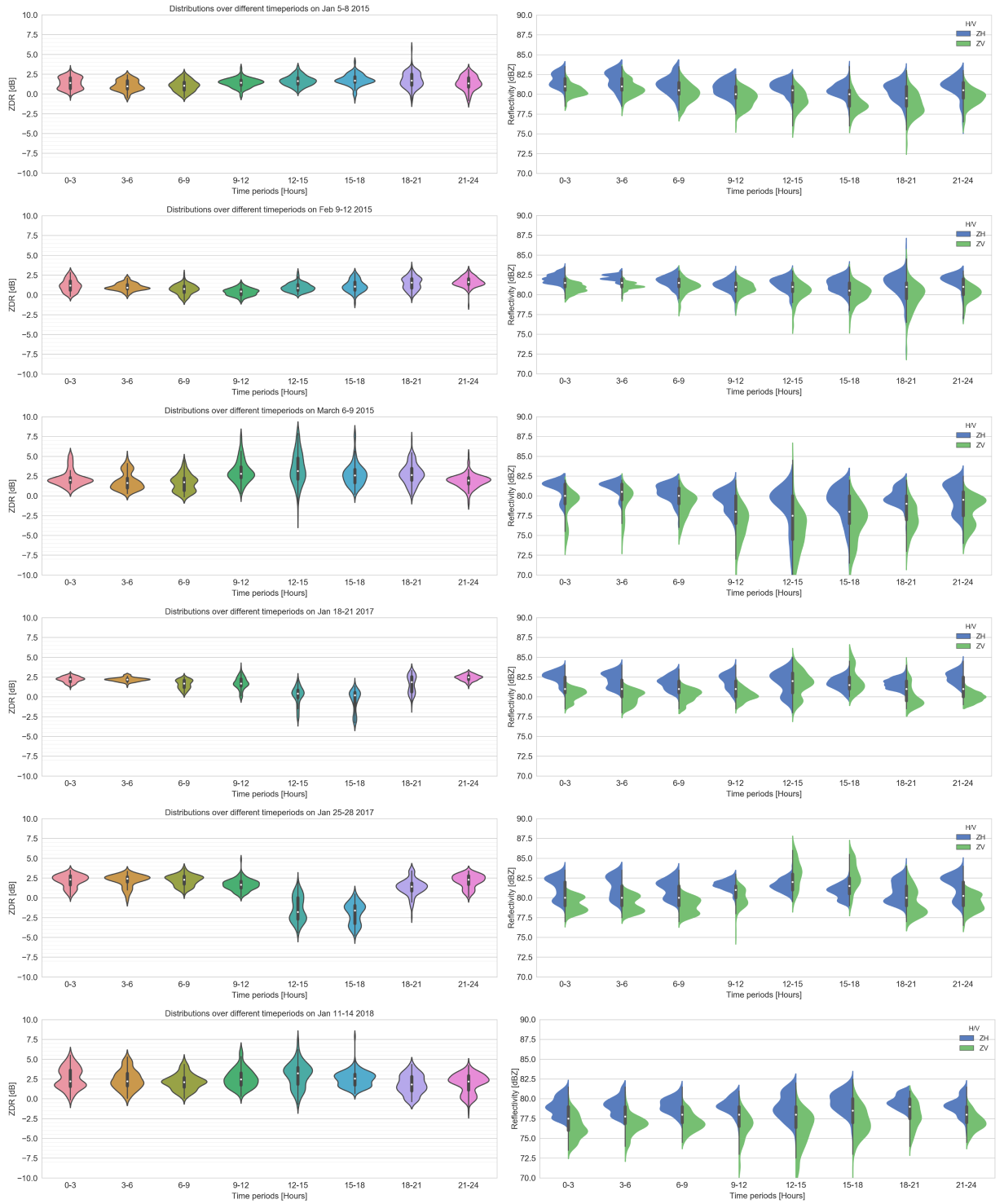


Figure 2.5 – Violin plots for events (top to bottom),  $Z_{DR}$ ,  $Z_V/Z_H$  (left to right) and specific time periods (x-axes).

### 2.4.2 Typical scales of variability

The daily variances in  $Z_{DR}$  for the March 2015 and January 2017 events well exceeds the daily variances of the January 2015 and February 2015 events (Table 2.1). The variability observed during the clear sky days in January seems to be concentrated during daytime (9:00 to 21:00 in March) and specifically in the afternoon (12:00 to 18:00 in January). The time series and the variance explained by component based on the Fourier transform were therefore analysed in order to better identify the presence of possible daily cycles in the measurements. Figure 2.6 shows the variances explained by temporal lags ranging from almost four days to 10 hours. The 25-28 January 2017 event displays a very strong diurnal component in  $Z_{DR}$  and  $Z_V$  with a peak in power at the 24 hour scale. The 12 hour peak of the same event is related to a reversal or dip of the  $Z_{DR}$  signal within the 24 hour cycles (Fig. 2.7, lowest panel). A less pronounced diurnal cycle can be observed in the 18-21 January 2017 event while the March 2015 event shows pronounced daily cycles in  $Z_H$  and  $Z_V$  resulting in a more negligible daily cycle in  $Z_{DR}$ . The other events show behaviour more or less similar to white or Brownian noise signals.

The full time series of the three events are shown in Fig. 2.7 with  $Z_{DR}$ ,  $Z_V$  and the differential noise source power on frontend (CAL<sub>dr</sub> signal) in the top panels of each plot and the internal and external temperature values and copolar correlation coefficient ( $\rho_{HV}$ ) in the bottom panels of the plots. It is clear that the diurnal cycles observed in  $Z_{DR}$  for the two January 2017 events are caused by variability in the vertical channel, and that the peaks in  $Z_V$  are slightly lagged ( $\sim 2$  hours) with peaks in the outside temperature. The vertical noise source power on frontend test signal seems to be affected by the same phenomenon as the vertical channel.

Clearly, the variability observed in  $Z_{DR}$  for the March 2015 event is not affected by the phenomenon highlighted in the two January 2017 events, which manifests itself as a high correlation ( $< 0.5$ ) between the CAL<sub>dr</sub> signal and  $Z_{DR}$ . As already indicated by the FFT output in Fig. 2.6, the diurnal signal in  $Z_{DR}$  is much smaller and the CAL<sub>dr</sub> signal behaves normally. The  $\rho_{HV}$  values have therefore been plotted as a proxy for how well the beam hits the Cimetta tower. The copolar correlation coefficient is the module of the complex correlation coefficient between two complex numbers which represent the magnitude of the backscattered signals of the orthogonal polarisation (Fabry, 2015). Hence, it ranges between 1 for perfect correlation and 0 for no correlation. If targets in the radar volume have identical shapes, the fluctuations in the returned radar signal will be identical at both polarisations thus resulting in a  $\rho_{HV}$  close to 1. If targets in the radar volume have varied shapes, the fluctuations in the H and V channels will become dissimilar and result in higher variability in  $Z_{DR}$  and lower values for  $\rho_{HV}$  (Bringi and Chandrasekar, 2001; Fabry, 2015).



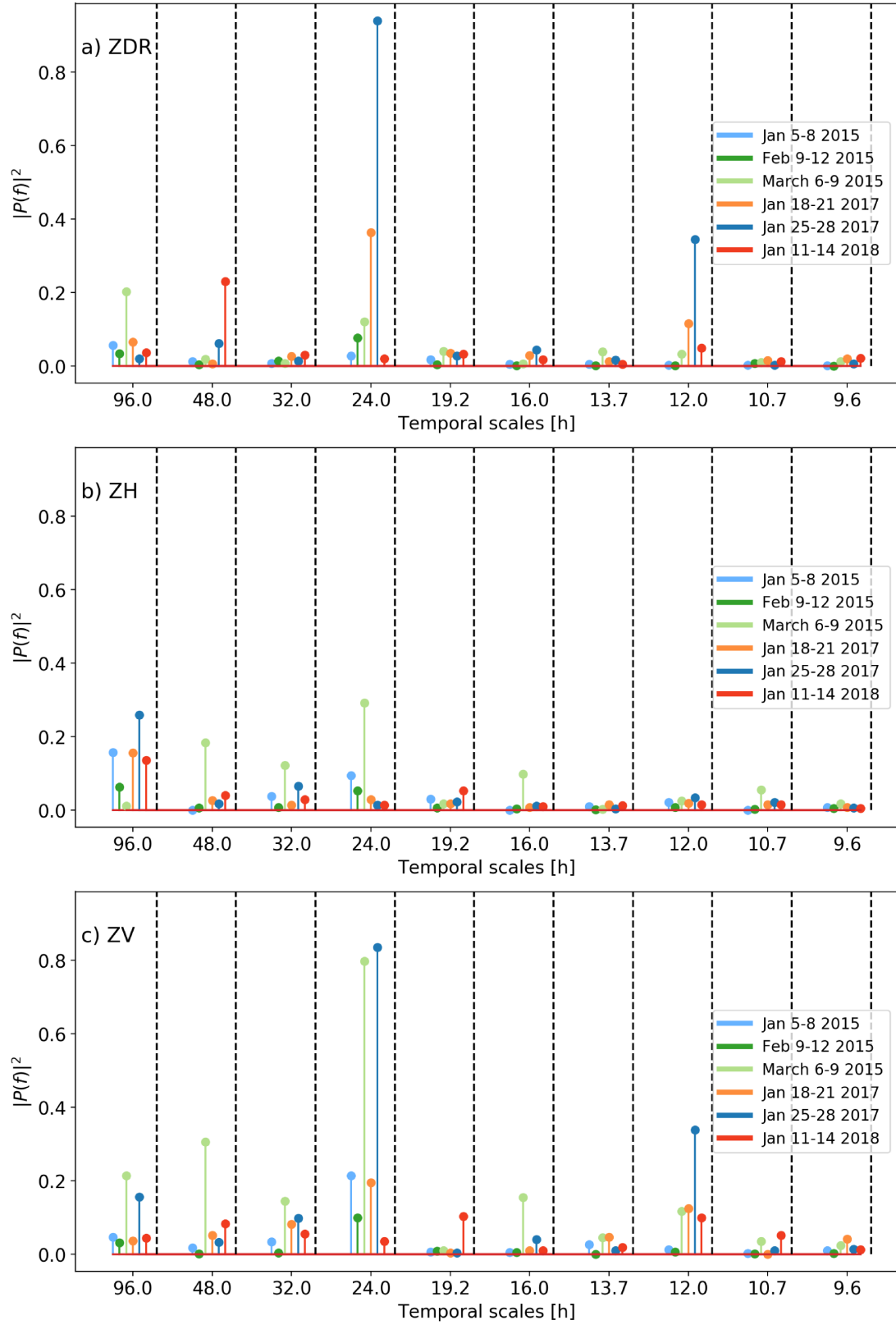


Figure 2.6 – Stem plots of the amounts of variance in the  $Z_{DR}$  (top)  $Z_H$  (middle) and  $Z_V$  (bottom) measurements explained by each temporal lag, for all of the events.

## Chapter 2. Temporal monitoring of dual-polarisation weather radar

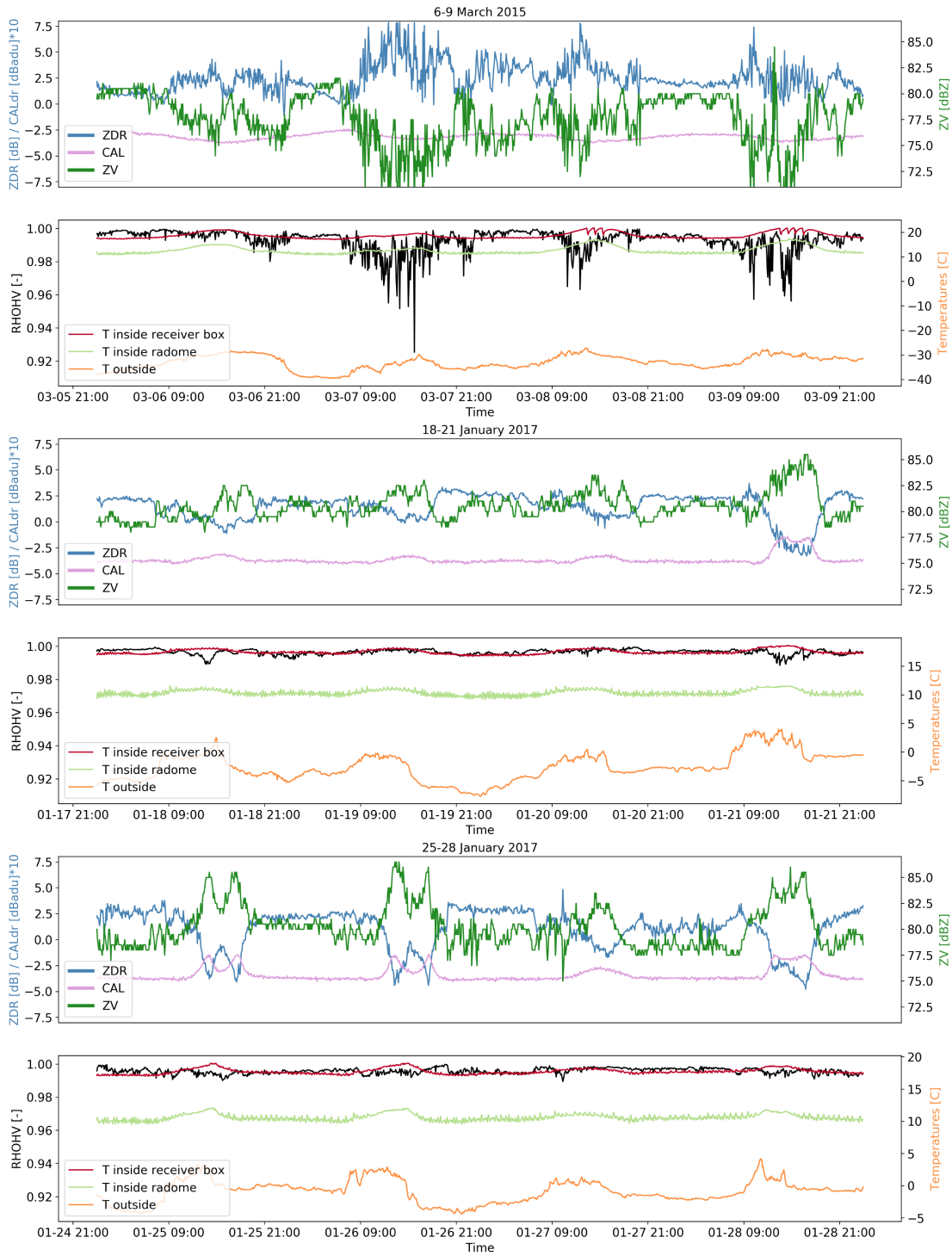


Figure 2.7 – Timeseries of  $Z_{DR}$ ,  $Z_V$ ,  $CAL_{dr}$  signal, Outside temperature and  $\rho_{HV}$  for 6-9 March 2015, 18-21 January 2017 and 25-28 January 2017. The outside temperature values for the March time series had a constant bias and have been corrected with values from a nearby station.

While the shape of the Cimetta tower remains unchanged, the radar beam may hit the tower somewhat differently from one pulse to the next over the total of 33 pulses (which can be expected for a moving antenna). As such, the shape of the Cimetta tower as observed by the radar will change between subsequent pulses, and it will change differently for the two channels which will lead to a reduction in correlations between the two channels. Typical  $\rho_{HV}$  values for ground clutter are between 0.75 and 0.95 (Fabry, 2015), however, the Cimetta tower being a single target, daily median  $\rho_{HV}$  values ranging between 0.9941 and 0.9985 have been obtained (Gabella, 2018). During the March 2017 event, periods of increased variability in  $Z_{DR}$  and  $Z_V$  coincide clearly with periods of reduced  $\rho_{HV}$  ( $\rho_{HV} > 0.98$ ) (Fig. 2.7). For the two January 2017 events, if there is any such a coincidence between  $\rho_{HV}$  drops and variability in  $Z_{DR}$  and  $Z_V$  it is drowned out by the daily cycles.

In order to summarise the above mentioned relationships between  $Z_{DR}$ ,  $Z_V$  and the  $CAL_{dr}$  signal, the outside temperature and drops in  $\rho_{HV}$ , correlation coefficients are given in Table 2.3. The correlation coefficient is a type of normalised covariance and therefore also gives a measure of the linearity of the relationship between two variables. Multiplying the correlation coefficient with the standard deviations of the two signals would result in the covariance (and thus refers back to the relationship described in eq. 2.2). The two January events show much lower correlations between the H and V channels and much higher correlations with outside temperature than all the other cases, while the March event has the highest correlation between  $Z_V$  and  $\rho_{HV}$  of all events. Interestingly, the correlation between  $Z_V$  and temperature increases when the temperature is shifted two hours forward indicating a lag in the relationship between the two. Fitting of the two signals on each individual 24 hour period of the events indicated that even higher correlations (up to 0.8 for 24 hour periods) could be found for temporal shifts between 2 to 4 hours. This shift was not necessarily incremental or decremental over the four day period, so that a buildup of heat inside the radome or inside the receiver box can not be affirmed (and is also not visible in any the temperature measurements recorded inside the radar (Fig. 2.7)).

Event	$[Z_H, Z_V]$	$[Z_V, T]$	$[Z_V, T_{+2H}]$	$[Z_V, RHO]$	$[Z_{DR}, CAL_{dr}]$	$[Z_{DR}, Z_H]$	$[Z_{DR}, Z_V]$
Jan 5-8 2015	0.797	-0.08	-0.16	0.41	-0.39	0.12	-0.49
Feb 9-12 2015	0.729	-0.04	-0.11	0.25	-0.29	0.16	-0.54
March 6-9 2015	0.819	-0.39	-0.28	0.64	-0.25	-0.20	-0.72
Jan 18-21 2017	0.392	0.32	0.54	-0.05	-0.83	0.32	-0.73
Jan 25-28 2017	0.394	0.40	0.61	-0.16	-0.91	0.19	-0.82
Jan 11-14 2018	0.625	-0.09	-0.09	0.44	-0.35	0.08	-0.71

Table 2.3 – Correlation coefficients  $Z_{DR}/Z_V$ ,  $Z_V/CAL_{dr}$ ,  $Z_V$ /temperatures and  $Z_V/Z_H$

The advantage of the fraction of variance explained by component is that temporal shifts do not matter such that the similarity or dissimilarity in the degrees of variation of the signals within specific time lags can be better assessed. Figure 2.8 shows the fractions of variance

explained for all the events and for all the signals under study. Under normal circumstances, for the  $CAL_{dr}$  signal something similar to a white noise signal or a Brownian noise signal in case of a small drift could be expected. Similarly, it seems reasonable to expect for  $\rho_{HV}$  a randomly varying (white noise) signal around the value 0.99 (Gabella, 2018). If less than 5% explained variance for a specific time lag is considered negligible, and the first component is neglected (as it is based on a single realisation) the purple line in Fig. 2.8 indicates that this is indeed the case for many of the clear-sky days with the most notable exception of 6-9 March 2015 and 11-14 January 2018. For both events, it can be observed that the principle scales of variability for  $\rho_{HV}$  are on the 48 and 24 hour time scales (Fig. 2.8).

For most of the clear-sky events the  $CAL_{dr}$  signal also shows a small peak in the variability at the 24 hour scale, which is most pronounced for the March 2015 event (Fig. 2.8). These diurnal cycles are also well visible in the time series in Fig. 2.7 and should in most cases be related to its function of correcting for temperature variations inside the receiver box.

In the following section all these different sources of information will be combined for the evaluation of the potential of the Cimetta tower for radar hardware monitoring.

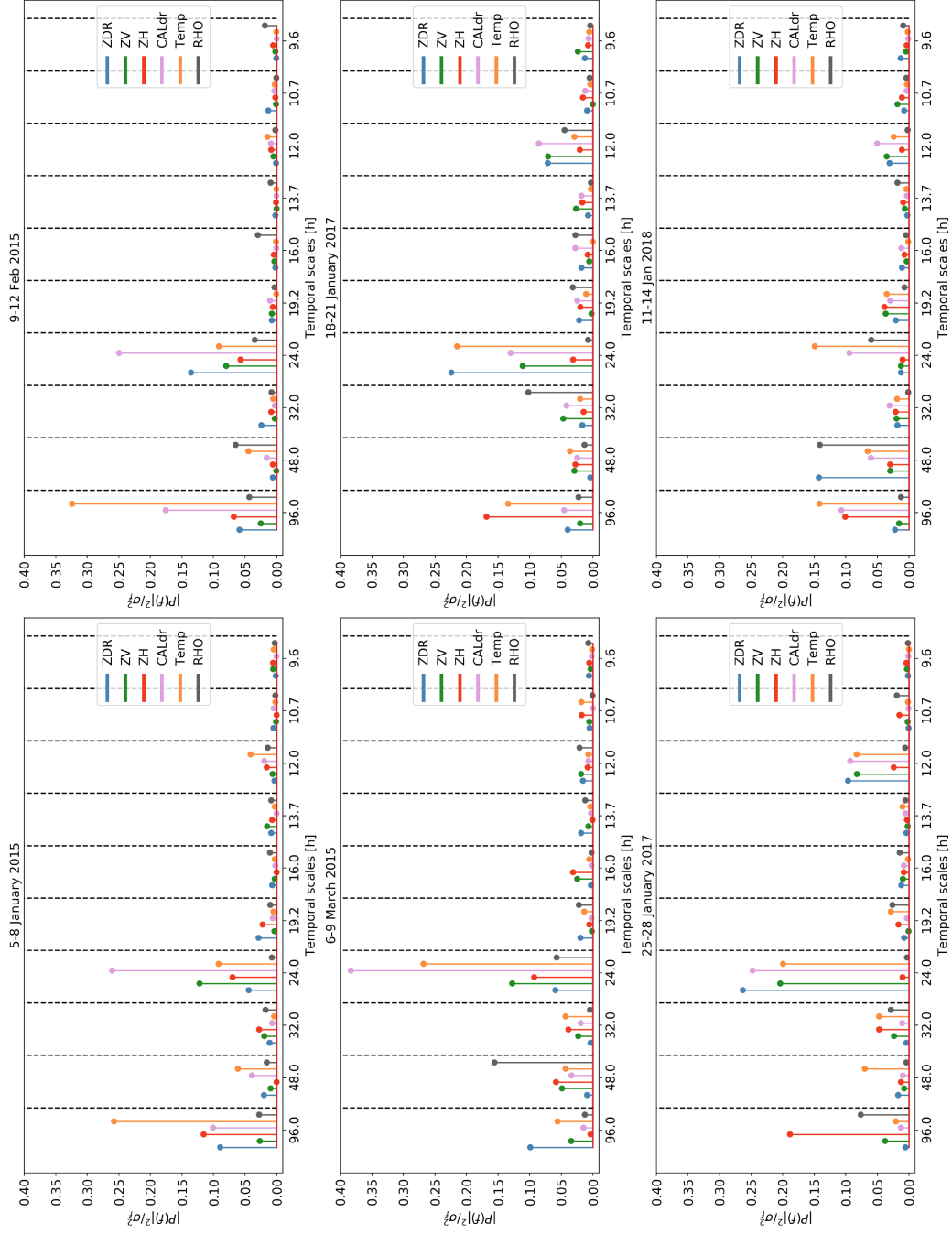


Figure 2.8 – Stem plots of the fractions of variance explained for all of the signals under study, for all of the selected events.

### 2.5 Discussion

A previous analysis by [Gabella \(2018\)](#) of the polarimetric values returned by a single bright target which is the Cimetta tower, indicated that this object could be used to monitor the hardware of the operational dual-polarisation Doppler C-band radar at Monte Lema. This study has extended the analysis conducted by [Gabella \(2018\)](#) with 19 more days, and by looking at the temporal variability of the signals, focusing on the observed variability of  $Z_{DR}$  for three specific events. [Borowska and Zrnic \(2012\)](#) list a number of influences on  $Z$  and  $Z_{DR}$  measurements from clutter, the nature of which can be further subdivided into environmental (env) or instrumental (instr):

- 1) changes in transmitted power (instr)
- 2) changes in receiver gains (instr)
- 3) antenna settling time (scan to scan changes in elevation) (instr)
- 4) scan to scan differences in azimuth pointing (instr)
- 5) variation of clutter reflection coefficient (env)
- 6) atmospheric refraction and beam propagation (env)
- 7) changes in attenuation due to precipitation (env)

The authors further note that if the variations of, and the correlation between the measurements in the H and V channels is high, there is probably a common cause affecting both channels such as a change in the transmitted power or some environmental influence ([Borowska and Zrnic, 2012](#)). While if the correlation between the two channels is low, they are not equally affected and thus variability is more likely to be caused by an instrumental issue in the receiving channel. As [Borowska and Zrnic \(2012\)](#) indicate, the radar should only be adjusted when it is certain that the discrepancies observed are caused by an instrumental issue. Table 2.3 shows that for most events in this study the correlation between the H and V channel is high ( $>0.6$ ) with the exception of the two January 2017 events for which it is significantly lower ( $>0.4$ ). For the March 2015 event on the other hand, correlations between the two channels are the highest of all six events. Changes in the transmitted power only affect  $Z$  measurements since the magic-T splits the power equally over the H and V channels. It can therefore be considered unlikely that the observed variability in  $Z_{DR}$  is related to any changes in the transmitted power. Since the analysis is based on only clear sky days and the tower is located relatively close to the radar, changes in attenuation can also be excluded. Due to the nature of the Cimetta tower, it is also unlikely that variability in the radar measurements may have been caused by variation in the clutter reflection coefficient. Even if the tower was wet, the resulting change in reflectivity should be negligible compared to the total reflectivity of the metallic tower and also similar in both channels. This leaves number 2,3 and 4 type issues from the instrumental influences and number 6 type issues from the environmental ones (notwithstanding the careful selection of events). To the aforementioned criteria this study also adds the high  $\rho_{HV}$  criterion on the grounds that if the target is not hit correctly over the full length of the 33 pulses, the data

should not be considered for hardware monitoring.

The high correlation between the H and V channels for the March 2015 and January 2018 events seems to indicate that the variability observed in  $Z_{DR}$  for this period is caused by a common factor influencing both channels (albeit the V channel more than the H channel). The high correlation between the V channel and the drops in  $\rho_{HV}$  (Table 2.3) further indicates that not hitting the Cimetta tower correctly seems to be the main factor causing these variations. Indeed, when data values for  $\rho_{HV} < 0.989$  are removed, the daily variances in the vertical channel (Table 2.1) are lowered to 2.7, 5.8, 2.6 and 4.7 for the March 2015 event, and to 1.3, 1.26, 4.0 and 1.6 for the January 2018 event. The fractions of variance explained by component for the unfiltered data in Fig. 2.8 show distinct peaks in the  $\rho_{HV}$  variability for the 48 hour and 24 hour components (0.15 and 0.05 respectively) suggesting an environmental issue rather than an instrumental one. The refractivity calculations do not indicate any abnormal propagation for this day (Table 2.2), so refractivities using stations at lower and higher altitudes were also calculated (Fig. 2.9). Interestingly, these show considerably more variation, and more specifically at the 48 hour timescale for the higher altitudes and the 24 hour timescales for the lower altitudes. The absolute value of the refractivity between Magadino (203 m asl) and Locarno-monti (367 m asl) is influenced by the very different nature of the two sites: Magadino is located close to the lake within the valley and subject to thermal inversions in wintertime while Locarno-monti is located on the mountain side and more exposed to the sun. The time series for the refractivity calculated between these two stations (blue lines) have been included as an indication of the relative stability of the lower part of the atmosphere between events, though it does not influence the trajectory of the radar beam which is well above these altitudes.

Finally, it can be noted that the  $CAL_{dr}$  signal also shows a small peak at the 24 hour component for the March 2015 event in Fig. 2.8 and that this  $CAL_{dr}$  signal variation co-fluctuates with the internal temperature variations (Fig. 2.7) and thus performs its normal corrective function of compensating for temperature variations inside the receiver box.

The significantly lower correlations between the H and V channels for the January 2017 events seem to indicate that the observed variability in  $Z_{DR}$  for these events was caused by an instrumental issue rather than an environmental one. Table 2.3 shows the high correlation between  $Z_V$  and outside temperature and Fig. 2.8 illustrates the distinct diurnal cycle observed in  $Z_{DR}$ ,  $Z_H$  and  $Z_V$ . While no correlations (Table 2.3) or diurnal cycles (Fig. 2.8) could be observed for  $\rho_{HV}$  and the atmosphere appears to have been relatively stable at all altitudes (Table 2.2 and Fig. 2.9). The diurnal cycle is also visible in the  $CAL_{dr}$  signal (differential noise source power on frontend) which was probably the result of the different behaviour of the low noise amplifiers (LNAs) of the H and V channels with respect to the temperature changes in the receiver box. The temperature change was  $\sim 2^\circ\text{C}$ , with an overall excursion of 0.15 dB for the H channel and 0.3 dB for the V channel. While the change in measured noise source power in the horizontal channel ( $\sim 0.07 \text{ dB/K}$ ) is still acceptable, the changes in the vertical channel are too important (Vollbracht et al., 2014).

## Chapter 2. Temporal monitoring of dual-polarisation weather radar

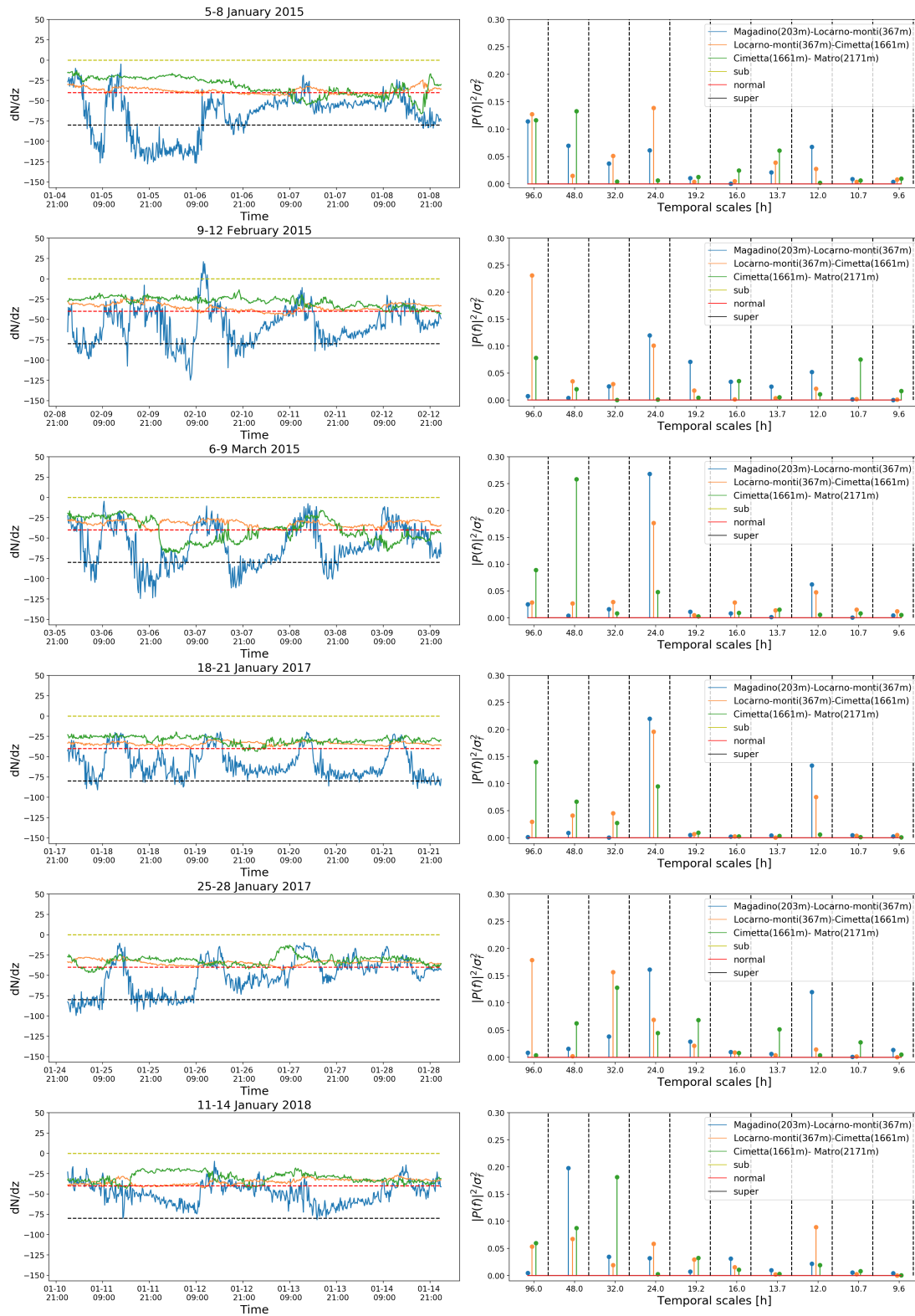


Figure 2.9 – Calculated refractivity time series (left) and their corresponding fraction of variance explained by component (right).



In order to operate on a broad dynamic range, the radar receiver system consists of four LNAs for the high gain (HI) and low gain (LOW) paths, and for both polarisations. Whereas the calibration (CAL) signals ( $\sim -90$  dBm) are amplified by the HI sensitivity channel, the strong Cimetta echo ( $\sim -30$  dBm) is necessarily amplified by the LOW sensitivity channel. Because in the January 2017 events both the returns from the Cimetta tower and the  $CAL_{dr}$  signal seem to be affected, the problem must have been situated in the receive path of the HI and the LOW sensitivity channels and most likely at the receivers. This finding is different from the findings by Borowska and Zrnic (2012), who also detected diurnal cycles in the  $Z_{DR}$  measurements of areas of ground clutter for the KOUN radar located in Oklahoma. In their case, the events coincided with high correlations between the H and V channels and were related to the diurnal cycle in the refractivity profile.

### 2.5.1 Possible correction of the diurnal cycle

The observations of the Cimetta tower can only be used for radar hardware monitoring if 1) it is certain that the center of the radar beam hit the tower correctly over the observation period (low correlation between  $Z_{DR}$  and  $\rho_{HV}$  and/or  $\rho_{HV} > 0.985$ ), and 2) the observed variability in the  $Z_{DR}$  signal is related to an instrumental issue (low correlation between  $Z_H$  and  $Z_V$ ). As such, situations with low correlations between  $Z_H$  and  $Z_V$ , high correlations between  $Z_{DR}$ ,  $Z_V$  (or  $Z_H$ ) and the  $CAL_{dr}$  signal, as well as a high 24 hour component ( $> 0.15$ ) in the FFT analysis for these three signals, can be considered as indicative of hardware issues. Since in the presented cases the  $CAL_{dr}$  signal is affected by the same phenomenon (high negative correlation between  $Z_{DR}$  and  $CAL_{dr}$  (Table 2.3)), it can be used to compensate for the variability in the  $Z_{DR}$  values, if it can be assumed that the  $CAL_{dr}$  signal should have been more or less constant over this period. Since the problem appears to have occurred in the vertical channel in the observed cases (as can be inferred from the high correlation between  $Z_V$  and  $Z_{DR}$ ) the  $CAL_{dr}$  signal needs to be added to the  $Z_{DR}$  signal for the compensation (and subtracted in case of a faulty horizontal channel). Finally, an amplification factor  $a$  for the  $CAL_{dr}$  signal is needed and calculated based on the ratio of the standard deviations of the  $Z_{DR}$  and  $CAL_{dr}$  signals:

$$Z_{DRc} = Z_{DR} + CAL_{dr} * a \quad (2.3)$$

where  $Z_{DR}$  and  $CAL_{dr}$  are in dB, and  $a$  is obtained by:

$$a = \frac{\sigma_{Z_{DR}}}{\sigma_{CAL_{dr}}} \quad (2.4)$$

The  $a$  values calculated for the 18-21 January and 25-28 January events were 26.5 and 29.45

respectively. This compensation takes care of most of the observed 24 and 12 hour cycles (Fig. 2.10) and reproduces a  $Z_{DR}$  signal of the Cimetta tower with variances of 0.5, 0.4, 0.4, and 0.5 for the four days of the first January 2017 event and 0.5, 0.6, 0.6 and 0.5 for the four days of the second January 2017 event which can be considered reasonable when compared with the values in Table 2.1.

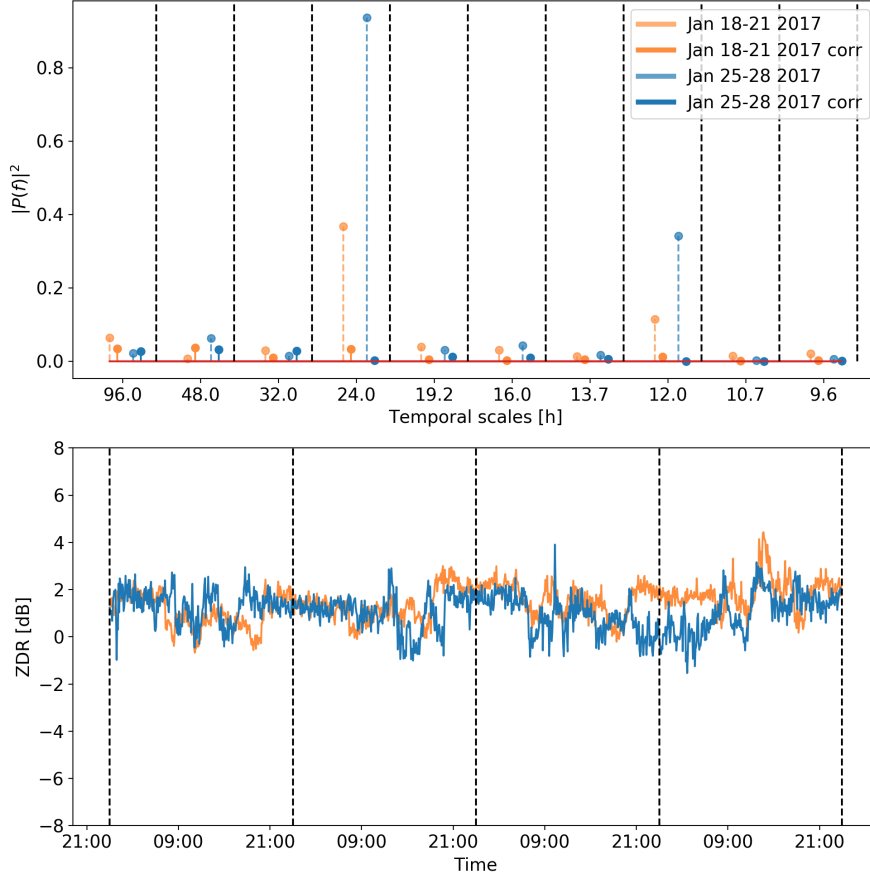


Figure 2.10 – Variance explained by each temporal lag for original and corrected  $Z_{DR}$  time series for the January 2017 events (top) and the time series for the corrected  $Z_{DR}$  (bottom).

## 2.6 Conclusions

The Cimetta tower represents a unique and stable bright scatterer which allows to perform temporal analysis of the polarimetric signals of the object and thus has the potential to be used for the temporal monitoring of the radar hardware. Based on observations of the Cimetta tower with the dual-polarisation Doppler C-band radar from the MeteoSwiss operational network for six events with four consecutive clear-sky days, this study seeks to identify periods within the day for which the variability of  $Z_{DR}$  is lower and analyses the potential of the tower for radar hardware monitoring. For the events analysed in this study it was found that the sub-daily variability in  $Z_{DR}$  measurements could be as low as  $\pm 0.9$  dB for some three hour

periods and as high as  $\pm 3$  dB for other three hour periods.

Three of the events were analysed in more detail because of the observed high temporal variability of the  $Z_{DR}$  measurement of the tower within the four day period. The FFT analysis of the time series further indicated a pronounced diurnal cycle in the  $Z_{DR}$  signal for two of these events. This diurnal cycle could be related to the noise source power on frontend calibration signal ( $CAL_{dr}$ ) and temperature. The low correlation between the H and V channels for these two events was considered indicative of an instrumental problem rather than an environmental one, while the high correlation between  $Z_{DR}$  and  $Z_V$  suggests that some problem in the receive path of the vertical channel may have caused the observed variability in  $Z_{DR}$ .

In the case of the event which did not display a distinct diurnal cycle in the FFT analysis of the  $Z_{DR}$  signal, the variability in the measurements could be related to variations in  $\rho_{HV}$  which was used in this study as an indicator for the quality of the measurement. The time series of refractivity just below the Cimetta tower showed variability at the 12 hour scale while the time series of refractivity in the air mass just above the Cimetta tower showed more variability at the 48 hour scale which was possibly related to more synoptic scale variability. It is possible that variations in the refractivity profile caused for the beam not to hit the Cimetta tower correctly over the course of this event. Because the horizontal and the vertical channels were equally affected, the correlation between these was high, although in absolute terms this resulted in lower measured values in the vertical channel causing an increase in  $Z_{DR}$ . Since this event was related to environmental factors rather than an instrumental problem, it was considered unfit for variance reduction using eq. 2.3. It is worth noting that this conclusion holds for the four day event as a whole. The spectral analysis presented in this study however, has shown that a daily time scale is probably optimal to emphasise hardware issues which are subject to diurnal variations (and are mainly linked to temperature variations inside the receiver box). This hypothesis has been verified and it was indeed found that on the first two days of the March 2015 event it is possible to successfully reduce the variance of  $Z_{DR}$  using the proposed eq. 2.3.

Hence it can be concluded that according to the results of this study, the Cimetta tower can be used successfully for radar system monitoring. It has been shown that there are cases for which an excess in variability of the  $Z_{DR}$  of the Cimetta tower can be related to an excessive compensation of the dual-polarisation LOW sensitivity channels. This important conclusion was reached by observing that in such cases the  $Z_{DR}$  signal of the tower is anomalously correlated with the online correction of the dual-polarisation HI sensitivity channel. If it can be assumed that the HI and LOW sensitivity channels are subject to a similar response to temperature (i.e. that these are correlated) then the differential echo from the Cimetta tower can be compensated based on the calibration (CAL) information related to the HI sensitivity channel (in the absence of such information for the LOW sensitivity channel). As demonstrated in this study, for the two events concerned the observed diurnal signal in  $Z_{DR}$  could be compensated using the information related to the calibration signals multiplied with an amplification factor. After this compensation, the daily variances of the  $Z_{DR}$  series were back to normal values ( $< 1 \text{ dB}^2$ ). As stated, the compensation method assumes that the

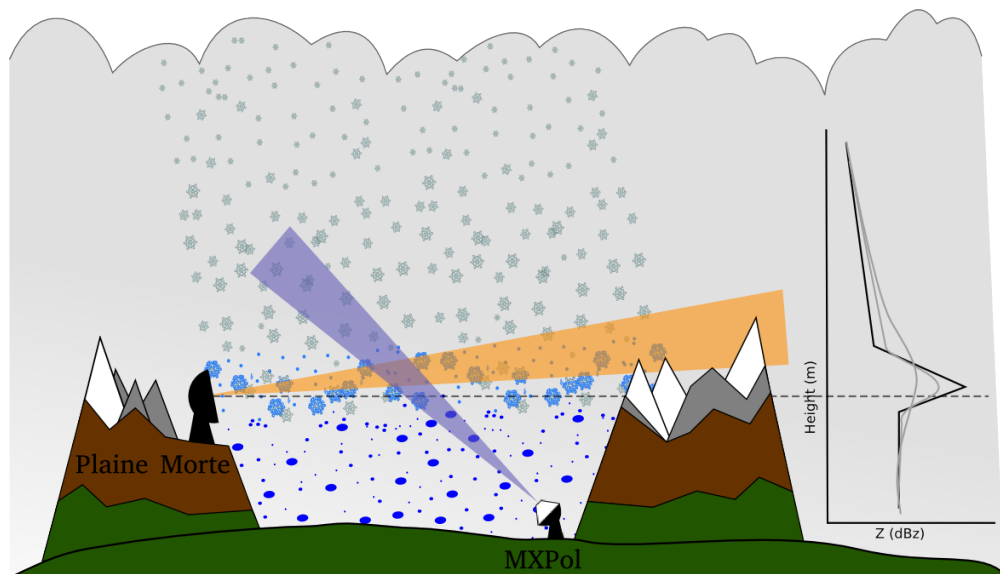
operational amplifier of the LOW sensitivity channel, which amplifies the Cimetta echo, is subject to the same diurnal (and temperature dependent) fluctuations as the HI sensitivity channel, which is calibrated using the noise source signal. However, this compensation was based on only eight days of measurements and should be tested with more events. Also, the results of this study were based on clear-sky days and further research may be conducted on the stability of the signal in days of continuous rain. Though a lack of four day events with non-interrupted rain would probably require such a study to be done on smaller temporal scales. The improved knowledge of the signature of the Cimetta tower does allow for further analysis of case studies of particular meteorological conditions such as the presence of a melting layer at the height of the Cimetta tower. Finally, this study has focused on signatures in  $Z_H$ ,  $Z_V$ ,  $Z_{DR}$  and to a lesser extent  $\rho_{HV}$ . Any further analysis could also include the temporal variability of the Cimetta tower signatures for other polarimetric variables.

### 3 Characterisation of the melting layer variability

This chapter has been adapted from the manuscript:

- van den Heuvel, F, M. Gabella, U. Germann and A. Berne, 2018: Characterisation of the melting layer variability in an Alpine valley based on polarimetric X-band radar scans. *Atmospheric Measurement Techniques*, **11** (9), 5181-5198, doi: 10.5194/amt-11-5181-2018.

It presents the characterisation and comparison of the spatio-temporal variability of the melting layer based the Fast Fourier Transform method applied to X-band radar data from a location on the Swiss plateau and a location in the Swiss Alps.



### 3.1 Summary

The melting layer designates the transition region from solid to liquid precipitation, and is a typical feature of the vertical structure of stratiform precipitation. As it is characterised by a well-known signature in polarimetric radar variables, it can be identified by automatic detection algorithms. Though often assumed to be uniform in space and time for applications such as vertical profile correction, the spatial variability of the melting layer remains poorly documented. The work presented in this chapter undertakes to characterise and quantify the spatial and temporal variability of the melting layer using a method based on the Fourier transform, which is applied to high resolution X-band polarimetric radar data from two measurement campaigns in Switzerland. It is first demonstrated that the proposed method can accurately and concisely describe the spatial variability of the melting layer and may therefore be used as a tool for comparison. The method is then used to characterise the melting layer variability in summer precipitation on the relatively flat Swiss plateau and in winter precipitation in a large inner Alpine valley (the Rhone valley in the Swiss Alps). Results indicate a higher contribution of smaller spatial scales to the total melting layer variability in the case of the Alpine environment. The same method is also applied on data from vertical scans in order to study the temporal variability of the melting layer. The variability in space and time is then compared to investigate the spatio-temporal coherence of the melting layer variability in the two study areas, which was found to be more consistent with the assumption of pure advection for the case of the plateau.

## 3.2 Introduction

Quantitative precipitation estimation (QPE) with radar in complex terrain such as the Alps, is complicated by many factors amongst which partial and total beam shielding by terrain, the influence of orography on the dynamics and microphysics of precipitation as well as the shallow depth of precipitation during cold seasons (Germann and Joss, 2004; Roe, 2005; Houze, 2012; Colle et al., 2013). In order to avoid the problem of shielding, radar measurements are often collected at higher elevations. The measurements made aloft are then usually extrapolated to the ground level to compensate for the lack of direct visibility with the radar (Joss and Pittini, 1991; Joss and Lee, 1995; Andrieu and Creutin, 1995; Vignal et al., 1999; Germann and Joss, 2002; Gray et al., 2002; Vignal et al., 2000; Zhang and Qi, 2010; Kirstetter et al., 2013). These extrapolated values are commonly corrected with the vertical profile of reflectivity (VPR) which represents the vertical change in the radar reflectivity measurement due to changes in size, phase and fallspeed of hydrometeors. Many VPR correction techniques used operationally, are based on mean VPRs extracted in well-visible regions of the radar (Koistinen, 1991; Joss and Lee, 1995; Germann and Joss, 2001, 2002). Other broad categories include climatological VPRs (Joss and Pittini, 1991; Joss and Lee, 1995; Gray et al., 2002), inverse VPRs (Andrieu and Creutin, 1995; Andrieu et al., 1995; Vignal et al., 1999; Vignal and Krajewski, 2001) and model derived VPRs (Mittermaier and Illingworth, 2003; Zhang and Qi, 2010; Kirstetter et al., 2013). A typical feature of VPRs in stratiform precipitation is the melting layer (ML) or bright band signature which designates a transition region from solid precipitation to liquid precipitation. It is characterised by a high horizontal reflectivity factor ( $Z_H$ ) due to the increase in effective dielectric constant as solid hydrometeors are coated by a thin layer of water, as well as a decrease in the copolar correlation coefficient ( $\rho_{HV}$ ) due to the presence of heterogeneous hydrometeor types (Battan, 1973; Zrnic et al., 1993; Fabry and Zawadzki, 1995; Brandes and Ikeda, 2004). Other polarimetric signatures in the melting layer include an increase in differential reflectivity ( $Z_{DR}$ ) which is usually smaller in the solid phase and higher in the liquid phase (Doviak and Zrnić, 2006) and large linear depolarisation ratio (LDR) values which may be related to broader distributions of canting angles due to increased spinning of the hydrometeors (Brandes and Ikeda, 2004). However, layers with single pristine crystals such as dendrites which are often present above the melting layer may cause a similar increase in  $Z_{DR}$  values (Matrosov et al., 2007), which is why many melting layer detection algorithms are based on  $Z_H$  and  $\rho_{HV}$  or LDR measurements.

Algorithms for QPE and VPR extraction often assume that the melting layer is spatially and temporally homogeneous, however as the VPR shape is dependent on microphysical processes such as riming and aggregation (Fabry and Zawadzki, 1995; Bell, 2000; Roe, 2005; Stoelinga et al., 2013), as well as on the vertical profiles of temperature and relative humidity (Matsuo and Sasyo, 1981; Stoelinga et al., 2013), this assumption may not necessarily hold for events with rain-snow transitions or in an orographic context (Boodoo et al., 2010; Campbell and Steenburgh, 2014). Multiple studies have shown that the melting layer can dip a few hundred metres downwards in the proximity of terrain (Lumb, 1983; Marwitz, 1983; Houze and Medina, 2005; Medina et al., 2005; Marigo et al., 2008; Stoelinga et al., 2013). And the melting layer

depth, for example, may vary with a factor of three depending on snowflake density (Matsuo and Sasyo, 1981; Stoelinga et al., 2013). Indeed, based on observational data, Wolfensberger et al. (2016) found significant dependencies between melting layer thickness and the presence of rimed particles above the melting layer. The authors related this to the longer distances travelled by rimed particles before complete melting due to the higher densities and fall velocities of these types of hydrometeors. Other important identified factors explaining the variability of the melting layer included the reflectivity gradient in the solid phase and copolar correlation coefficient values inside the melting layer (Wolfensberger et al., 2016).

As a result, individual VPRs at the near and far range can be highly variable with respect to the average VPR even in non-mountainous terrain (Jordan et al., 2000; Bellon et al., 2005; Berne et al., 2004). Though the variability of the melting layer and the freezing level height has been extensively studied at seasonal and large spatial (Harris et al., 2000; Thurai et al., 2003; Das et al., 2011; Rudolph and Friedrich, 2013) and temporal (Fabry and Zawadzki, 1995) scales, information on and quantification of the small scale spatial variability remains relatively sparse. Das et al. (2011) for example, studied the seasonal variability of the melting layer height at two different locations in India and found that the higher latitude location showed more monthly variability. For Mediterranean precipitation Berne et al. (2004) found that point-scale VPRs have a spatial representativeness which is limited to 6 km distances from the radar for 15 minutes integration times. Whereas Fabry et al. (1994b) reported a melting layer height change of 1500 metres within 3 hours in Montreal (Canada), Cluckie et al. (2000) found no more than 600 meters deviation in the melting layer height in the region of Middle Wallop (England) and this only in conditions with significant convection. However, none of these studies were conducted in an Alpine environment.

Mohyont and Delobbe (2008) first evaluated the ability of variograms to assess the spatial variability of the vertical profile of reflectivity in volumetric radar data in Belgium. They found that the variations of variograms of VPRs up to 200 km from the radar were caused by the non-uniform nature of the vertical structure. Variograms of reflectivity were also used by Germann and Joss (2001) to quantify the spatial variation of Alpine precipitation, which was found to be considerable for various types (convective and stratiform) of precipitation. Though the differences in reflectivity at all spatial ranges were lower for stratiform precipitation than for convective precipitation, the authors also found that the variation was weaker above the melting layer than below, indicating that the variation in reflectivity aloft can not fully explain the variation observed at ground levels. The vertical structure of radar-observed precipitation in Switzerland was also studied by Rudolph and Friedrich (2013). Based on characteristic seasonal patterns in the vertical structure, the authors could perform a seasonal classification of storms. The authors further related the vertical structure to dynamic and thermodynamic environmental parameters, showing that the radar-observed vertical structure of precipitation in the vicinity of Locarno, Switzerland, is correlated with synoptic patterns, integrated water vapour flux, atmospheric stability and the vertical profiles of temperature, moisture and wind (Rudolph and Friedrich, 2014). They could predict the vertical storm structure type with reasonable accuracy based on these parameters.

To increase the availability of radar information, MeteoSwiss has recently extended its weather



radar network with two polarimetric C-band radars at high altitude locations (~3000 m asl) in the Swiss Alps (Germann et al., 2015). This poses a new challenge of the applicability of existing vertical profile correction techniques to these high-altitude measurements but also provides new opportunities to use polarimetric radar variables for the improvement of QPE in these regions. Thus, information on, and the quantification of the spatial variability of the vertical structure of polarimetric radar variables in mountainous terrain is an important first step to the improvement of QPE and the estimation of its uncertainty in the Swiss Alps. Two measurement campaigns were conducted in very different though highly representative regions in Switzerland in order to study the structure and variability of precipitation. The use of mobile radars allowed to study the lower part of the troposphere in places of interest and with reduced visibility from the operational C-band radars. The melting layer detection algorithm designed by Wolfensberger et al. (2016) has been applied to the RHI (range-height indicator) scans from these campaigns to extract information on various characteristics of the melting layer. The study presented in this chapter seeks to quantify and compare the spatial variability of these melting layer characteristics at different spatial scales using a method based on the Fourier transform. The chapter is structured as follows; section 3.3 briefly presents the datasets and study areas, section 3.4 describes the pre-processing and how the Fourier transform method has been applied for the quantification of the spatial variability, section 3.5 presents an evaluation of the method as well as the results and discussion of the melting layer statistics from the two study areas and section 3.6 contains the main conclusions.

### 3.3 Dataset description

Most of the RHI scans used in this work were performed by the EPFL-LTE X-band Doppler dual polarization radar (MXPol) which was deployed in two distinct areas in Switzerland. First within the context of the PaRaDIso (Payerne RADAR and ISOtopes) campaign on the Swiss plateau in Payerne from the end of March to the beginning of July 2014 (Fig. 3.1), where it was co-located with another X-band radar (DX50). This location was of particular interest because it represents the climate conditions of a large, and most densely populated part of Switzerland and because of the presence of various other (disdrometers, radars, profilers, sounding) instruments in the area. MXPol was then deployed at the ground level (460 m asl) near Martigny in the main valley of the Swiss Alps for the 2016-2017 winter season. This area has the advantage of being both a very deep and long valley, thus providing both relatively good visibility with the mobile X-band radar and the possibility of studying precipitation characteristics in an Alpine valley.

#### 3.3.1 Data PaRaDIso campaign

The MXPol radar operated in Payerne from the 21<sup>st</sup> of March until the 14<sup>th</sup> of May within the context of the PaRaDIso campaign (hereafter Payerne campaign). It was offline for maintenance for one week between the 21<sup>st</sup> and the 28<sup>th</sup> of April, but no significant precipitation

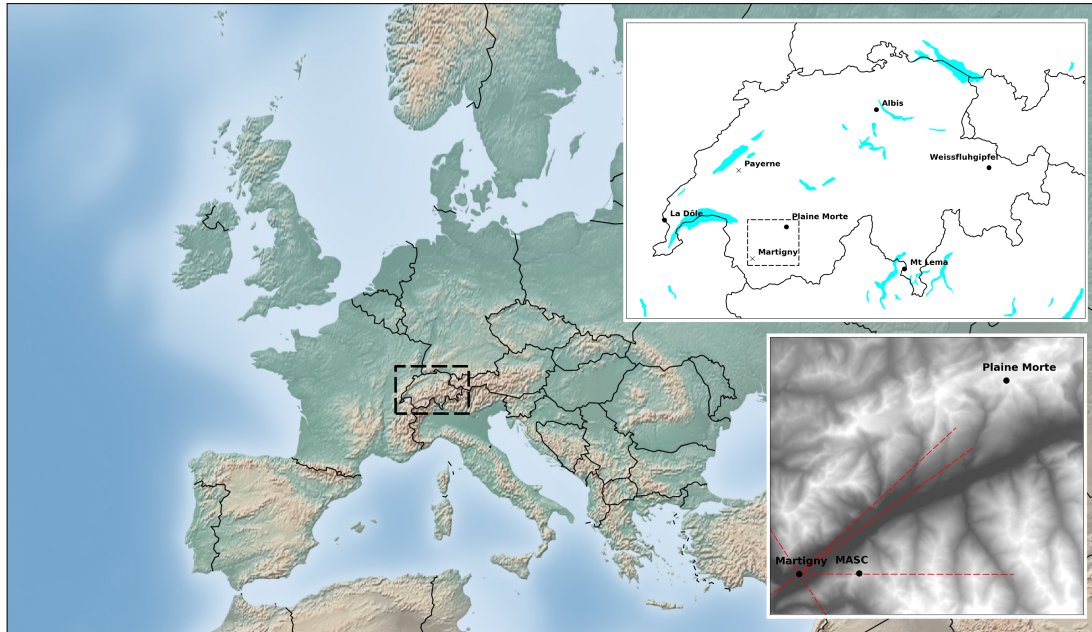


Figure 3.1 – Locations of the study areas (Payerne and Martigny) within Switzerland (top left panel) and the scan directions for the RHI scans during the Valais campaign (lower left panel).

events occurred during this period. Datasets from this campaign include RHI scans from the MXPOL radar as well as those from a similar X-band radar (DX50), located approximately 3.7 km away from MXPOL. The scanning strategy of the MXPOL radar during this campaign consisted of two RHIs (one in the direction of the DX50 radar) a Plan Position Indicator (PPI) scan at  $5^\circ$  elevation and a vertical PPI scan (rotating 360 degrees). The DX50 performed 3 RHIs (one in the direction of the MXPOL), 3 PPIs and also a vertically pointing scan. The scan strategies of both radars were repeated every 5 minutes. There are a total of 10 significant events for which data were recorded by both radars, representing over 170 hours of precipitation during which a total of 61.5 mm of rain was recorded in the nearby rain gauge. In addition to this, there were 4 medium intensity events, which represent over 29 hours of data and for which 5.4 mm of rain was recorded in the gauge. Data from both radars is also available for 5 low intensity events. All these events constituted the basis for the selection of the radar data for continuous and sufficiently long melting layers. About 460 RHI scans per azimuth were retained, each event containing at least 20 RHI scans. More information on this campaign can also be found in [Figueras i Ventura et al. \(2015\)](#).

The left most panel in Fig. 3.2 shows the average number of days with precipitation in Payerne for the period of March until May 2014 compared to the average conditions at that location for the same period. March 2014 for example, was relatively dry, whereas May was slightly wetter than usual. The middle panel shows the number of scans with a detected melting layer for each month; there is a clear over-representation for the month of May, mainly due to the fact that this is a rainier month both in terms of number of rainy days (left panel) and

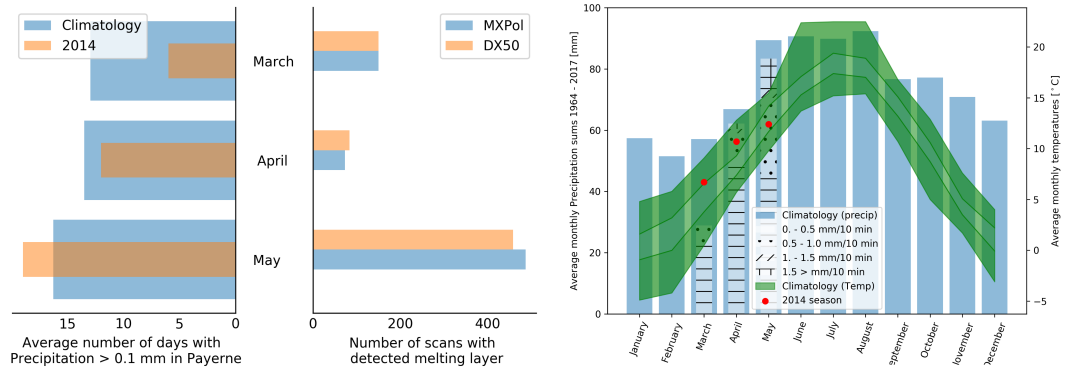


Figure 3.2 – Meteorological conditions in Payerne during the campaign compared to climatology; with the average number of days with precipitation for each month (left panel), the number of retained scans with a detected melting layer (middle panel) and a climatogram (right panel).

precipitation amounts (right panel). The climatogram in the right panel indicates average monthly precipitation sums (blue) and temperatures (green, with the quartiles in different shades) as compared with the measurements over the period of the Payerne campaign. The observed precipitation sums have been subdivided into the contributions of four classes of precipitation intensity. The total precipitation sums for the month of May did not exceed the climatological average, even though the number of wet days was higher. The average observed monthly temperatures are represented with red dots and are well within the climatological limits.

#### 3.3.2 Valais 2016-2017 campaign

The set-up of a mobile X-band radar near Martigny scanning under the operational MeteoSwiss C-band radar located at Plaine Morte (~40 km distance) was specifically intended to study precipitation in an orographic context and in wintertime, which are the conditions known to be most challenging to the quantitative estimation of precipitation in Switzerland (Germann and Joss, 2004; Koistinen et al., 2004; Germann et al., 2006; Montopoli et al., 2017). The MXPOL radar measured precipitation in the Valais from the 3<sup>rd</sup> of November 2016 to the 24<sup>th</sup> of May 2017. From this period, only the measurements between November 2016 and March 2017 are taken into account in order to restrict the analysis as much as possible to winter precipitation. The main characteristics of the MXPOL radar and the principal scanning strategy performed during the Valais campaign are given in Table 3.1. Because the radar was located in a deep valley, no non-vertical PPI scans were performed. The scan strategy changed once early during the campaign; before that, the radar performed 3 RHI scans in Dual Pulse Pair (DPP) mode in the main axis of the valley and one vertical PPI scan (rotating 360 degrees). The scanning strategy described in Table 3.1 turned for the remainder of the campaign and performed one RHI scan in the direction of the Plaine Morte (47°), one hemispheric RHI in the axis of the

### Chapter 3. Characterisation of the melting layer variability

main valley (54°), one RHI in Fast Fourier Transform (FFT) mode in the direction of Pierre Avoi mountain (90°), one RHI which made a cross section of the main valley (147°) and the vertical PPI scan in FFT mode. Both FFT mode scans were performed at 30 metres resolution and the DPP mode scans were performed with 75 metres resolution.

Radar parameters	
Wavelength	3.2 cm
Diameter	185 cm, <b>183 cm</b>
Range	35 km
3dB beamwidth	1.43° / <b>1.27°<sup>1</sup></b>
Peak power	7.50 kW per channel
Radial Resolution	30, <b>75 m</b>
Polarization	Simultaneous H-V
Scan strategy	
3 Range Height Indicator (RHI)	47, 90, 147° azimuth
1 emispheric RHI	90° azimuth
1 PPI for $Z_{DR}$ calibration	90° elevation
Scanning	Dual Pulse Pair mode FFT mode
Sequence duration	3 minutes 45 seconds
DPP mode	
PRI 1 (Pulse Repetition Interval)	800 $\mu$ sec
PRI 2	1000 $\mu$ sec
Group interval	1000 $\mu$ sec
Clutter averaging	9
Post averaging	3
Scan velocity	12 deg/s
FFT mode (PPI)	
PRI 1	700 $\mu$ sec
PRI 2	700 $\mu$ sec
Group interval	1200 $\mu$ sec
Clutter averaging	2
Post averaging	2
Scan velocity	16 deg/s

Table 3.1 – Characteristics of the MXPOL radar and scanning strategy during the Valais campaign.

<sup>1</sup>Due to a change in antenna for the Valais campaign

During the considered time period, a total of 403 hours of precipitation were recorded at the ground station in Martigny. Roughly 16 precipitation events could be identified on the basis of more or less continuous precipitation and similar synoptic conditions, representing a total of 324 hours of precipitation. These 16 events constituted the basis for the selection of the radar data for continuous and sufficiently long melting layers. Eventually, 1651 RHI scans per azimuth direction were retained, with each event containing at least 50 RHI scans.

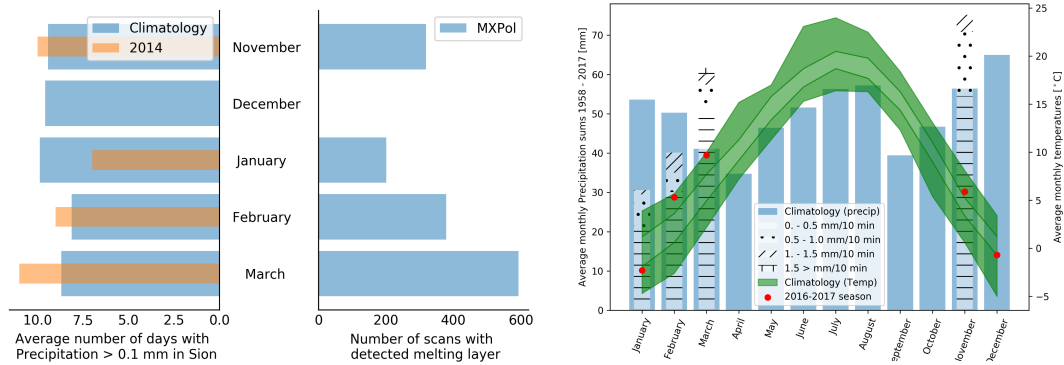


Figure 3.3 – Meteorological conditions in Sion (~20 km from MXPoI) during the campaign compared to climatology; with the average number of days with precipitation for each month (left panel), the number of retained scans with a detected melting layer (middle panel) and a climatogram (right panel).

The left panel in Fig. 3.3 shows the average number of days with precipitation in Sion (~20 km distance from MXPoI) compared with the observed number of days with precipitation at this location during the Valais campaign. While December and January were unusually dry, the other months were slightly wetter. The middle panel in Fig. 3.3 shows the number of scans with a detected melting layer for each month. The month of March is slightly over-represented due to the higher number of wet days and the higher precipitation sums for that month (right panel). The climatogram in the right panel indicates average monthly precipitation sums (blue) and temperatures (green, with the quartiles in different shades) as compared with the measurements over the period of the Valais campaign. The observed precipitation sums have been subdivided into the contributions of four classes of precipitation intensity. Precipitation sums for the months of May and November exceeded by far the climatological average, while February and March were relatively warm.

## 3.4 Methodology

### 3.4.1 Pre-processing

MXPoI applies an automatic Doppler filter on non-vertical scans, and all the radar data from the measurement campaigns have been further subjected to the same pre-processing routine

including a filtering of the data based on the signal-to-noise ratio threshold of 5 dB (10 dB for all phase based data)<sup>2</sup> and a copolar correlation coefficient ( $\rho_{hv}$ ) threshold of 0.6. Horizontal reflectivity ( $Z_H$ ) and differential reflectivity ( $Z_{DR}$ ) have been corrected for attenuation in rain using the constrained method by [Testud et al. \(2000\)](#). For the Payerne data a single  $Z_{DR}$  calibration coefficient, based on observations from previous campaigns, was applied. For the Valais campaign, due to increased variability of the  $Z_{DR}$  likely related to higher temperature variations on site, the calibration coefficient was updated more frequently and calculated based on data from the solid phase similar to the approach described by [Dixon et al. \(2017\)](#). The specific differential phase ( $K_{dp}$ ) was estimated from the total differential phase shift ( $\Psi_{dp}$ ) using the multistep method described by [Vulpiani et al. \(2012\)](#)<sup>3</sup>.

All the RHI scans from the 16 identified precipitation events were subjected to the melting layer detection algorithm developed by [Wolfensberger et al. \(2016\)](#), which was run using the ARM Radar Toolkit (Py-ART ([Helmus and Collis, 2016](#))). The algorithm uses the gradients of reflectivity and copolar correlation coefficient to detect the melting layer top and bottom; more information on the algorithm can be found in section 1.1.6 and [Wolfensberger et al. \(2016\)](#). Before applying the algorithm, the lowest elevation angles and the furthest gates of the scans were cut off to avoid contamination from ground clutter and mountains. In addition to this, the RHIs were subjected to a texture based clutter filter from the Py-ART toolbox. In order to limit the effects of beam broadening, the melting layer detection algorithm has been set to detect up to a maximum distance of 10 km from the radar, holes in the detected melting layer tops and bottoms were interpolated up to a maximum length of 1500 metres such as to obtain continuous, non interrupted data series. Otherwise, the default settings found to be optimal and described by [Wolfensberger et al. \(2016\)](#) were used, including interpolation of the RHI scans on a 25 m resolution Cartesian grid.

#### 3.4.2 Calculation of the power spectra of melting layer variables

From the output of the melting layer detection algorithm various variables have been extracted and calculated such as the heights of the top and bottom of the melting layer, the thickness or depth of the melting layer and the height of the reflectivity peak within the melting layer. Figure 3.4 shows the melting layer detection algorithm output with the corresponding extracted and derived variables for an idealised vertical profile.

Before subjecting the data to the Fourier transform, it was conditioned following the indications in [Stull \(1988\)](#). More specifically, the melting layer variables were first de-trended and then tapered to avoid red noise and leakage. The tapering was done with a bell taper for which

---

<sup>2</sup>for the Payerne data thresholds were 0 dB and 5 dB respectively

<sup>3</sup>Kalman-filtering was used for the Payerne data

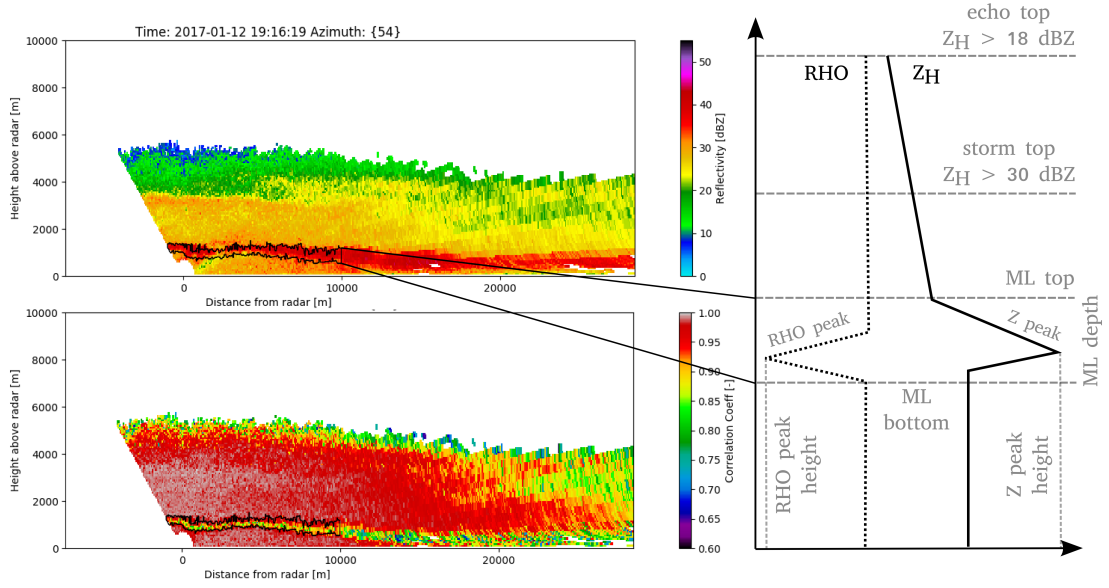


Figure 3.4 – Melting layer detection algorithm output superimposed on the reflectivity values (left upper panel) and on copolar correlation coefficient values (left lower panel) and the extracted and derived variables (right) indicated for an idealised vertical profile of reflectivity (VPR). The bending of the melting layer towards the ground is probably related to the trapping of cold air in the valley and the observed negative temperature gradient towards the East (in the direction of the scan).

the window weight is given by:

$$W(k) = \begin{cases} \sin^2(5\pi k/N) & \text{for } 0 \leq k \leq 0.1N \\ 1 & \text{elsewhere} \\ \sin^2(5\pi k/N) & \text{for } 0.9N \leq k \leq N \end{cases} \quad (3.1)$$

The variables were then subjected to a one dimensional Fast Fourier transform, such that for each melting layer variable  $A$  of length  $N$  the Fourier transform returned  $N$  coefficients of  $F_A(n_c)$  for every frequency  $n_c$ . Since only continuous melting layers were taken for the analysis, padding (filling the gaps with artificial data points) was not necessary. The fraction of variance explained by each component (or spatial scale)  $n_c$  was obtained by dividing the square of the norm of the complex Fourier transform by the total variance such as described in section 1.3.2. The effects of the conditioning of the data on the fractions of variance explained by component were monitored, and are briefly discussed in the following section.



### 3.5 Results

In the subsections below the extent to which the method can describe the individual melting layers, and how the fractions of variance explained by component are affected by the conditioning of the data are treated first. Then the results from the study areas on the Swiss plateau and in the Swiss Alps are compared, first based on general statistics of the melting layer and then based on the fractions of variance explained by component for the spatial analysis. Finally, the spatio-temporal coherence of the melting layer variability is assessed for the two sites.

#### 3.5.1 Evaluation of the method

In order to evaluate the extent to which the method can describe the melting layer variability and how many components are needed, the performance on individual melting layers was analysed. Figure 3.5 shows a selection of three melting layer tops from the Payerne campaign and two melting layers tops from the Valais campaign. The blue line is an artificial melting layer created by adding white noise to a linear trend. For the fraction of variance explained by component (panel b), only the first ten spatial frequencies are given (here represented in wavelength ( $1/f$ )) for representational purposes. The largest wavelengths (or spatial scales) correspond to distances of 20-15 km for melting layers which spanned almost the entire hemispheric scan. Panel c gives the cumulated sum of the fractions of variance explained by component from the 5000 m distance lag down to the Nyquist frequency (two times the resolution of the data). Since the spectra have not been folded back such as for the calculation of the discrete spectral density, the maximum fraction of explained variance is at 0.5. As a scaling break can be observed around the 500 m wavelength at minimum (indicated with a vertical dashed line) and since the most important differences between the melting layers are concentrated in the first few components, higher frequencies are considered to approach the noise related either to the melting layer detection algorithm or the resolution of the data. This is also close to the 750 m distance lag found by [Fabry et al. \(1994a\)](#) as the separation between variability due to measurement noise and weather. Moreover, as the panel c in Fig. 3.5 as well as calculations over the entire dataset indicate, at this distance the cumulated explained variance is 50% or more of the total variance in most of the melting layer tops.

The fractions of variance explained by component in panel b of Fig. 3.5 indicate how the individual melting layer tops can be distinguished; melting layer tops with less spatial variability (two of the three Payerne cases) have most of their variance explained by the first component and then equal amounts of variance explained by all of the subsequent components. This means that the corresponding melting layer tops either vary only at the largest spatial scale or at even larger scales not resolved by the obtained spatial frequencies. Melting layer tops which are spatially more variable have higher contributions to the total variance from smaller spatial scales, though here as well some leakage to the neighbouring frequencies is possible. It must be borne in mind that the larger spatial scales also have a higher associated uncertainty;



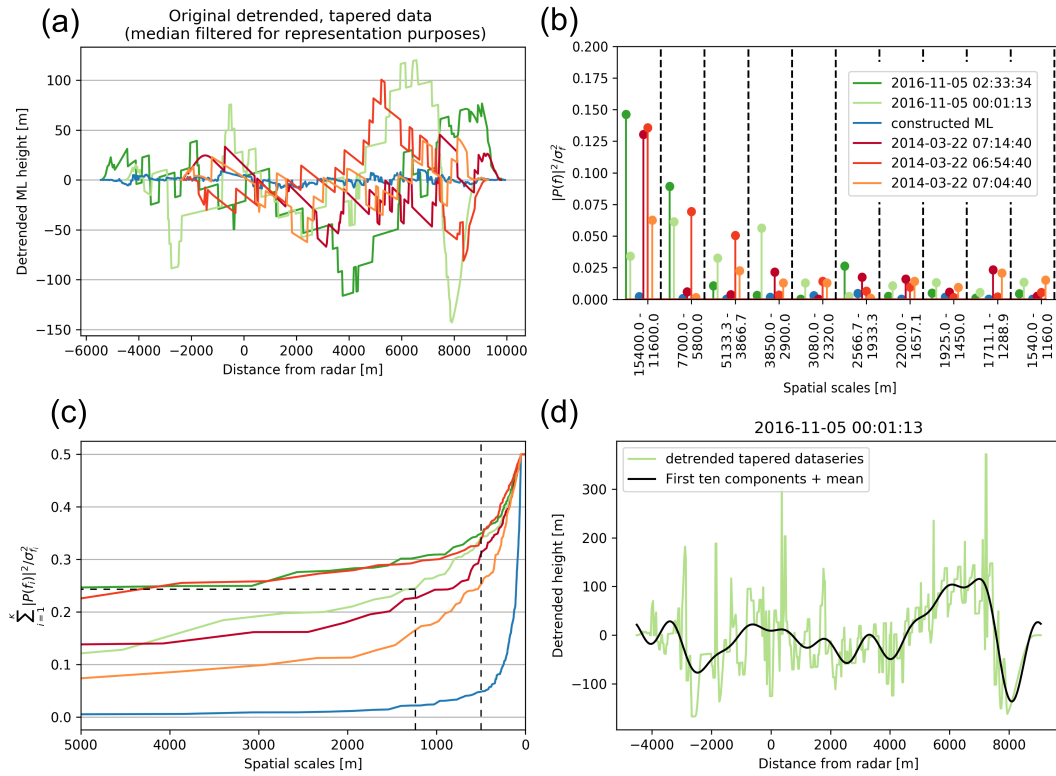


Figure 3.5 – Examples of observed melting layer tops (a), their corresponding fractions of variance explained by component (b), the cumulated fractions of variance explained (c) and one original melting layer with the reconstituted melting layer from the first ten components (d) from the Valais campaign (green), from the Payerne campaign (red) and for a constructed melting layer consisting of white noise with a drift (blue). The vertical dashed line in panel c indicates the location of the scaling break at wavelengths of 500 m and the horizontal dashed line indicates the location where 50% or more of the total variance is explained.

the first component for example, is based on only one realisation of the series. Therefore, as an example, the ability of the first ten components to reconstitute a single melting layer top is given in panel d in Fig. 3.5. These first ten components represent 50% of the total variance of this signal as indicated by the dashed lines in panel c of Fig. 3.5. The high spikes in the original melting layer (green line in panels a and d) are artefacts from the melting layer detection algorithm, and some beam effects can also be observed at further distances (around 7000 m distance from the radar). Nevertheless, the series are rather well reconstituted by the first ten components, giving credibility to the accuracy of the method. Furthermore, for the comparison of the data from the two campaigns the individual fractions of variance explained by component have been regrouped into box plots in order to account for the uncertainties at the larger spatial scales.

The effects of de-trending and tapering the data before performing the Fourier transform are shown for the melting layer tops of both campaigns in Fig. 3.6. De-trending reduces the amount of variance explained by the first component as it decreases the amount of red noise;

a linear trend acts as an infinite wavelength wave which manifests itself with noise at low frequencies. As mentioned, some of the melting layers may still have signals which are longer than 20 kilometres. The fact that these have been truncated at a set distance may also result in some additional red noise at the lower frequencies. However, the fact that the first component does not always explain most of the variance and the ability of the components to reconstitute the original melting layer indicates that red noise does not dominate the fractions of variance explained by component. With the exception of the echo tops, where slopes were slightly higher, the values of the trends that have been subtracted from the data were very similar for all datasets and were for the melting layer tops between -0.2 and 0.2; more than 50% of these remained within the -0.1 and 0.1 limits. Artefacts from the melting layer detection algorithm or noise from the original measurement may have some influence on the spectral slopes, which is why Fig. 3.6 also shows the effects of performing an additional median filtering of the melting layers before de-trending and tapering. It appears that the effect of median filtering on the fractions of variance explained by component is minor, and that de-trending and tapering of the melting layers is sufficient.

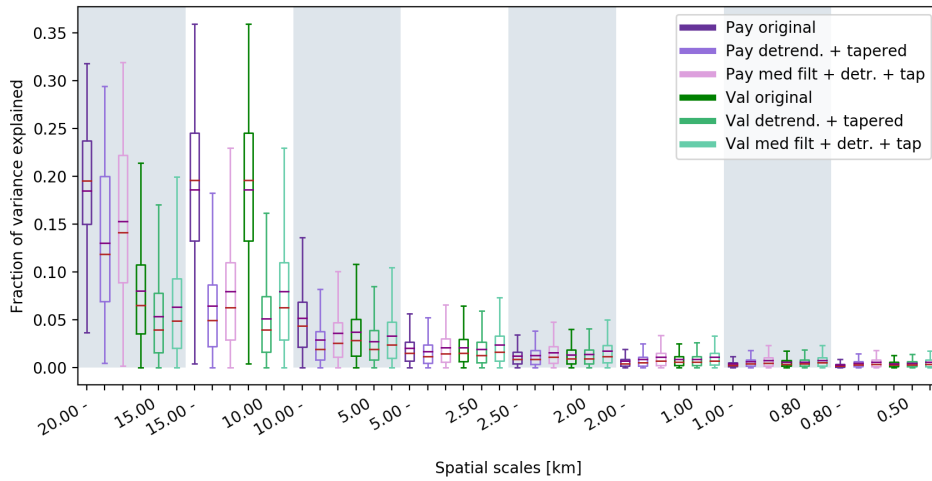


Figure 3.6 – Box plots illustrating the effects of median filtering, de-trending and tapering on the original melting layer tops for Payerne data (purple) and Valais data (green).

#### 3.5.2 Melting layer statistics

After running the melting layer detection algorithm on the retained scans, the outputs and derived variables as illustrated in Fig. 3.4 could be computed and descriptive statistics were calculated using the data over the entire scan. The resulting distributions of the melting layer tops, bottoms and depths, the highest reflectivity value and the lowest copolar correlation coefficient value within the melting layer and the height difference between these two values for all datasets are given in Fig. 3.7. A summary of these statistics including statistics of other polarimetric variables is given in Table 3.2. For comparability with the Fig. 3.7, the statistics in

Table 3.2 have been calculated on the log-transformed values. The comparison between DX50 values and MXPOL values in Payerne allows to evaluate to what extent the observed differences in the statistics may be attributed to the different radar systems. The melting layer tops and bottoms display a bimodal distribution in the Valais with an approximately 400 metre shift to the lower values due to the lower zero degrees isotherm in this region and season. The distributions of the heights of the melting layer tops and bottoms for the DX50 and MXPOL radars (for the same events) are comparable, with some second-order differences which could be explained by the different locations of the radar. Distributions of the melting layer depths are slightly skewed with a mode around 300 metres. The histograms of the melting layer tops, bottoms and depths show remarkable coherence in that the height distributions on the same location are very similar, that there is a shift towards the lower heights for the Valais data and that the melting layer depths remain the same between locations. The bimodality of the Valais data may be explained by the exceptional character of the 2016-2017 winter season with unseasonally high temperatures and perhaps the inclusion of data from early spring notwithstanding our careful selection of the data. Nevertheless, they are comparable to the results from Cluckie et al. (2000) in Salford England, where a bimodal distribution of melting layer heights with peaks at 650 metres and 1850 metres was found. The melting layer tops are also within the limits of the values found by Fabry et al. (1994b) in Montreal, which ranged between 200 and 3800 metres in spring and 0 and 3900 metres in winter. The observed melting layer depths are thicker than those observed by Cluckie et al. (2000) but comparable to the depth ranges reported by Fabry et al. (1994b). Similarly to the results in Cluckie et al. (2000) and Wolfensberger et al. (2016), melting layer thickness seems to be independent of season, climate or topography. It thus appears that at least in these datasets there is no indication of a relationship between melting layer thickness and melting layer height as suggested in Fabry et al. (1994b). Instead, as found by Fabry and Zawadzki (1995) it is more likely that there is some positive correlation between the melting layer thickness and the reflectivity of rain below the melting layer. Though distributions of the reflectivity values also seem very similar between the datasets, the Valais dataset is slightly shifted towards higher reflectivity values. This may be an effect of sampling (as the Payerne dataset is smaller) or due to the presence of higher precipitation intensities in the Valais dataset, but is also conform with the results from Wolfensberger et al. (2016) where a shift between the Payerne data and the Davos data (also a mountainous area) can be observed.

The distributions of the lowest values of the copolar correlation coefficient in the melting layer show much lower values for the DX50 than for the MXPOL radar; this is a known deviation for this radar, but does not affect the melting layer detection algorithm which is based on scaled gradients of  $\rho_{hv}$  and  $Z_H$  (Wolfensberger et al., 2016). The Valais dataset, like the Davos dataset in Wolfensberger et al. (2016) shows a larger presence of lower  $\rho_{hv}$  values within and above the melting layer but similar overall distributions. Lower  $\rho_{hv}$  values could be associated with enhanced riming and depositional growth above the melting layer. These processes result in the presence of a higher variety of particle types and can be expected to be the dominant growth mechanisms in a winter orographic environment and in situations with a low melting

### Chapter 3. Characterisation of the melting layer variability

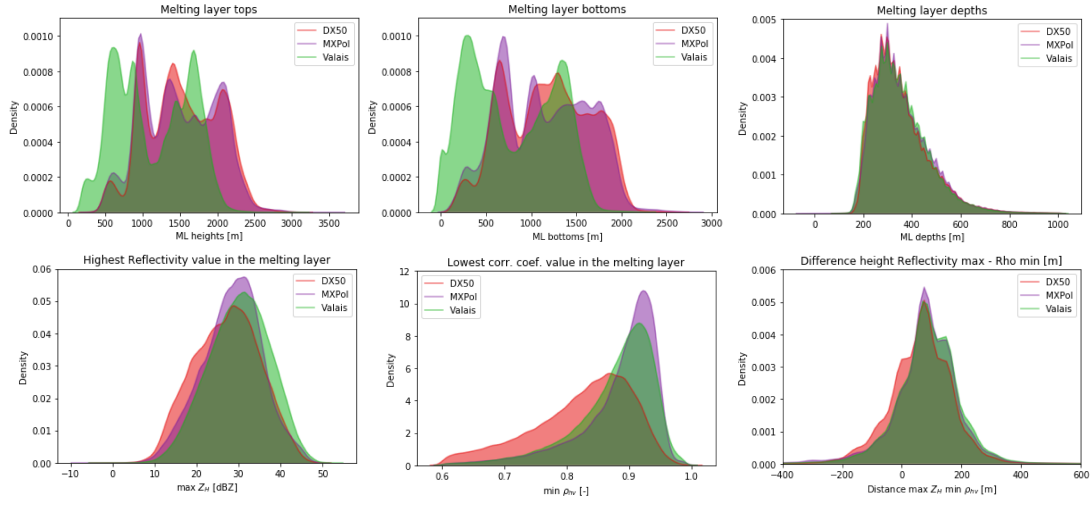


Figure 3.7 – Distributions of the characteristic melting layer variables.

layer (Colle and Zeng, 2004b,a; Colle et al., 2005a,b; Stoelinga et al., 2013; Schneebeli et al., 2013). Finally, the distance between the reflectivity maximum and the copolar correlation coefficient minimum shows a similar distribution across all datasets.

Variable	Statistic	DX50 (pay)	MXPoI (pay)	MXPoI (val)	Variable	Statistic	DX50 (pay)	MXPoI (pay)	MXPoI (val)
$Z_H$	Mean	22.19	23.14	22.84	$\rho_{hv}$	Mean	0.9125	0.9256	0.9301
	St.Dev	8.72	8.45	8.82		St.Dev	0.0727	0.0618	0.0595
	Q10	11.5	11.90	11.77		Q10	0.8111	0.8457	0.8506
	Q50	22.0	23.25	22.36		Q50	0.9331	0.9421	0.9465
	Q90	34.0	34.0	35.02		Q90	0.9803	0.9841	0.9874
$Z_{Hpeak}$	Mean	27.18	28.49	30.18	$\rho_{hvmin}$	Mean	0.8245	0.8854	0.8785
	St.Dev	7.73	7.11	7.23		St.Dev	0.0796	0.0633	0.0637
	Q10	16.5	18.83	20.44		Q10	0.7047	0.7971	0.7912
	Q50	27.5	28.95	30.47		Q50	0.8386	0.9039	0.8937
	Q90	37.5	37.15	39.49		Q90	0.9173	0.9437	0.9430
$Z_{DR}$	Mean	1.04	0.6	1.11	$K_{dp}$	Mean	0.06	0.098	0.099
	St.Dev	1.13	0.86	1.06		St.Dev	0.5	0.2	0.2
	Q10	-0.13	-0.3	0.05		Q10	-0.5	-0.13	-0.045
	Q50	0.90	0.47	0.92		Q50	0.05	0.09	0.03
	Q90	2.47	1.76	2.39		Q90	0.61	0.32	0.33

Table 3.2 – Statistics of the polarimetric variables related to the melting layer for the DX50 and MXPoI in the Payerne and Valais campaigns.

### 3.5.3 Spatial variability

The fractions of variance explained by component have been calculated for each separate RHI scan; which acts as a type of normalisation since each fraction represents the fraction of the total variability of the detected melting layer in that scan. Because the detected melting layers do not all have the same length, the fractions of variance explained by component have been regrouped into spatial scales based on their corresponding frequency values. As demonstrated in Eq. (1.20), the fractions of variance explained by component only give values of one side of the Fourier spectrum, in order for the fractions to sum to 1, the spectra should be folded (i.e. multiplied by 2). Figure 3.8 shows the box plots for the melting layer tops; both the DX50 and the MXPOL data from the Payerne campaign show higher fractions of variability explained for the first components (larger spatial scales) and an exponential decline of the fractions of variance explained towards the smaller spatial scales. The box plots for the Valais data on the other hand, display a much less pronounced decline in these fractions towards the smaller spatial scales indicating, on average, a higher relative importance of the variability at smaller spatial scales in the Alpine winter environment. Random sub-sampling of the Valais dataset indicated that these results are robust also for a smaller number (460) of scans. And analysis of the spatial variability at the event scale showed similar behaviour of the components across events. Moreover, the first ten components shown in the box plots explain, on average and for the folded spectra, 43%, 42% and 36% of the total variance for the DX50, MXPOL (Payerne) and MXPOL (Valais) data respectively. The difference between the Valais and Payerne datasets decreases when the first 20 components are considered to 54%, 53% and 50%.

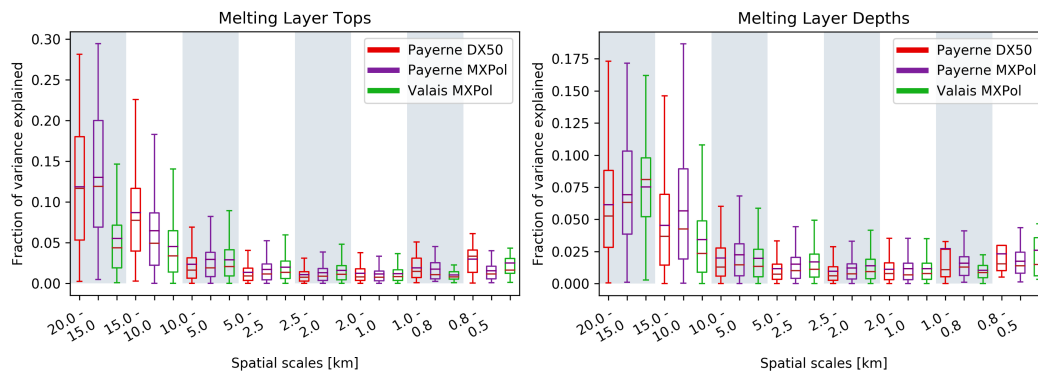


Figure 3.8 – Fractions of variance explained by component for the melting layer tops (left panel) and the melting layer depths (right panel) for the DX50 (red), MXPOL in Payerne (purple) and MXPOL in the Valais (green) (fractions of individual melting layers have been binned based on their corresponding frequency values).

The levelling out of the variability after the fifth component (the subsequent component corresponds to spatial scales of 2000 - 1500 metres) is comparable to the findings in [Wolfensberger et al. \(2016\)](#) who noted that the variogram of the melting layer tops reaches decorrelation distance at around 1500 metres. As can be seen in the box plots in Fig. 3.8 the intra campaign variability remains quite large. In fact, the first component is not always the most important

component in terms of fractions of variance explained. And subsequent components are more often the most important component in the Valais data than in the Payerne datasets (Fig. 3.9).

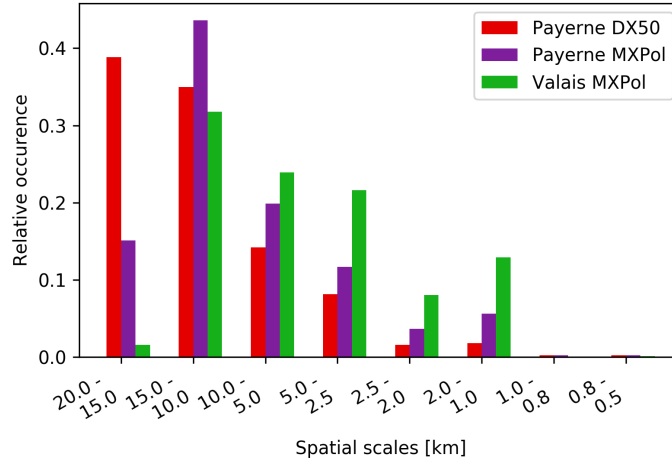


Figure 3.9 – Distribution of the binned spatial component with the highest fraction of explained variance per scan for the DX50 (red), MXPOL in Payerne (purple) and MXPOL in the Valais (green).

This intra campaign variability can be separated into inter event variability and intra event variability. Figure 3.10 shows the parallel coordinates plots of the fractions of variance explained for the binned spatial scales (on the vertical parallel y-axes) for each individual RHI scan (coloured lines) of the separate events (grouped on the first vertical y-axis). A single event has been highlighted on the first vertical y-axis such that the variability of the values for the components in a single event (intra-event variability) becomes evident. On the third y-axis from the left, 10% of the explained variability of the second component has also been highlighted to illustrate the inter-event variability. The inter event variability of the fractions of variance explained by component appears to be larger for the Payerne data, as is illustrated by the many different colours in the selected 10% of the second component. This may well be due to a sampling effect as the dataset is much smaller and thus the weight of the individual scans is much more important. For the Valais data, the intra-event variability and the inter event variability appear more similar. The high intra-event variability in the fractions of variance explained by component suggests that the melting layer variability is not necessarily consistent for similar synoptic conditions. Notwithstanding this inter and intra event variability, the box plots of the fractions of variance explained by component at the event scale indicate a typical behaviour namely that the variability in space at the larger scales is always smaller in the Valais data, and in the Payerne data most of the total variance is always explained by the first component (i.e. the larger scales). The coordinate plots also show that the larger spatial scales (20-15 km) are equally well represented in both campaigns even though for the Valais campaign these only occurred in the first two events because of a change in scan strategy which hindered the visibility in the 0-23 degrees elevations afterwards.

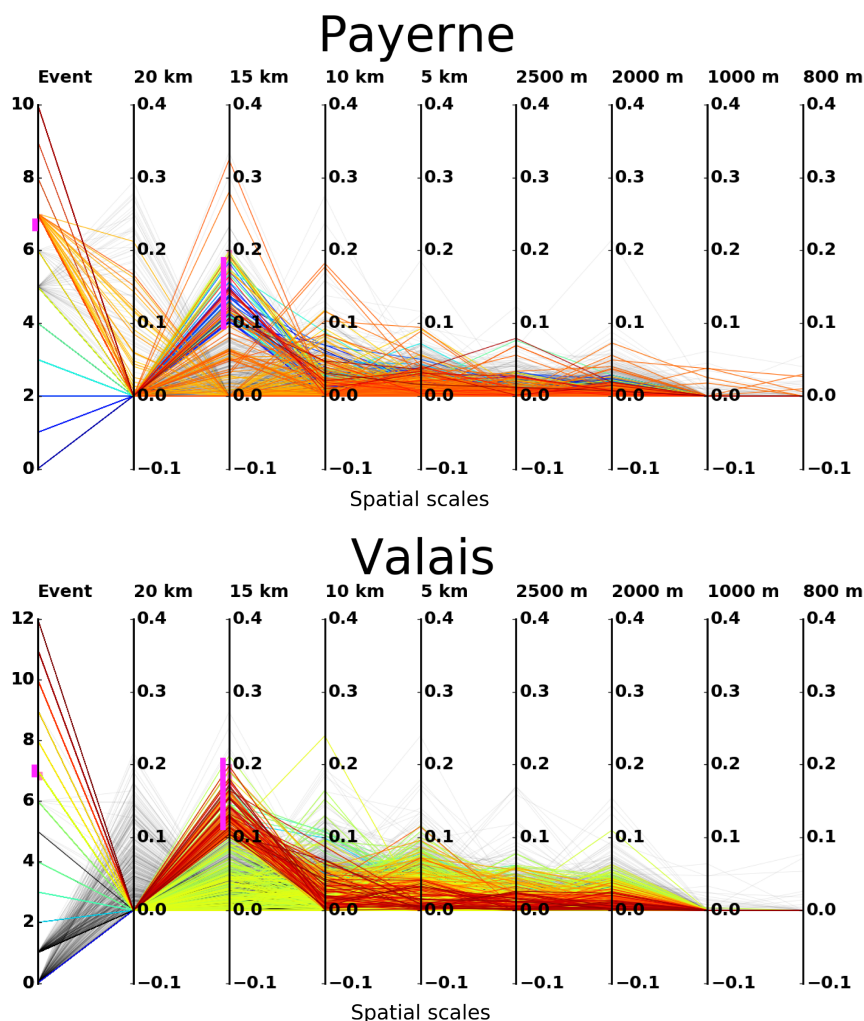


Figure 3.10 – Parallel coordinates plots illustrating the intra and inter event variability of the fractions of variance explained by component of the melting layer tops, for the MXPOL in Payerne (top panel) and the MXPOL in the Valais (bottom panel); highlighted for a single event (number 7, indicated in pink on the first y-axis, and event lines are orange for Payerne and yellow for Valais) and highlighted for 10% of the explained variance for the second component (indicated in pink on the third y-axis).

The fractions of variance explained by the melting layer bottoms are more similar for both campaigns and showed higher values for the larger spatial scales in the Valais data than for the melting layer tops. This has been commented on in [Wolfensberger et al. \(2016\)](#) and is thought to be related to the fact that the detected melting layer bottom is smoother than the tops because the detection of the melting layer top is solely dependent on reflectivity which is more influenced by large hydrometeors, while the detection of the bottom depends on both reflectivity and the copolar cross-correlation coefficient. The box plots of the fractions of variance explained by component of the melting layer depths (thickness) show very little spatial variability and indicate the opposite behaviour as compared to the melting layer tops.



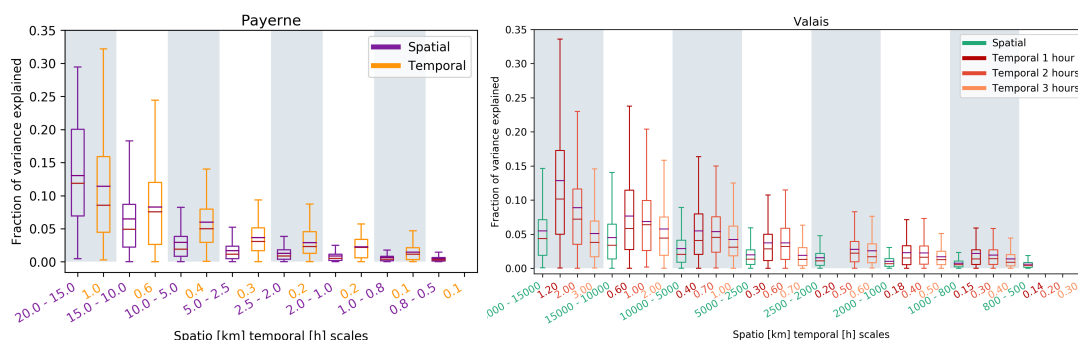
For the Valais data, the larger spatial scales explain most of the variance, whereas for the Payerne data, the 20 - 15 km and the 15-10 km (15-10 km and 10-5 km for the  $\rho_{hv}$  minimum) lags are equally important. This may be related to the presence of more convective pockets in the Payerne dataset. Overall, the statistics are more similar for the two locations (and for the three radars) for the melting layer depths than for the melting layer tops, indicating that the variability in the melting layer depth is more consistent over flat areas and complex topography.

#### 3.5.4 Spatio-temporal coherence of the melting layer variability

For the analysis of the temporal variability, a number of events have been selected based on their duration (at least 5 hours of quasi continuous precipitation). As such, from the Payerne campaign 4 events with a total duration of 26.5 hours were selected, and from the Valais campaign 4 events with a total duration of 94 hours were selected. In order to increase the temporal resolution, the data extracted at vertical incidence from the RHI scans were added to the vertical PPI scans, creating blended RHI/PPI time series of at least 1.66 minute resolution. The melting layer detection algorithm was then applied to the temporal series which were de-trended over the duration of the entire event, thus preserving the within-event variability. The removed absolute trends varied depending on the length of the time series; the highest removed trend was 112 metres/hour for the shortest event and the lowest removed trend was 3 metres/hour for the longest event. The 112 metres/hour trend may seem large, but has been related to the passage of a small occluded front, and remains lower than the observed height change in a time series from [Fabry et al. \(1994b\)](#), who recorded a change of 1.5 km in 3 hours. From the de-trended data, periods of one hour were selected with a sliding window of 12 minutes. The lengths of the sub selected time series were roughly the same, but they have nevertheless been re-binned into set time lags. Figure 3.11 shows the resulting box plots of the fractions of variance explained by component for both the spatial components (in purple and green) and the temporal components (in orange and red) for the two campaigns. Figure 3.11 suggests that in Payerne, the spatial and temporal variabilities are very similar at the investigated scales. The slightly lower values for the temporal data may be attributed to the fact that it was more difficult to ascertain continuous precipitation in the temporal data and discontinuities have the effect of diminishing the spectral slope and as such also the fractions of variance explained for the larger scale components ([De Montera et al., 2009](#); [Verrier et al., 2011](#); [Rysman et al., 2013](#)). Still, variability observed at spatial scales of 20 to 15 kilometres is very similar to the variability observed at the 1 hour scale. Indeed, considering that the average wind speed measured by a meteorological station on site during the time periods of the selected events was  $11.0 \text{ km/h} \pm 3.7 \text{ km/h}$ , it may well be that the air mass scanned by the RHI scans up to 10 km from the radar was very similar to the air mass scanned above the radar within the hour. This is also comparable to the findings of [Rysman et al. \(2013\)](#), who found similar spectral slopes for the 20-45 minutes temporal range and the 7-20 km spatial range for summer months in the Mediterranean region. The authors related the spectral slope at these temporal ranges to the expected value for velocity within a turbulent



flow, indicating that at these scales rain is driven by turbulence. Whereas in the Mediterranean case the spectral slope for the 20-45 minute time lag was the same for all months (except during fall), the Payerne and Valais datasets show more discrepancies. For the Valais data at the one hour scale (red box plots in the right panel of Fig. 3.11), the larger time lags seem to be responsible for about twice as much of the temporal variability than the larger spatial scales. On the one hand, this could be consistent with the influence of the more variable small-scale topography in the Valais affecting the RHI scans. On the other hand, the wind speeds during the Valais events were also much more variable with an average of 4.2 km/h and a standard deviation of 5.3 km/h. The slower wind speeds and longer time series of the Valais events justifies an analysis at longer temporal scales. The right panel in Fig. 3.11 also shows the box plots for the temporal components for spatial scales up to 2 (dark orange) and three (orange) hours. Though some differences with the spatial components can still be observed, the temporal components are much more similar at the 2 hourly and 3 hourly scales. The difficulty of finding spatio-temporal coherence in the Valais data may also partly be explained by the wintertime results from [Rysman et al. \(2013\)](#) where spectral slopes showed that a unique scaling regime characterised the rainfall scaling behaviour from 3 to 70 km scales (and from 5 minute to 3 hourly scales), meaning that the fractions of variance explained by component can be expected to be very similar at these scales.



Chapter 3. Characterisation of the melting layer variability

transect of the RHI in the Valais, it is difficult to link these to the melting layer variability due to the many other factors (i.e. wind speeds and hydrometeor fall velocities) that may play a role.

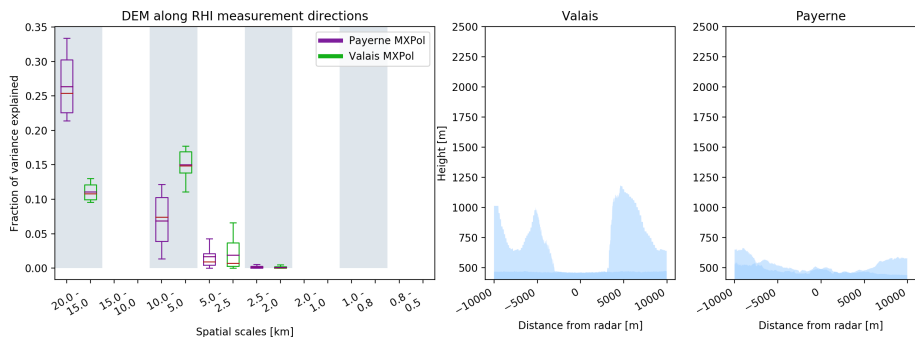


Figure 3.12 – Box plots of the fractions of variance explained by component (binned) for the ten transects extracted from the DEM data in the direction of the RHI scans ( $\pm 5$  degrees azimuth) with in the right hand panels the first and last transect of the DEM in clockwise direction (measurement direction  $-5^\circ$  and measurement direction  $+5^\circ$  azimuth).

### 3.6 Conclusions

This chapter presented the characterisation and quantification of the spatial variability of the melting layer at different scales using a method based on the Fourier transform. It is demonstrated that the proposed method is able to accurately describe the variability in individual melting layers and that it constitutes a useful basis for comparison of the variability of the observed melting layer at different spatial scales in different regions or from different data sources. The method has been applied to data from measurement campaigns conducted in two very different though highly representative regions in Switzerland, namely on the relatively flat Swiss plateau during summer and in a large inner Alpine valley in the Swiss Alps in winter. The descriptive global statistics of the melting layer tops, bottoms and depths have been found to display remarkable coherence; with a seasonal shift in the distributions of the heights while distributions of the melting layer thickness remained the same independent of season or location. The values and distributions found in this study are consistent with those found in previous studies at other locations. However, the performed Fourier analysis of the spatial variability of the melting layer tops indicated a higher importance of variability at smaller spatial scales in the case of the Alpine environment, possibly related to the influence of the small-scale topography. The investigation of the variability of the topography in the dominant wind directions of the considered regions also suggested a larger importance of the small scales in the Valais region, but will require further research in order to establish a more direct link. According to the results of this study, there is little difference in the spatial variability of the melting layer thickness in the two regions suggesting that it is less affected by topography. Finally, the method was also applied to time series of the melting layer height of sufficiently long events in order to study the spatio-temporal coherence of the melting layer variability. For the Swiss plateau, the variability at the 1 hourly temporal scale corresponded well with the spatial variability at the 15-20 km scales, which is also consistent with results from other studies. The average wind speeds during these events varied little around 11 km/h suggesting that the hypothesis of pure advection is quite valid for this region and during spring time. Due to more variable wind speeds and directions, the presence of small-scale topography and the possible scale invariance of wintertime precipitation conditions, it was more difficult to relate the scales of spatial and temporal variability in the Alpine environment. If any, it is possible that the spatio-temporal coherence in this region occurs at larger scales than could be measured with an X-band radar.

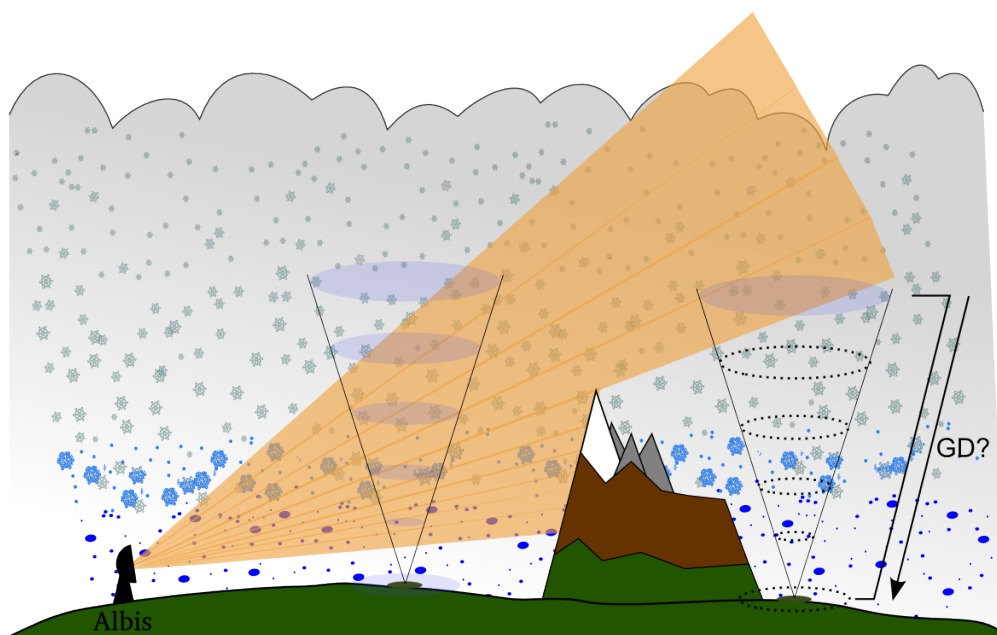
It should be noted that the results of this study are restricted to very specific locations and conditions as well as to temporal scales of up to 3 hours and spatial scales of 20 km and less. Nevertheless, the presented results indicate that for some regions the descriptive global statistics of the melting layer height may hide some important spatial variability of the melting layer. Current operational vertical profile correction techniques still assume spatial homogeneity of the melting layer, and the results of this study further indicate the necessity of a correction technique which takes this variability into account, and give an indication of the relative contributions of various scales.

## 4 Learning about the vertical structure of radar reflectivity

This chapter has been adapted from the manuscript:

- van den Heuvel, F, L. Foresti, M. Gabella, U. Germann and A. Berne, 2019: Learning about the vertical structure of radar reflectivity using hydrometeor classes and neural networks - going beyond an average profile in the Swiss Alps. *Atmospheric Measurement Techniques*, in preparation.

It presents a more localised vertical profile correction technique using reflectivity data and hydrometeor proportions extracted within vertical cones as inputs for artificial neural networks.



## 4.1 Summary

The use of radar for precipitation measurement in mountainous regions is complicated by many factors, especially beam shielding by terrain features, which, for example, reduces the visibility of the shallow precipitation systems during the cold season. When extrapolating the radar measurements aloft for quantitative precipitation estimation (QPE) at the ground, these must be corrected for the vertical change of the radar echo caused by the growth and transformation of precipitation. Building on the availability of polarimetric data and a hydrometeor classification algorithm, this work applies machine learning methods to study the vertical structure of precipitation in Switzerland and proposes a more localised vertical profile correction. It first establishes the ground work for the use of machine learning methods in this context: from volumetric data of 30 precipitation events vertical cones with 500 m vertical resolution are extracted. It is shown that these cones can well represent the vertical structure of different types (stratiform, convective, snowfall) of precipitation events. The reflectivity data and the hydrometeor proportions from the extracted cones constitutes the input for the training of artificial neural networks (ANN), which are required to predict the vertical change in reflectivity. Lower height levels are gradually removed in order to test the ANN's ability to extrapolate the radar measurements to the ground level. It is found that ANN models using the information on hydrometeor proportions can predict from altitudes between 500 and 1000 metres higher than the ANN based on only reflectivity data. In comparison with more traditional vertical profile correction techniques the ANNs show less prediction errors made from all height levels up to 4000 m a.s.l., above which the ANNs lose predictive skill and the performance levels off to a constant value.

### 4.2 Introduction

Precipitation constitutes a key meteorological variable for ecosystems and societies; both as a primary input for freshwater resources and (in deficit or excess) as a potential threat to infrastructure and human lives. Mountainous regions such as the Alps, through their impact on the flow and stability of air masses, influence the spatial distribution of precipitation (Frei and Schär, 1998; Roe, 2005; Colle et al., 2013) as well as precipitation growth processes and microphysics (Yuter and Houze, 2003; Colle et al., 2005b; Stoelinga et al., 2013).

Nevertheless, measuring precipitation in the Alps remains a challenge: while ground rain-gauge networks are typically affected by poorer spatial representativity, wind-induced errors (especially in the case of solid precipitation (Nitu et al., 2018)) and practical difficulties related to access and maintenance, the quantitative precipitation estimates (QPE) by radar are also limited by many factors (Germann and Joss, 2002). While the errors induced by ground clutter, hardware calibration and - to a certain extent - attenuation (Germann, 2000; Germann et al., 2006, 2015; Gabella et al., 2016), can be satisfactorily dealt with within the Swiss polarimetric C-band radar network, reduced visibility and the correction for the changes in the vertical profile of precipitation remain important challenges (Germann and Joss, 2002). Visibility reduction due to partial and total beam shielding by mountainous terrain is partly overcome by the higher elevation locations of the Swiss radars (between ~900 and ~3000 m a.s.l.) but this also exacerbates the effects of overshooting due to earth curvature. As a result, the radars cannot measure in the lowest layers of the atmosphere. For areas with reduced visibility it is common practice to use radar measurements from aloft to estimate precipitation quantities at the ground level. These measurements must first be corrected for the vertical profile of precipitation (VPP) which includes changes in size, phase and fall speed of hydrometeors. And because vertical profile corrections are typically based on and applied to the radar reflectivity measurements, this technique is called the vertical profile of reflectivity (VPR) correction. Existing operational VPR correction schemes often assume spatio-temporal homogeneity and rely heavily on the reflectivity measurements (section 1.2). Due to the spatial variability of precipitation microphysics, of temperature and humidity profiles as well as the growth and decay processes (Matsuo and Sasyo, 1981; Fabry and Zawadzki, 1995; Bell, 2000; Roe, 2005; Stoelinga et al., 2013) VPP and thus VPR profiles may be expected to vary considerably in space and time, especially in an orographic context (Boodoo et al., 2010; Campbell and Steenburgh, 2014).

The aim of this study is to propose a more local vertical profile correction technique using machine learning algorithms (MLA) and information on hydrometeor proportions to predict the vertical change in reflectivity or growth and decay (GD). To the best of our knowledge, MLA have not been used for the investigation of the vertical structure of precipitation and therefore an important part of the presented work is to establish the foundation for the use of MLA in this context. Artificial Neural Networks (ANN) are a type of MLA which are well-established in the geo- and environmental sciences and are also used for this study. The selection of events, preparation and extraction of the data will be addressed in Sect. 4.3,

while more details on the set up and the training of the ANN are given in Sect. 4.4. The main objective of this work will be addressed through the following steps: firstly, the ANN is used to learn about the contribution of hydrometeors to potentially improve QPE in Switzerland, then information at lower height levels is gradually removed in order to test the ANN's ability to extrapolate the radar measurements to the ground level. And finally, the ANN predictions will be evaluated and compared with the current operational VPR correction technique. Sect. 4.5 presents the exploratory data analysis, the results of the machine learning predictions and their verification, while Sect. 4.6 puts the contribution of this study into a broader perspective.

### 4.3 The vertical cone database

The data used in this study are extracted from high-resolution volumetric radar data acquired by the Albis radar located at ~900 m a.s.l on the Swiss plateau. The radar has good visibility from the South West to the East and some regions with ground clutter in the South due to the presence of the Bernese Alps (Fig. 4.1). Of the five Swiss radars, the Albis radar is situated at the lowest altitude and can thus provide measurements of the lowest parts of the atmosphere. Moreover, the Albis radar has been stably producing high quality data over the past years, allowing the ANN to be trained with the best available quality data.

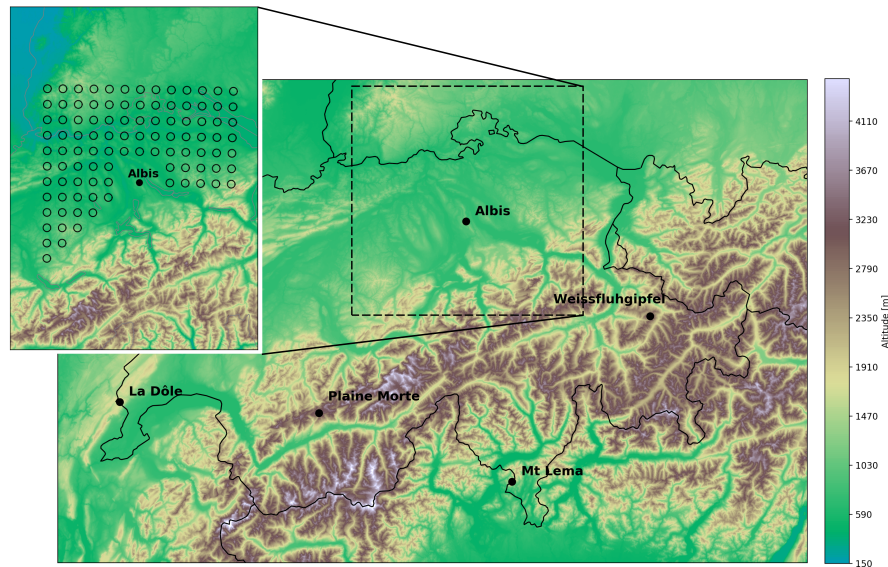


Figure 4.1 – Location of the Albis radar within Switzerland and the regular grid for the vertical cone extraction.

#### 4.3.1 Radar data pre-processing

Like the other radars in the Swiss operational network, the Albis radar performs 20 plan position indicator (PPI) scans within five minutes at elevations ranging from  $-0.2^\circ$  to  $40^\circ$  (Germann et al., 2015) with an interleaved sweep pattern. For this study the high resolution

data with a range resolution of 83.33 m was used.

The processing of the radar data was performed using the Python-based open source software Pyrad/Py-ART (Helmus and Collis, 2016; Figueras i Ventura et al., 2017). The signal-to-noise ratio (SNR) of the horizontal channel was calculated based on the estimated receiver noise at high-elevation angles ( $40^\circ$  or  $35^\circ$ ). Subsequently the SNR, and the ratio of the receiver noise in the horizontal and vertical channels were used to minimise the effect of noise on the co-polar correlation coefficient ( $\rho_{HV}$ ) (Gourley et al., 2006). Clutter was identified and removed using a filter based on textures of reflectivity factor at horizontal polarisation ( $Z_H$ ), differential reflectivity ( $Z_{DR}$ ), copolar cross correlation coefficient ( $\rho_{HV}$ ), total differential phase shift ( $\psi_{dp}$ ) and the value of  $\rho_{HV}$ . Gates with an SNR below the threshold of 10 dB were filtered out before performing a double window moving median filter on  $\psi_{dp}$ . The filtered differential phase ( $\phi_{dp}$ ) was then used to estimate the specific attenuation ( $A_h$ ) using the ZPHI algorithm (Testud et al., 2000) in order to correct for attenuation induced by precipitation, and to derive the specific differential phase shift on propagation ( $K_{dp}$ ) using the method described by Vulpiani et al. (2012).

The filtered and corrected polarimetric variables were then used as input for the semi-supervised hydrometeor classification developed by Besic et al. (2016, 2018). This method uses  $Z_H$  (-10 - 60 dBZ, influenced by particle concentration, size and density),  $Z_{DR}$  (-1.5 - 5 dB, influenced by particle shape, orientation and density),  $K_{dp}$  (-0.5 - 5 deg km<sup>-1</sup>, influenced by particle concentration and shape),  $\rho_{hv}$  (0.7 - 1, influenced by particle homogeneity) and a liquid/melting/ice phase indicator to distinguish nine classes of hydrometeor types. These classes consist of: aggregates (AG), ice crystals (CR), light rain (LR), rimed particles (RP), rain (RN), vertically-oriented ice crystals (VI), wet snow (WS), melting hail (MH), ice hail-high density graupel (IH/HDG) and no classification (No valid radar data - NC). Within the context of this study, light rain and rain were aggregated into a single rain class and vertical ice was aggregated into the crystals class.

### 4.3.2 Vertical cone extraction

Because this study aims to propose a more localised vertical profile correction technique, the filtered and corrected volumetric radar data needs to be sampled at scales small enough to capture the spatio-temporal variability and large enough to give a robust estimate of the vertical profile at each location. Also, rather than extracting a vertical column of a certain size, vertical cones such as illustrated in Fig. 4.2 were extracted. The motivation for this is twofold: on the one hand it accounts for the decrease in the number of measurements at higher altitudes by increasing the sampling size of the cone, and on the other hand it follows the assumption that precipitation observed at a certain point of interest  $x, y$  on the grid (Fig. 4.1), may have originated from a much wider region aloft. As described in Roe (2005), the terminal fall speed of hydrometeors varies between 1 m s<sup>-1</sup> for snow and 10 m s<sup>-1</sup> for heavy rain (excluding hail stones). This implies that when taking into account a range of horizontal wind speeds from 5 to 30 m s<sup>-1</sup>, a hydrometeor originating at 3 km altitude may get advected



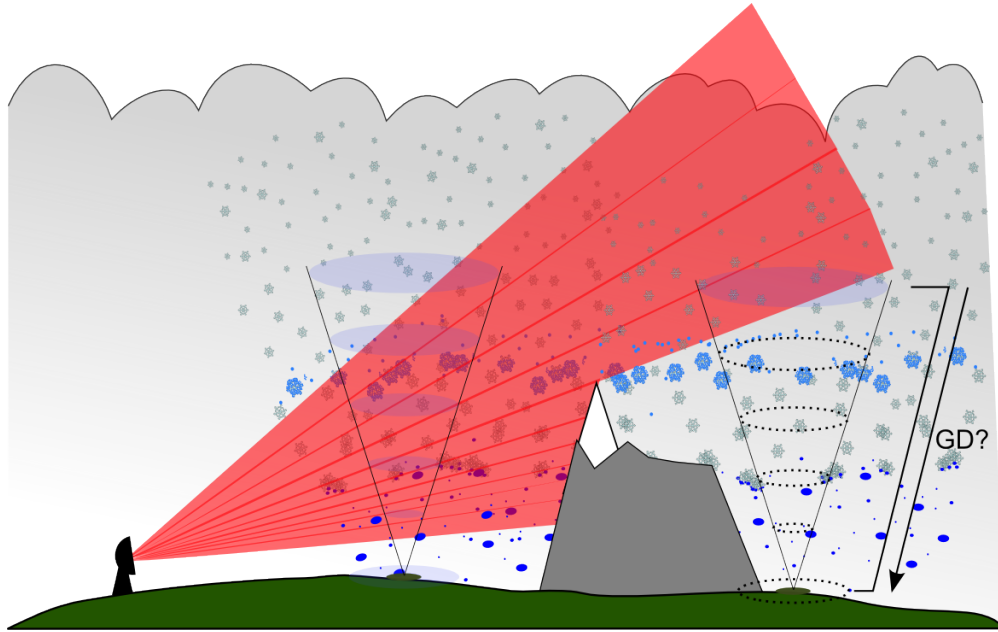


Figure 4.2 – Cones are extracted in well-visible regions of the radar and used to train the ANN. The trained ANN model can then be used to extrapolate to the ground level in regions with reduced visibility.

anywhere between 1.5 and 90 km before reaching the surface. However, the choice in the size of the base and top of the cones is also related to grid spacing: as will become clear, in this study we have chosen cone sizes which do not overlap or touch at the base and partly overlap at the top. The cone size is furthermore related to the maximum distance of the grid and the vertical resolution of the cone through the number of available samples at each altitude. Considering that for the lowest elevation angle the  $1^\circ$  beam width diameter exceeds 1 km at distances further than 60 km, we estimate that a 500 m vertical resolution is the highest possible. Given the 500 m vertical resolution and distances of  $>60$  km from the radar, it was estimated that cones with a 4 km radius at the base and a 10 km radius at the top, would have sufficient samples at each height level (Table 4.1). In order to preserve some spatio-temporal consistency and to further increase the number of samples at each height level, the cones at each location were aggregated over up to 30 minutes (6 previous scans).

The variables (hydrometeor class (HC) proportions and  $Z_H$ ) were extracted within height level bands of 500 m at levels ranging from 1500 m to 10 km altitude. The lowest available level (1000 m a.s.l.) was considered the “ground” reference. For  $Z_H$  the average reflectivity within each height band was calculated, including measures of dispersion and location (standard deviation, percentiles 16, 25, 50, 75 and 84). For the hydrometeor classes the number of pixels pertaining to each class was counted and these were transformed into proportions after the temporal averaging. The temporal averaging was performed as a last step so that each individual cone could still be stored and examined and such that experiments could be performed with shorter temporal averaging.

$h_b$ [m]	$h$ [m]	20-30 km	40-50 km	> 60 km
750				
1250	1000	154	141	122
1750	1500	178	171	158
2250	2000	215	201	131
2750	2500	191	182	163
3250	3000	218	204	205
3750	3500	214	181	47
4250	4000	279	177	152
4750	4500	251	174	100
5250	5000	365	251	189
5750	5500	301	194	94
6250	6000	371	343	294
6750	6500	339	273	129
7250	7000	392	353	255
7750	7500	379	354	239
8250	8000	393	379	276
8750	8500	409	363	296
9250	9000	401	379	293
9750	9500	384	380	344
10250	10000	406	383	350

Table 4.1 – Median number of pixels for 500 m height intervals (boundaries in first column) at increasing distances from the radar based on geometry for a single volume scan and a cone with 4 km radius at the base and a 10 km radius at the top. The altitudes given in the first two columns are in metres above sea level.

The target value  $y$  which the ANN was required to predict was chosen to be the vertical growth and decay (GD) of precipitation which was derived after the temporal averaging and for each height level  $h$ :

$$y = GD_{h-1\ km} = 10 * \log_{10} \left( \frac{Z_{h\ km}}{Z_{1\ km}} \right) \text{ [dB]} \quad (4.1)$$

The choice for trying to predict growth and decay was based on the accurate definition of the learning problem at hand; here we are interested in predicting the vertical change in reflectivity between the lowest visible height level and the ground, rather than in predicting the exact reflectivity value at the ground level. As such, the ANN had to be trained with the correct input data.

### 4.3.3 Selection of precipitation events

Since the calculation of the variables inside the cones is a costly operation in terms of computing time, there is some trade-off between the number of cones to be extracted per scan, and the number of precipitation events for which cones can be extracted within a reasonable amount of time. For this study 30 precipitation events over the course of three years (2016, 2017 and 2018) and covering a broad range of microphysical situations were selected. Within each event, one scan per hour was randomly selected, and for each scan the 6 previous scans (equalling 30 minutes in time) were also extracted. The temporal spacing between the extracted scans was adopted in order to avoid strong correlations between successive temporally averaged cones and allowed to further limit processing time. Details of the events are given in Table 4.2. Due to the higher frequency and duration of stratiform events these are slightly over represented in the data. This study will therefore also apply some event stratification.

Date	GWTWS Type	Duration [hours]	max / $\mu$ Windspeed [m/s]	Daily Precip [mm]	Date	GWTWS Type	Duration [hours]	max / $\mu$ Windspeed [m/s]	Daily Precip [mm]
08-01-2016	W (A)	11	5.8 / 1.6	11.1	28-06-2017	SW (A)	14	11.0 / 2.1	26.3
31-01-2016	NW (A)	10	11.4 / 2.7	11.1	10-07-2017	SW (A)	6	19.1 / 1.8	23.7
23-02-2016	W (A)	7	12.1 / 3.2	7.8	18-08-2017	SW (A)	4	9.9 / 1.5	35.7
02-03-2016	W (A)	7	21.0 / 2.35	7.1	31-08-2017	SW (A)	20	5.8 / 1.5	29.4
17-04-2016	SW (A)	17	9.8 / 1.9	17.6	01-09-2017	SW (A)	16	7.5 / 2.6	24.2
12-05-2016	LP (C)	21	10.4 / 2.6	31.9	12-11-2017	W (A)	9	23.5 / 3.3	14.6
23-05-2016	SE (A)	22	8.0 / 2.6	25.0	22-01-2018	NW (A)	22	9.4 / 2.2	29.1
16-06-2016	SW (A)	12	7.5 / 1.9	20.9	17-02-2018	W (A)	14	5.8 / 1.5	16.4
12-07-2016	SW (A)	19	6.6 / 1.4	47.9	28-03-2018	W (A)	13	9.9 / 2.2	6.1
25-10-2016	W (A)	20	5.9 / 1.2	20.8	30-04-2018	SW (A)	3	15.3 / 2.4	1.2
31-01-2017	NW (A)	23	5.7 / 1.3	34.7	14-05-2018	E (A)	7	6.8 / 1.7	9.6
09-03-2017	NW (A)	17	5.7 / 1.6	16.3	15-05-2018	N (A)	9	7.0 / 2.0	7.6
18-03-2017	NW (A)	11	9.8 / 1.7	11.1	22-05-2018	FP (C)	6	9.7 / 1.5	39.8
25-04-2017	W (A)	15	10.7 / 1.9	24.4	30-05-2018	HP (C)	2	9.5 / 1.8	0.0
12-05-2017	LP (C)	4	10.8 / 1.6	6.6	04-06-2018	FP (C)	2	13.9 / 1.8	0.8

Table 4.2 – Statistics for the precipitation events used in this study. Daily precipitation sums and wind speeds are from the ground station Cham at approximately 15 km distance from the Albis radar. For the GWT weather type classification (Weusthoff, 2011), LP, HP and FP represent High Pressure, Low Pressure and Flat Pressure situations respectively, the other acronyms are abbreviations of GWTWS flow directions. The letters A and C indicate advective or convective types.

## 4.4 Neural network and experimental setup

Machine learning algorithms are tools which, compared to traditional statistical data models, are fully non-parametric and designed to solve regression tasks in high-dimensional input spaces. This means that MLAs aim to obtain the best possible performance without making strong assumptions about the distributions of or dependency between the variables (see e.g. Kanevski et al. 2009). Artificial Neural Networks (ANN) are a type of MLA which are particularly well adapted to treating multi-dimensional input data and resolving non-linear problems and

the MultiLayer Perceptron (MLP) model used in this study is a feedforward ANN.

MLP models are typically composed of one input layer, one or more hidden layers and one output layer (Fig. 4.3). The neurons in the input layer correspond to the input variables (predictors), and the neurons in the output layer to the target variables (predictands). Each neuron is connected to the other neurons of the network with synaptic weights  $w_i$  (which can be positive or negative). The neuron itself integrates the input signals from the synapses  $s_i$  and applies a bounded, non-linear sigmoid activation function (typically logistic or hyperbolic tangent) to control the output of the neuron  $o_i$ . The combined effect of the hidden layer is that it performs a non-linear transformation on the weighted linear summation of the values coming from the input neurons.

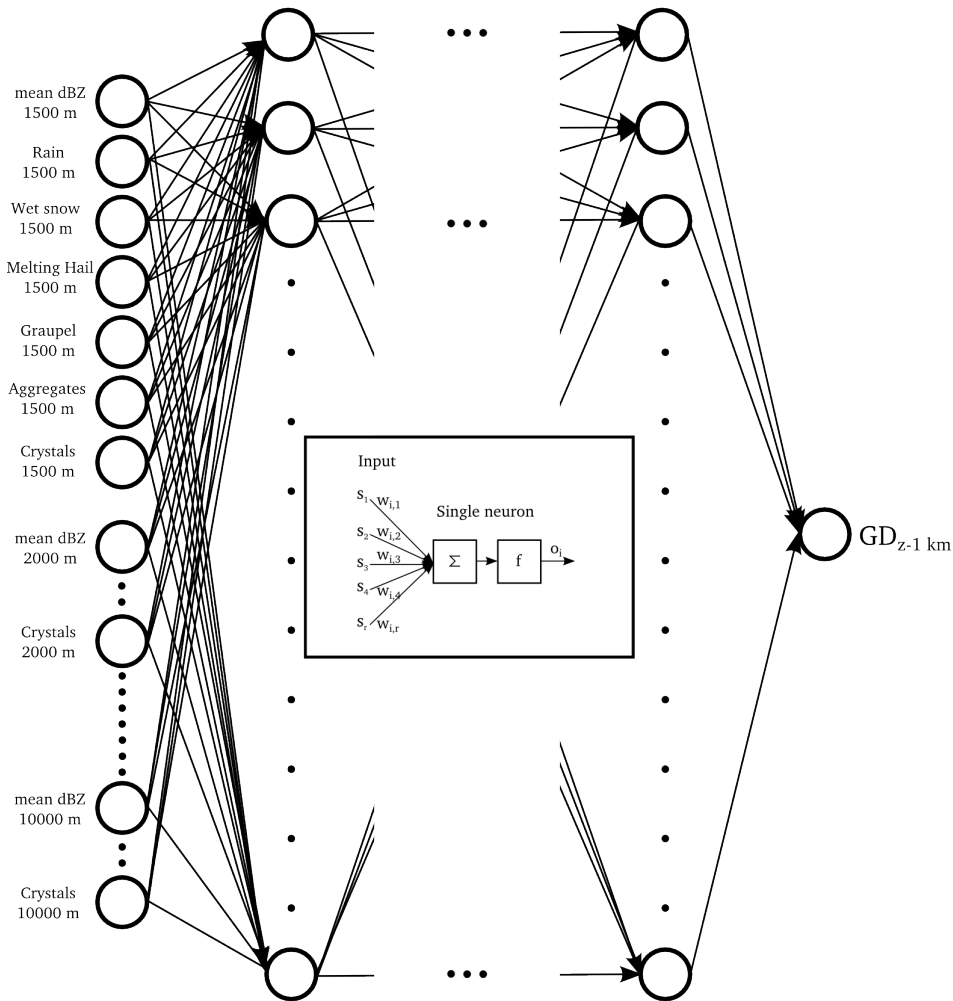


Figure 4.3 – Example of a multi-input single-output MLP model and set-up as used in this study. The number of input variables  $M$  equals the number of  $V$  variables (reflectivity, HC proportions)  $\times H$  height levels used.

The training of the MLP is then achieved by performing an iterative optimisation of the network

weights  $\mathbf{w}$  to minimise the mean squared error loss function between the predicted and the target values in the output neuron:

$$E_{MSE}(\mathbf{w}) = \frac{1}{N} \sum_{i=1}^N \left( y_i^{obs} - y_i^{pred}(\mathbf{x}, \mathbf{w}) \right)^2 \quad (4.2)$$

Linking individual neurons with sigmoid shaped functions in a network has the advantage of creating a system which is able to model complex non-linear behaviour (Cybenko, 1989). Whereas a single neuron merely fits a sigmoid-shaped function, the weighted combination of several neurons (or sigmoid functions) can reproduce the complex, non-linear dependency of the data. This also means that provided that there are a sufficient number of neurons and a non-constant, non-decreasing activation function at each hidden neuron, an ANN can model any function with the desired precision (Cybenko, 1989; Hornik et al., 1989). This means that the architecture of the network may lead to potential overfitting. Overfitting and the presence of multiple minima may lead to the inability of the ANN to generalise the learnt patterns. While overfitting may be addressed by early stopping or using separate training and validation datasets, local minima can be avoided by using stochastic gradient descent optimisation algorithms.

Thus, the hyper-parameters of MLP models are the number of hidden layers, the number of hidden neurons within these layers, the type of activation function and the learning rate for the update of the weights. The last parameter influences the speed at which the MLP converges. Given enough iterations, these are not as important for the performance of the MLP as the network architecture. The number of hidden layers and neurons must therefore be tuned accordingly. Models with different network architectures can then be compared based on their performance on new data, but also based on their complexity.

The training of the MLP, as well as the evaluation of its performance is achieved by using different datasets. Typically the dataset is split up into training (60%), validation (20%) and testing (20%) datasets. While the model is trained with the training dataset to find the appropriate weights to minimise the training error, it is simultaneously applied to the validation dataset in order to evaluate the predictive performance of the MLP. The training error will continue to decrease, however as soon as the model starts overfitting the training data, the validation error will start to increase. The set of weights with the lowest training and validation error is retained as the best model.

Finally, the testing dataset can then be used as a completely impartial dataset to evaluate the models. In this study, all three datasets contain cones from separate precipitation events with as a constraint that each dataset includes at least one event from every season.

### 4.5 Exploratory data analysis and results

The goal of exploratory data analysis (EDA) is the extraction of some useful information before applying MLAs to the dataset. The efficiency and accuracy of MLA methods depend critically on the quality and quantity of the data. EDA may therefore be useful for the identification of relevant variables, existing patterns and outliers or errors in the dataset.

#### 4.5.1 EDA: Vertical profiles of hydrometeor proportions

In order to evaluate the ability of the vertical cones to capture the vertical structure of precipitation and as a part of the EDA, the vertical profiles of hydrometeor proportions, reflectivity and GD have been plotted. Figure 4.4 shows the medians and quartiles of the vertical profiles for different events calculated over the entire spatial domain and for a single 30 minute time step. The profiles of hydrometeor proportions show some distinctly different features for events with snow at the ground, stratiform and convective events. For the event with snow until the ground level (left panel Fig. 4.4) high proportions of aggregates and rimed particles can be observed at lower altitudes, while above 5500 m a.s.l. only crystals are present. For the stratiform event, crystals also dominate at altitude levels above 5500 m a.s.l., but a distinct increase in wet snow around 2000 m a.s.l. indicates the presence of a melting layer and rain dominates at the lower altitude levels. For the convective event, rain dominates up until 3000 m a.s.l. and important proportions of crystals, aggregates and rimed particles can be observed until at least 10 km altitude.

The vertical profiles of hydrometeor proportions in Fig. 4.4 indicate that a) different event types can be distinguished with the HC proportions from the cones, b) the sampling strategy (cones size, grid spacing) is sufficient to differentiate between events and c) some types of events may benefit more than others from information from aloft.

Vertical profiles were also calculated for each single cone location and averaged over the entire dataset. This was done to exclude cones with consistently missing data at certain height levels due to geometrical constraints; this is different from the information in Table 4.1 which shows the theoretical median number of pixels within cones at different ranges from the radar. Indeed, based on this analysis 85 coordinates situated at typical angles with respect to the radar and mostly at further distances from the radar were removed from the dataset. The reasons for removing these data points were that MLAs can not handle missing data values and that these cones resulted in extreme GD values in the observation dataset. For the same reasons, cones which were less than 10% filled in the bottom 4000 metres of the cone were also removed, such that a total of 17123 cones remained for input in the ANN models.

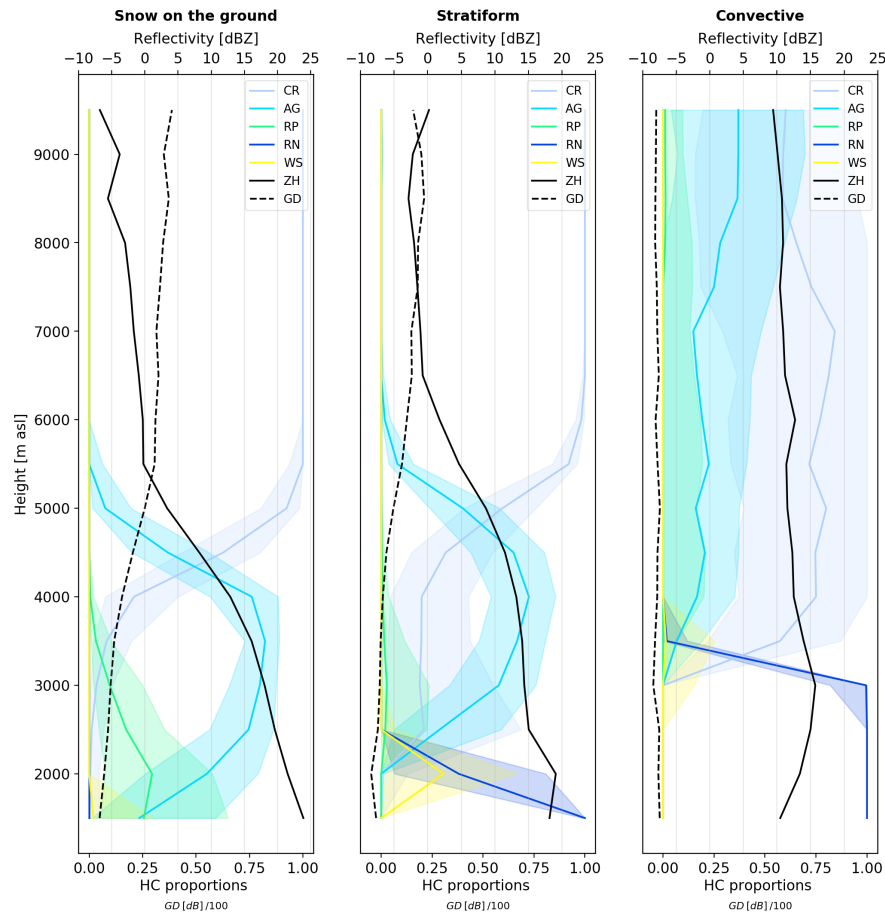


Figure 4.4 – Examples of vertical profiles of hydrometeor proportions for three different events. The thick lines show the average value and the shading represents the quartiles calculated over the entire spatial domain for a single 30 minute time step.

#### 4.5.2 Results: ANN predictions of growth and decay

Two main types of ANN models were trained and tested within the scope of this study: one model was trained with only values of average reflectivity at each height level (“dBZ-only model”) and the second was trained with the average values of reflectivity and HC proportions of rain, wet snow, rimed particles, aggregates and crystals at each height level (“HC + dBZ-model”). Occurrences of hail and melting hail were so rare in the considered dataset that these were not used as input variables. For each of these two ANN types, separate models starting at different height levels have been trained (i.e. starting at 1500 m a.s.l. and upwards, starting at 2000 m a.s.l. and upwards etc.). Because the number of input neurons was equal to the number of variables  $\times$  the number of altitudes, the dBZ-only model for example had 20 neurons in the input layer for the ANN starting at 1500 m a.s.l, 19 neurons for the ANN starting at 2000 m a.s.l. and so forth. For the HC + dBZ-model these numbers were 110 and 104 respectively.

The 2D histogram plots in Fig. 4.6 show the observed (x-axes) and predicted (y-axis) GD for the HC + dBZ-models (top row) and dBZ-only (bottom row) trained with data from different altitudes and upwards (columns). As predictions are made from increasingly higher altitudes, both the observations and the predictions move towards growth, as can be expected. The colouring of the plots indicates the point density, and while the blue points are single observations and thus show more scatter, the areas with high point density (red/orange) fall better along the identity line for the HC + dBZ-model than for the dBZ-only model. Especially for predicting GD from 2500 m a.s.l and aloft, the dBZ-only models seem to have difficulty with predicting growth values higher than 10 dB.

The 2D histogram plots in Fig. 4.6 are summarised in Fig. 4.5 which shows the Root Mean Squared Error (RMSE) and correlation coefficient ( $\rho$ ) of the models. It can be observed that the model with HC proportions performs consistently better than the model without HC proportions (i.e. at equal RMSE values, the HC + dBZ model can predict from altitudes between 500 and 1000 metres higher than the dBZ only model). The RMSE for both model types seems to level off for ANNs trained with data starting from 4000 m a.s.l. and aloft, indicating that the models show no skill for predictions made from these height levels. At the lowest height level (1500 m a.s.l.) the dBZ-only model and the HC + dBZ-model seem to result in the same amount of error. A possible explanation for this is that for the prediction of GD between the ground and 500 metres aloft, the average reflectivity at 1500 m a.s.l. is the dominant variable also for the HC + dBZ-model. The differences between the models and observations at this and subsequent height levels is analysed in more detail in the following section.

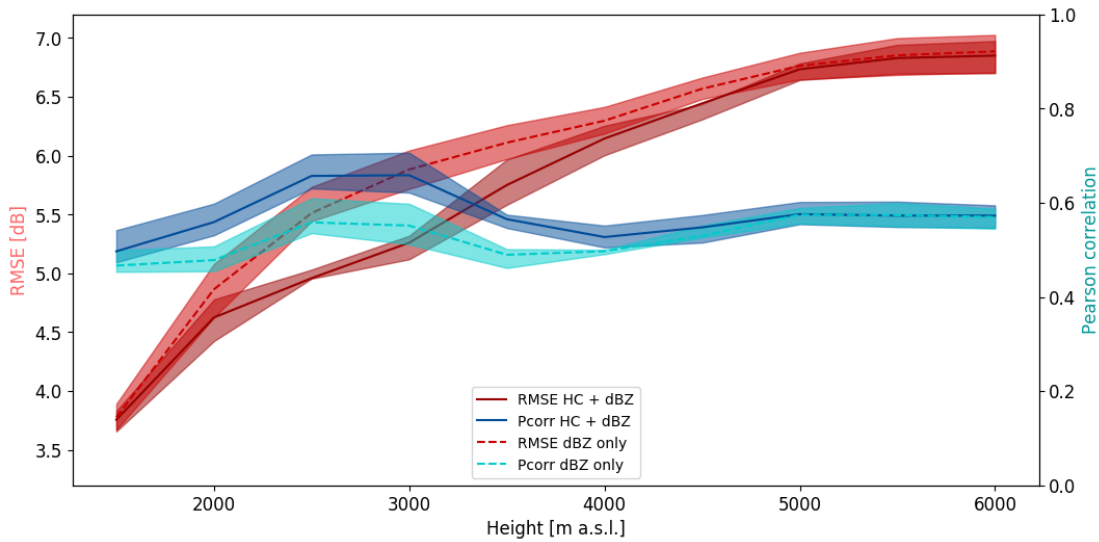


Figure 4.5 – RMSE and Pearson correlation coefficient for dBZ only-models and HC + dBZ-models trained with data starting from increasing altitude levels. The thick lines indicate the average values and the shading the quartiles calculated over ten model runs using different combinations of events for the training, validation and testing datasets.



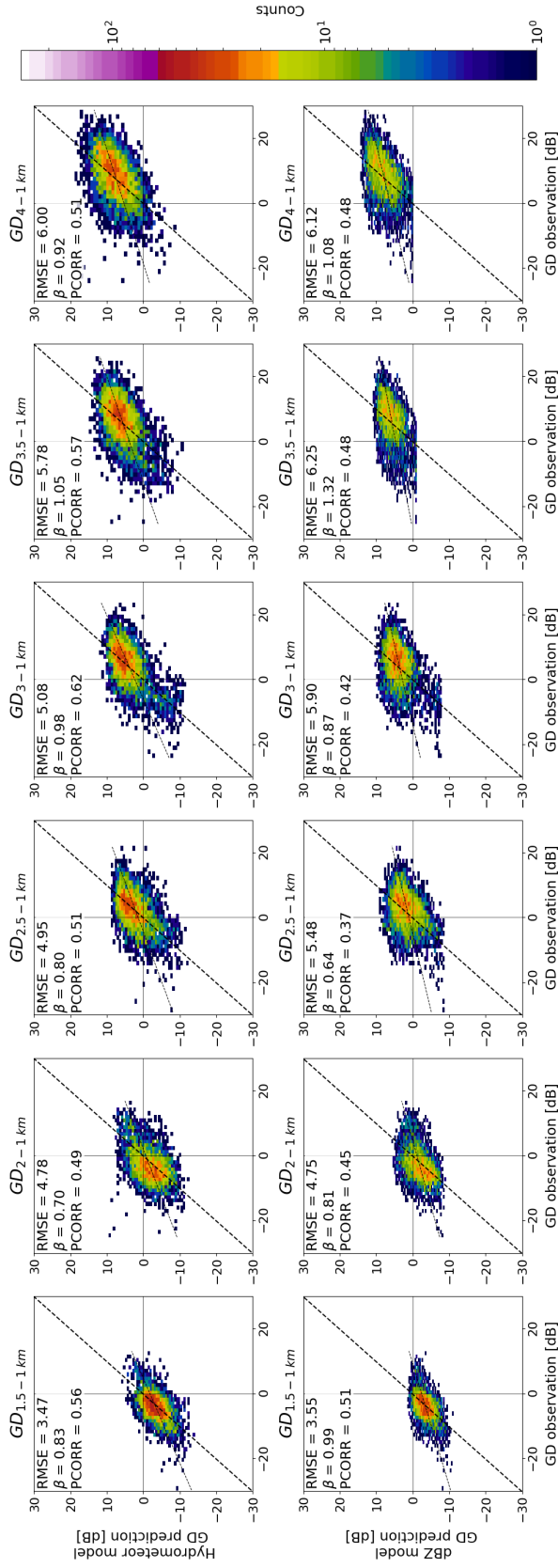


Figure 4.6 – 2D histogram for observed (x-axes) and predicted (y-axes) GD for the HC + dBZ-models (top row) and dBZ-only models (bottom row) trained with data starting from higher altitude levels and aloft (columns). The number of points in each bin is indicated in colour.

### Results: 2D histogram matrices of growth and decay

The matrices in Fig. 4.7 show the 2D histograms for GD based on combinations of HC proportions and average reflectivity values at the lowest height levels (1500 m a.s.l. and 2500 m a.s.l.) for the observed data (left column), the HC + dBZ-model (middle column) and the dBZ-only model (right column). The GD values were calculated based on the reflectivity at that height level and the 1000 m a.s.l. reference level. The 2D histogram matrices allow to distinguish different GD patterns for different combinations of variables. Overall, higher average reflectivity values at any altitude  $h$  lead to observed decay between that altitude  $h$  and the ground reference and, inversely, lower reflectivity values at altitude  $h$  lead to more observed growth. This is also reflected by the models. However, more specific patterns can also be observed, such as the pronounced growth values for cones with low to average reflectivity values at altitude  $h$  and high proportions of aggregates or any presence of rimed particles at that same altitude  $h$ . While these patterns are also visible in the HC + dBZ-model output, the dBZ-only model is unable to reproduce these.

In order to evaluate how well the models reproduce the observed GD patterns, figures 4.8 and 4.9 show the 2D histogram error matrices for predictions from 1500 m and 2500 m a.s.l. respectively. For each of the combinations of variables the binned 2D histogram for the observations was subtracted from the binned 2D histograms of the model outputs such that positive values in figures 4.8 and 4.9 show model overestimation and negative values correspond to model underestimation.

Overall, the errors for the dBZ-only model have a greater amplitude than the errors for the HC + dBZ-model (figures 4.8 and 4.9). Most notable is the overestimation by the dBZ-only model for cases where Crystals are present, for example the RMSE for combinations of Crystals and average reflectivity at 1500 m a.s.l. for the HC + dBZ-model is 3.05 dB while for the dBZ-only model it is 4.64 dB. The dBZ-only model also particularly underestimates for cases with Rimed Particles and high proportions of Aggregates. The HC + dBZ-model also underestimates cases with Rimed Particles, though only when predicting from 1500 m altitude levels and less so than the dBZ-only model (combinations of Rimed Particles and average reflectivity at 1500 m a.s.l. result in an RMSE of 2.23 dB for the HC + dBZ-model and 2.90 dB for the dBZ-only model). Overall, the HC + dBZ-only model shows less patterns in the errors and the highest errors are located at the edges of the distributions and thus more likely related to outliers in the observations.

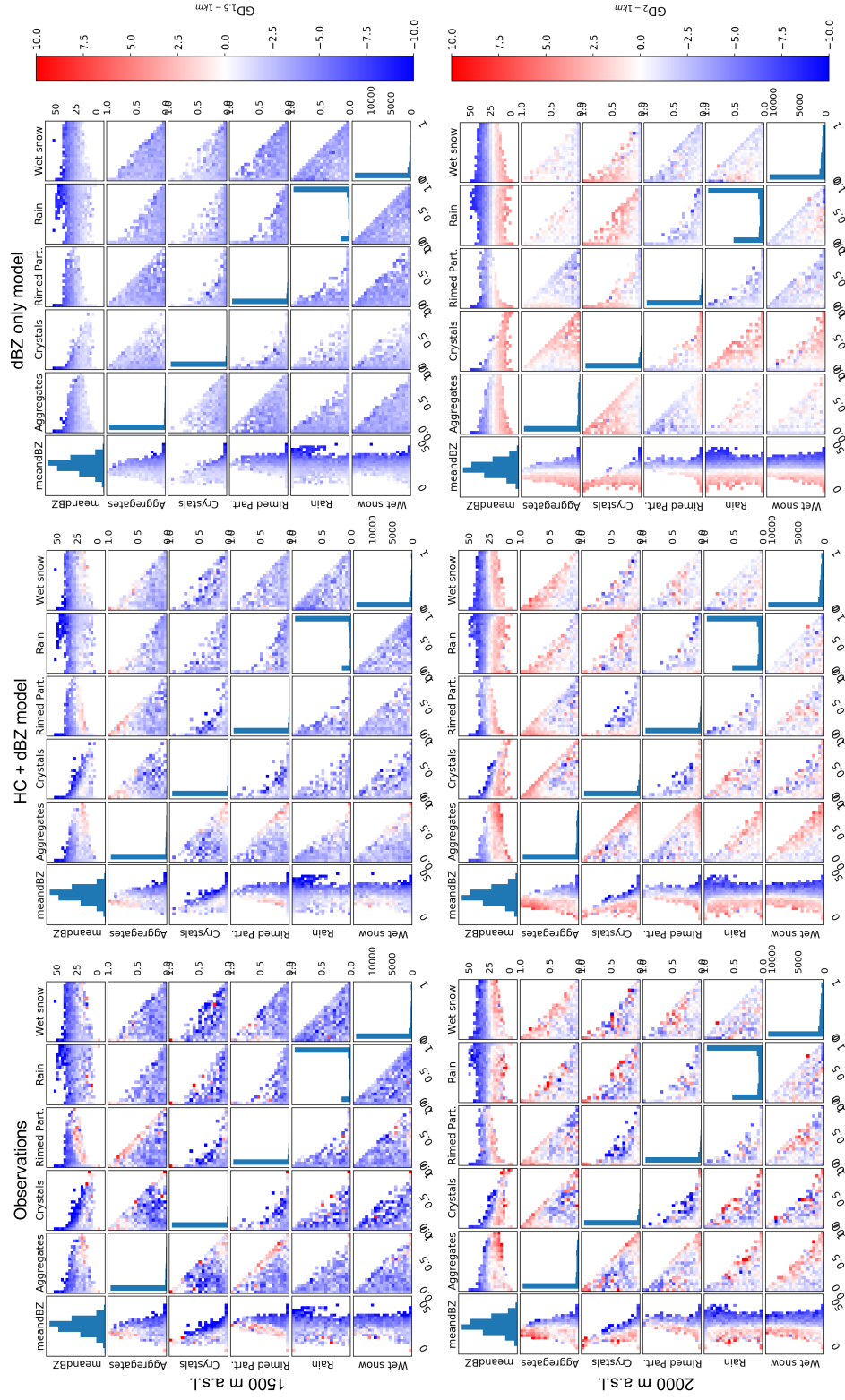


Figure 4.7 – 2D histogram matrices for 1500 m a.s.l. (top row) and 2500 m a.s.l. (bottom row) for observed data (left), HC + dBZ-model (center) and dBZ-only model (right). The colour of each bin is based on the average GD value.

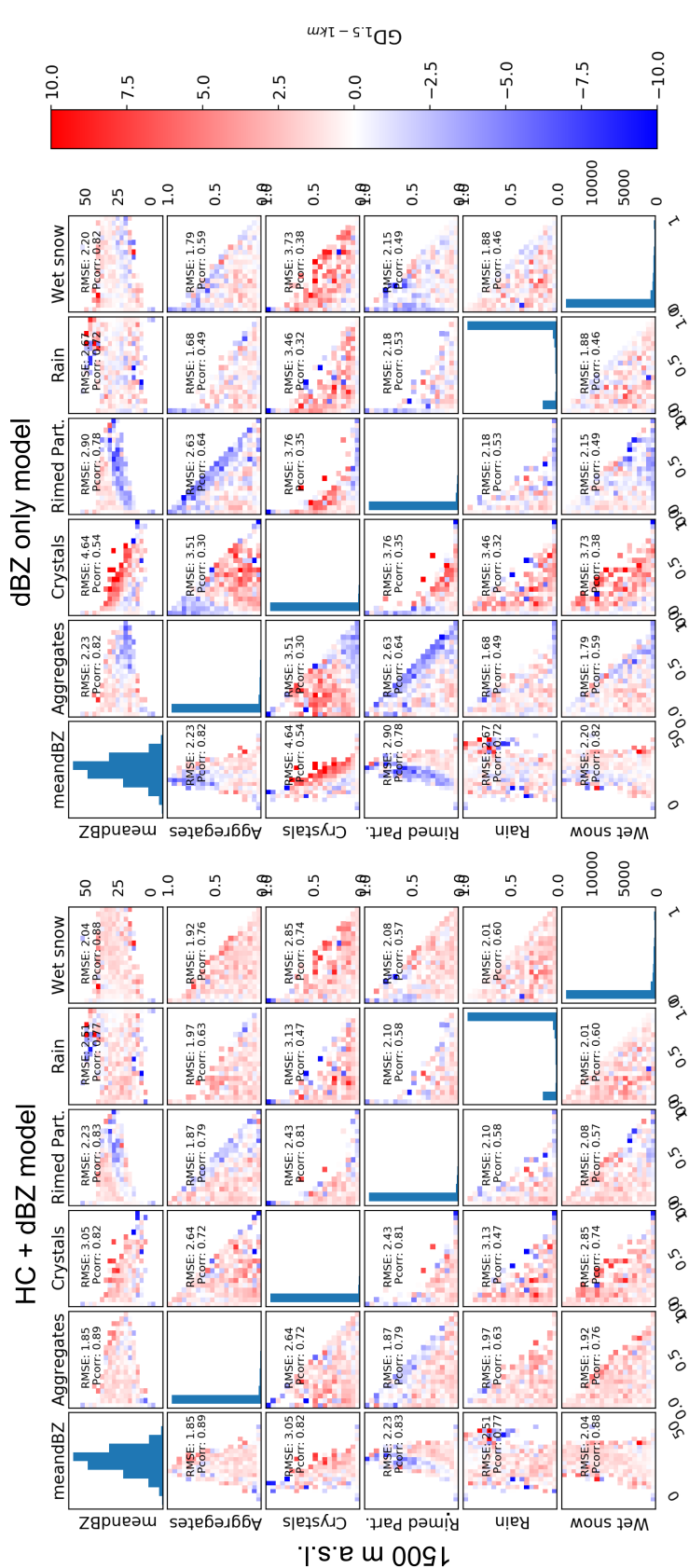


Figure 4.8 – 2D histogram error matrices from 1500 m a.s.l. for HC + dBZ-model (left) and dBZ-only model (right). The colour of each bin is based on the difference between the observed binned average and the binned average of the model output.

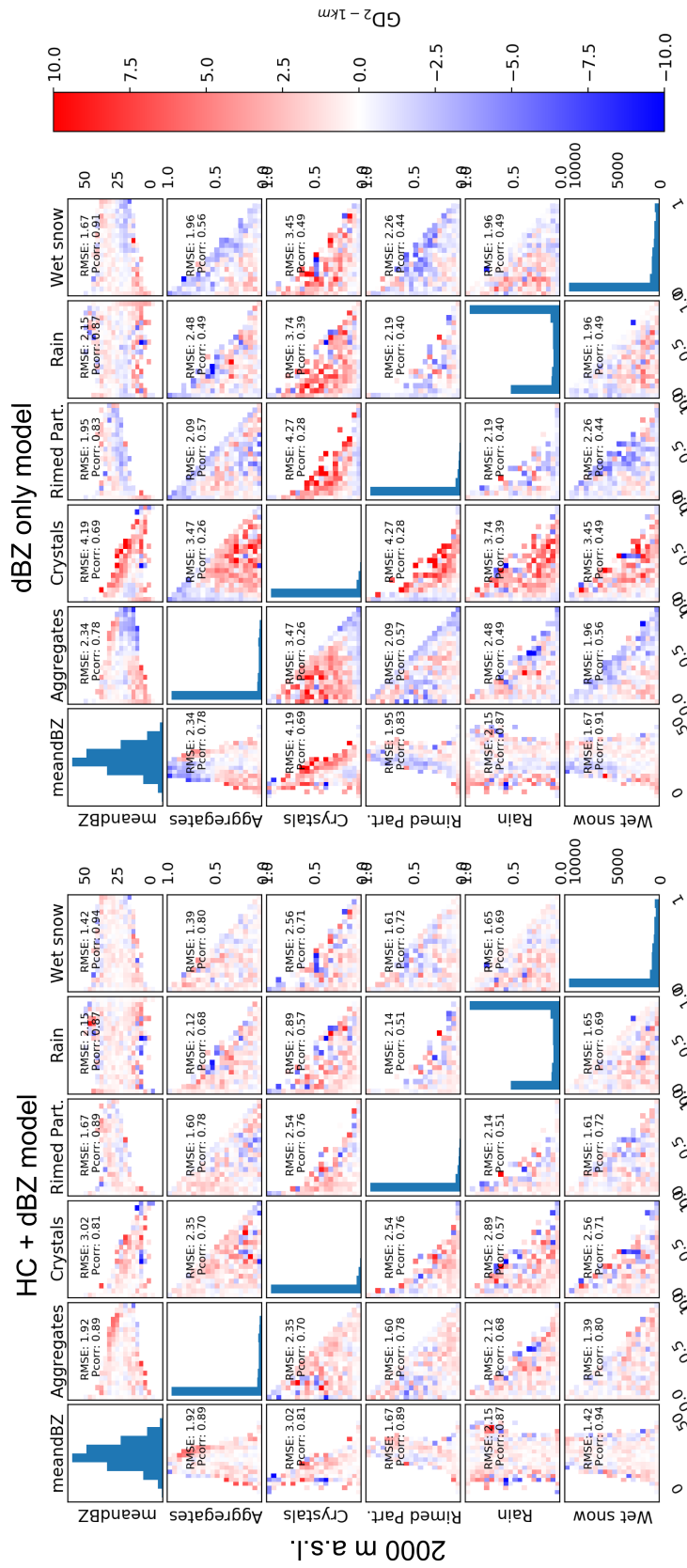


Figure 4.9 – 2D histogram error matrices from 2500 m a.s.l. for HC + dBZ-model (left) and dBZ-only model (right). The colour of each bin is based on the difference between the observed binned average and the binned average of the model output.

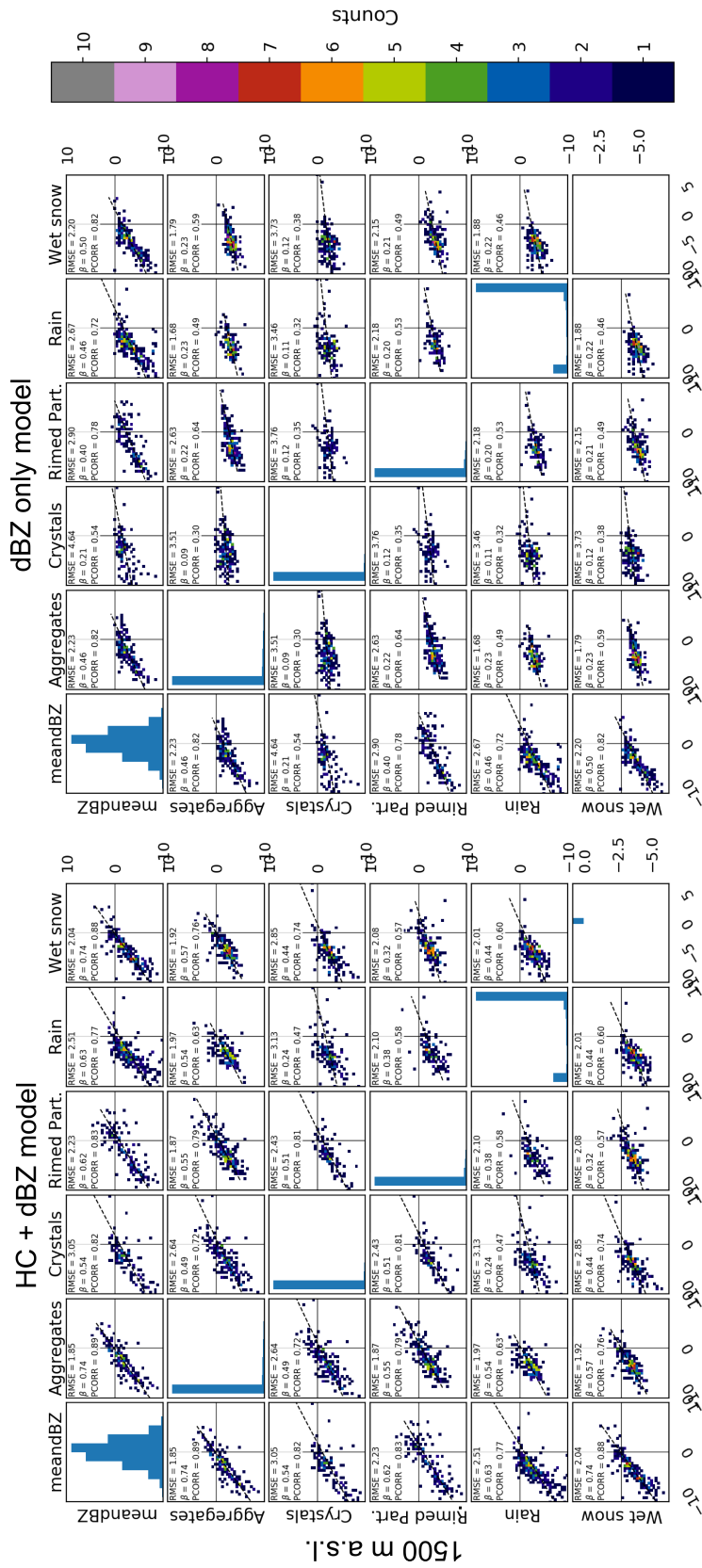


Figure 4.10 – 2D histogram matrices for observed (x-axes) and predicted (y-axes) GD for the HC + dBZ-model (left) and dBZ-only model (right) trained from 1500 m a.s.l. and data aloft. The number of points in each bin is indicated in colour.

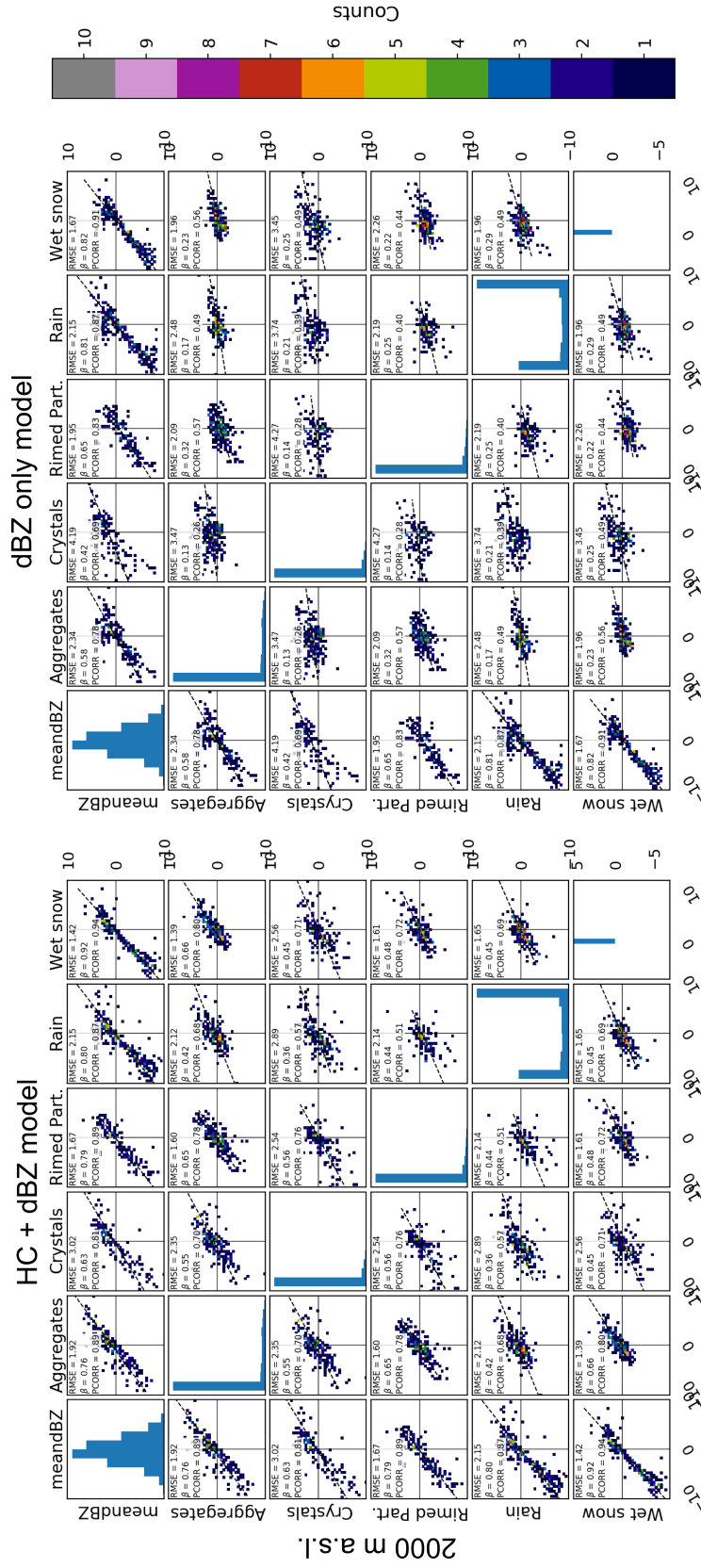


Figure 4.11 – 2D histogram matrices for observed (x-axes) and predicted (y-axes) GD for the HC + dBZ-model (left) and dBZ-only model (right) trained from 2500 m a.s.l. and data aloft. The number of points in each bin is indicated in colour.



Figures 4.10 and 4.11 show the same types of 2D histograms as in Fig. 4.6 but for the binned statistics shown in figures 4.7, 4.8 and 4.9. The numbers mentioned in the discussion below are for 1500 m a.s.l. but the observations are also valid at 2000 m a.s.l. For the HC + dBZ-model the observed and predicted GD for combinations of average reflectivity and any hydrometeor class show good agreement with high regression coefficients ( $0.94 < \beta < 1.22$ ) and correlation coefficients ( $> 0.76$ ). For combinations of hydrometeor classes, and especially Rain + Aggregates or Rain + Rimed Particles the performance of the HC + dBZ-model is not as good (correlations drop to 0.63 and 0.58 respectively) though this could also be related to the more complicated and less frequent nature of situations with these combinations of hydrometeor classes. For the dBZ-only model, the agreement between observed and predicted GD for combinations of average reflectivity and hydrometeor class is much lower than for the HC + dBZ-model. For combinations of hydrometeor classes the dBZ-only model gives similar predictions for the whole range of observed GD values.

### Comparison ANN predictions with traditional methods

The comparison between the ANN model outputs and traditional VPR correction techniques is made by adding the predicted GD to the lowest reflectivity measurement and comparing the predicted reflectivity at the ground level with the observed reflectivity:

$$RMSE = \frac{1}{N} \sum_{i=1}^N \left( dBZ_i^{obs} - dBZ_i^{pred} \right)^2 \quad (4.3)$$

Where  $dBZ_{pred}$  for the ANN models is obtained by:

$$dBZ_{pred} = dBZ_h + GD_{h-1\ km} \quad (4.4)$$

The traditional models considered are:

1) performing no correction or assuming *vertical stationarity* by taking the lowest available reflectivity measurement:

$$dBZ_{pred} = dBZ_h \quad (4.5)$$

2) a simple *spatially averaged* profile, obtained by taking the average GD from all the cones (C)



within the study area for a single time step

$$dBZ_{pred} = dBZ_h + \frac{1}{C} \sum_{c=1}^C \left( GD_c^{h-1 km} \right) \quad (4.6)$$

3) the *meso-beta* profile correction factor which is calculated operationally. For each altitude  $h$  the correction factor is extracted from the profiles and applied to the average reflectivity value at altitude  $h$  from the cone. More details on the calculation of the correction factor can be found in [Germann and Joss \(2002\)](#).

Altitude [m a.s.l.]	vertical station.	spatial average	meso-beta profile	dBZ-only ANN	HC + dBZ ANN
<b>1500.0</b>	5.62   <b>0.82</b>	8.67   <b>0.82</b>	5.14   <b>0.84</b>	3.55   <b>0.85</b>	3.47   <b>0.86</b>
<b>2000.0</b>	5.85   <b>0.70</b>	7.43   <b>0.70</b>	5.45   <b>0.74</b>	4.75   <b>0.72</b>	4.78   <b>0.73</b>
<b>2500.0</b>	6.12   <b>0.60</b>	7.20   <b>0.60</b>	5.47   <b>0.71</b>	5.48   <b>0.59</b>	4.95   <b>0.68</b>
<b>3000.0</b>	7.81   <b>0.50</b>	10.93   <b>0.50</b>	5.64   <b>0.63</b>	5.90   <b>0.50</b>	5.08   <b>0.66</b>
<b>3500.0</b>	9.27   <b>0.41</b>	13.98   <b>0.41</b>	5.96   <b>0.55</b>	6.25   <b>0.43</b>	5.78   <b>0.53</b>
<b>4000.0</b>	10.70   <b>0.40</b>	17.70   <b>0.40</b>	6.69   <b>0.46</b>	6.12   <b>0.43</b>	6.00   <b>0.47</b>
<b>4500.0</b>	12.95   <b>0.37</b>	22.72   <b>0.37</b>	7.95   <b>0.39</b>	6.20   <b>0.40</b>	6.27   <b>0.39</b>
<b>5000.0</b>	15.84   <b>0.29</b>	28.78   <b>0.29</b>	10.14   <b>0.30</b>	6.43   <b>0.32</b>	6.37   <b>0.34</b>
<b>5500.0</b>	18.57   <b>0.25</b>	34.63   <b>0.25</b>	12.41   <b>0.26</b>	6.54   <b>0.28</b>	6.37   <b>0.32</b>
<b>6000.0</b>	19.98   <b>0.21</b>	37.58   <b>0.21</b>	13.69   <b>0.21</b>	6.63   <b>0.24</b>	6.53   <b>0.29</b>

Table 4.3 – RMSE and **Pearson correlation coefficient** scores for various VPR correction techniques applied to an independent test dataset of 3884 cones.

The RMSEs for each of these VPR models as well as the dBZ-only and HC + dBZ models were calculated over a completely independent test dataset of 3884 cones and are given in Table 4.3. The spatially averaged profile based on the averaged cones shows the worst results, while assuming vertical stationarity may be feasible at lower elevations but results in large errors when the lowest visible elevations are higher than 2000 m a.s.l. The operational meso-beta profile is extracted from the well-visible regions close to the Albis radar and gives a correction factor with respect to the reference altitude used operationally and which is set to 1500 m a.s.l. for Albis. Since the meso-beta profiles have no information at 1000 m a.s.l. altitude, the initial error for predictions from 1500 m a.s.l. to 1000 m a.s.l. is approximately 1.6 dB higher than for the ANN models. Because the meso-beta profile correction factors are calculated such as to obtain a more or less constant rain rate in the vertical, the RMSE of the meso-beta profile also remains quite constant up to 4000 m a.s.l. The increase in RMSE at higher altitudes is probably because the required correction exceeds the maximum threshold for the operational correction factor. Compared to the meso-beta profile the ANNs show some improvement:

the dBZ-only model for height levels up to 2000 m a.s.l. and the HC + dBZ-only model for all height levels. As was observed in Fig. 4.5 the error levels off around 4000 m a.s.l. for both ANN models. This may be partly explained by some over representation of stratiform events in the dataset which are less developed in the vertical so that the models have very little information available at these altitudes.

### 4.6 Conclusions

The aim of this study was to propose a more localised vertical profile (VPR) correction technique by making use of machine learning algorithms (MLA) and by exploiting polarimetric radar information through the use of hydrometeor types and their proportions. An important part of the work consisted of establishing the foundations for the use of MLA for the investigation of the vertical structure of precipitation. Vertical cones were extracted on a regular grid up to 60 km distances and in the well visible regions of the Albis radar. The cones were divided into height levels from 1500 m a.s.l. up to 10 km a.s.l. with a 500 m vertical resolution. For each 500 m height level band, the average reflectivity values and hydrometeor proportions were calculated and used as inputs for the Artificial Neural Network (ANN) model. The target value or predictand for the ANN model was the vertical change in reflectivity (or growth and decay (GD)) between each height level and the ground level (1000 m a.s.l.). A total of 30 precipitation events were randomly split into training, validation and testing datasets, each containing data from separate events. The ANN was then trained with the training and validation datasets and its performance could be evaluated with a completely independent test dataset.

Exploratory data analysis (EDA) of the vertical cone data allowed to further filter the dataset and to exclude cones with consistently missing values at certain height levels due to the geometrical constraints related to the scan strategy. EDA also allowed to verify that the cones could successfully capture the vertical structure and hydrometeor proportions of the precipitation events.

In order to evaluate the potential of information on hydrometeor classes (HC) to improve quantitative precipitation estimates (QPE) in Switzerland, two main types of ANN were trained: one with the average reflectivity values at different height levels (dBZ only-model) and one with the average reflectivity values and hydrometeor proportions at each height level (HC + dBZ-model). The ability of each model to extrapolate the radar measurements to the ground level was then assessed by progressively removing information at the lower height levels of the vertical cones and retraining the ANNs. It was found that, for equal values of RMSE, the HC + dBZ-model could predict from altitudes between 500 and 1000 metres higher than the dBZ only-model. A more in-depth analysis of the GD patterns as a function of hydrometeor types, indicated that the dBZ-only model overestimated (underestimated) GD especially in cases where Crystals (Aggregates) were present.

Finally, the ANN models were compared to simplified traditional VPR correction techniques by adding the ANN predicted GD to the lowest observed reflectivity value. The other approaches

considered were vertical stationarity of reflectivity, a spatially averaged profile and the operational meso-beta profile which was extracted for each time step and applied to the cone data. It was found that the dBZ only-model had lower RMSEs at altitudes up to 2000 m a.s.l. while the HC + dBZ-model performed better at all height levels. The higher error observed for the meso-beta profile correction technique may have been partly caused by the fact that this method uses 1500 m a.s.l. as the reference level, and not 1000 m a.s.l. The performance for both the dBZ only-model and the HC + dBZ-model levels off above 4000 m a.s.l., suggesting that the models have little or no predictive skill above this altitude. In order to better evaluate and compare the proposed ANN models to existing techniques, it would be valuable to also compare their outputs with rain gauge estimates at the ground level. In this case, a rainfall rate calculated on the basis of the predominant hydrometeor class could substitute the reflectivity-rainfall rate relationship. Future work should also include a sensitivity analysis of the contributions of the input variables, as this would allow to remove redundant predictors and so further improve the models. Similarly, an evaluation of the influence of the geometry and spacing of the cones on the final result (within the aforementioned constraints related to processing time, the resolution of the radar measurements and visibility at lower height levels) would allow to further improve the results of this method. The here presented cone extraction and evaluation of the method has been performed entirely on data from the Albis radar. It would be interesting to perform and compare the vertical cone correction method on one of the high altitude radars in Switzerland.

## 5 Conclusions and outlook

### 5.1 Summary

The objective of this thesis was to contribute to the improvement of quantitative precipitation estimation at the ground in the Alps, through the analysis of the spatial and temporal variability of polarimetric weather radar signals. This topic was addressed in three main chapters which covered radar monitoring and stability, the spatio-temporal variability of the melting layer in the Alpine regions and the potential for the inclusion of polarimetric radar variables in a more localised vertical profile correction approach.

Errors in quantitative precipitation estimates by radar are caused by many factors, and the accuracy and quality of the polarimetric weather radar measurements which, in turn, depend critically on the calibration and stability of the instrument, is highly important. Numerous methods for radar calibration and monitoring, including methods based on ground clutter returns, exist. However, these are based on the probability distributions of the returns from large clutter areas (e.g. [Silberstein et al., 2008](#)) and any temporal variability of the changes in the radar system may be masked by the median or average of many, temporally varying scattering objects. Chapter 2 provided some new perspectives on radar hardware monitoring using spectral analysis on the polarimetric radar signals returned by a single bright scatterer. Although the dispersion of the differential reflectivity values returned by this target was considered too large for calibration purposes, it was shown that valuable information on the state and stability of the radar hardware can still be obtained if different scales of variability and several polarimetric variables are considered. The better characterisation of the temporal variability of the returns of this target may benefit, for example, more in-depth case studies of the two-way attenuation of the signal returned by the single bright scatterer in the melting layer.

Nowadays it is considered that errors in radar QPE are predominantly caused by the vertical profile of reflectivity. A typical feature of the VPR in stratiform precipitation is the melting layer which is characterised by a dramatic increase in  $Z_H$ . The ML is often assumed spatially and temporally homogeneous by algorithms for QPE and VPR correction even though it is strongly

related to other factors (such as the vertical profile of temperature) which are variable in space and time. Moreover, the variability of the ML is quite poorly documented and limited to a few qualitative observations. The spectral analysis method which was used in chapter 2 to analyse the temporal variability of the radar signals, could be further extended and applied in chapter 3 to study the temporal and the spatial variability of the ML. It was shown that this method could be used to reliably describe the typical scales of variability of the ML. Then, based on polarimetric X-band radar scans from two measurement campaigns, the spatio-temporal variability of the ML could be characterised and compared for summer precipitation on the relatively flat Swiss plateau and for winter precipitation in a large inner Alpine valley in the Swiss Alps. Based on the results of this study it appears that the smaller spatial scales (15 to 10 km) contribute more to the total spatial variability of the ML in the case of the Alpine environment.

The findings in chapter 3 further emphasised the need to perform vertical profile corrections at smaller scales than currently considered by the operational methods. In addition to this, the relatively new dual-polarisation capability of the Swiss operational radar network could be better exploited in such a new approach. Thus, building on the availability of polarimetric data and a hydrometeor classification algorithm, chapter 4 proposed a framework for the application of machine learning methods to study the vertical structure of precipitation in Switzerland as well as a more localised vertical profile correction method. It was found that models which included information on hydrometeor proportions better represented the observed patterns of vertical change (growth and decay) in precipitation. More importantly, these models could predict from altitudes between 500 to 1000 metres higher than the models based on only reflectivity data. By providing a framework for analysis and showing the added value of the inclusion of hydrometeor proportions, this work thus opens up new possibilities to improve the currently operational algorithms for QPE and VPR correction at MeteoSwiss.

## 5.2 Contribution of this thesis

The main contributions of this thesis are:

- \* The application of fraction of variance explained by component as a method to interpret the spatial and temporal scales of variability of weather radar signals. Compared to the more commonly used spectral slopes, these have the advantage of being less compromised by averaging or conditioning of the input data and better summarising the contribution of each individual component.
- \* Some new perspectives on radar hardware monitoring using a single bright scatterer. It was shown that the combination of different sources of information based on the correlation between, and the spectral analysis of polarimetric signals can help better distinguish between environmental and instrumental influences.
- \* The characterisation and comparison of the spatio-temporal variability of the melting

layer for two different locations in Switzerland. The results indicated a higher contribution of smaller spatial scales to the total melting layer variability in the case of an Alpine environment.

- \* The combination of spatial and temporal scales of melting layer variability. From observational data it was inferred that whereas on the Swiss plateau the assumption of pure advection seems adequate, the small-scale topography does not allow to link spatial and temporal scales of melting layer variability in the Swiss Alps.
- \* A framework for the inclusion of information on hydrometeor classes and the application of machine learning algorithms to the study of the vertical structure of precipitation. It was found that models which included information on hydrometeor proportions better represented the observed patterns of vertical growth and decay of precipitation.
- \* A more localised vertical profile correction technique exploiting the polarimetric capabilities of the radar network through the inclusion of hydrometeor proportions. It was shown that for a given error, the artificial neural network model trained with hydrometeor proportions can predict from altitudes between 500 to 1000 metres higher than the model based on only reflectivity data.

### 5.3 Perspectives

Many aspects of the research presented in this thesis deserve further attention and development. The radar hardware monitoring using a single bright scatterer for example, would benefit from the analysis of more events. The difficulty here is partly in finding periods of four uninterrupted clear-sky days in the radar repository, especially because high resolution radar data of clear-sky events is not stored indefinitely due to the costs related to data storage. Further research should also be conducted on the stability of the signals in continuous rain, although four consecutive days of uninterrupted precipitation is such a rare event in the study region that such an analysis would probably have to be performed on smaller temporal scales. From a more technical point of view, the relationship between the noise source signal and the reflectivity measurements as well as the response of the low noise amplifiers to variations in temperature, more specifically daily temperature cycles, deserves further testing. Finally, the improved knowledge of the signature of the bright scatterer in clear-sky conditions may allow for the analysis of particular case studies and perhaps even the quantification of melting layer attenuation.

The characterisation of the melting layer variability presented in chapter 3 is restricted to the two Swiss locations at which the measurement campaigns were conducted with a mobile X-band radar (Payerne and Martigny). Although Payerne could be considered representative for conditions on the Swiss plateau, the data from the measurement campaign covered a period from March 2014 until May 2014 and thus did not include winter time conditions at this location. The campaign conducted in the Swiss Alps covered winter and spring conditions

in a very deep and long Alpine valley. Though it can not be argued that this location was representative for all Alpine valleys, performing a similar measurement campaign elsewhere would be complicated by topography: in smaller valleys the radar would likely not have an unimpeded view over sufficiently long ranges. For the same reasons, the results of the presented chapter 3 are also restricted to temporal scales of up to 3 hours and spatial scales of 20 km and less. Performing the analysis on the operational C-band radar data would not only allow for the description of the melting layer variability at much larger spatial and temporal scales, but also constitute a more representative characterisation for Switzerland. However such an endeavor would require the application of a melting layer detection algorithm to PPI scans and although such algorithms exist, the edges of the melting layer are much less clear and well-defined in the PPI scans. Furthermore, the data from the operational C-band radars, although available for much longer spatial ranges, is also subject to beam broadening and a decrease in resolution with distance such that it would still constrain the maximum range up to which the analysis could be performed. Finally, the altitudes of the operational C-band radars which are located in the Alps ( $> 2850$  m a.s.l.) means that these will practically always measure above or within the melting layer.

The localised vertical profile correction technique described in chapter 4 along with the developed framework for the application of machine learning algorithms and the inclusion of other (polarimetric) variables to the study of the vertical structure of precipitation opens up many perspectives for further analysis. Firstly, the analysis of the contributions of the input variables (predictors) would provide even more information on the relevance of (combinations of) hydrometeor classes and the different height levels. There are more and less complicated ways to tackle this problem and while simple solutions (such as performing predictions while randomising each of the variables in turn) may not be able to fully take into account the complex non-linear relationships between the variables, more complex methods (such as recursive feature elimination) requires many iterations for the training of the neural networks and are thus computationally more expensive. Similarly, a full sensitivity analysis of the obtained results with respect to the chosen cone parameters (diameters of the base and top, vertical resolution and the grid spacing of the cone locations) for example, was outside of the scope of the presented study. And although the choices in the parameters were subject to many constraints related to processing time, the resolution of the radar measurements and visibility at lower height levels, it would be valuable to estimate the optimal cone parameters within these constraints. Naturally, the current dataset of 30 precipitation events could be further extended and other machine learning methods such as convolutional neural networks or random forests may be applied to the data. Part of the objective of this study was to better exploit the polarimetric capabilities of the radar network, and this was done indirectly by including information hydrometeor proportions. The inclusion of polarimetric variables, other radar derived products or information from other instruments (i.e. satellite data) or meteorological models is also among the possibilities for future work. The verification of the proposed vertical profile correction technique was done by adding the predicted change in reflectivity to the lowest observed reflectivity measurement. The thus obtained predicted

values could be compared with the observed reflectivity values at the ground level and also with other, more traditional profile correction techniques. It would be interesting to also evaluate the performance of the correction schemes by comparing them with rain gauge estimates at the ground level. In this case, a rainfall rate calculated on the basis of the predominant hydrometeor class could substitute the reflectivity-rainfall rate relationship. Finally, one of the motivations for the presented study was the extrapolation of high-altitude radar measurements to the ground level. An interesting extension of this work would be to apply the correction technique to data from one of the high-altitude radars. For the Plaine Morte radar based in the Valais, the correction technique could be verified with the X-band radar scans from the 2016-2017 winter campaign presented in chapter 3.

In terms of the improvement of the current operational QPE and VPR correction techniques, this thesis has opened up some new perspectives. Notably, it appears that the variability of the melting layer and thus the vertical structure of precipitation is more important at small (15 to 10 km) spatial scales in an Alpine environment than in a flat area. In practice this means that the meso-beta profile which is extracted within a range of 70 km from the radar and integrated over a few hours will not capture well enough the spatio-temporal variability of the precipitation in the Alpine environment. The more localised correction approach proposed in this thesis has the merit of applying the vertical profile corrections at the 10 km scale and has further demonstrated the additional value of including polarimetric information through the use of hydrometeor proportions. However, the requirements for operational use are stringent and so the potential of the proposed method should also be evaluated in the light of these requirements. Firstly, any operational correction method should be able to function at all times. The method based on the vertical cone correction for example could fail if for some reason one of the polarimetric variables is unavailable or compromised. One way to assure that a profile correction can always be applied in current strategies is through the inclusion of a climatological profile. In the case of the vertical cone correction, the dBZ-only model could substitute the HC + dBZ-only model when necessary. A potential limitation of such a change between models is that it may lead to some discontinuities from one radar image to the next, and some aggregation in time may be needed to resolve such issues. Also, at time  $t_0$  some profile would have to be used as a first guess and the vertical cone correction technique does not propose such a profile yet. In terms of processing costs, once the cones are extracted and the model is trained, the application of the ANN models to existing data should be relatively fast. Since average reflectivity values and hydrometeor proportions have been used, the model could be applied at different spatial scales. It may even be considered to apply the correction to larger scales in some regions such as the Swiss plateau and to smaller scales in other regions such as the Alps.



## A Calculation of refractivity

As the radar beam propagates through the atmosphere it is both attenuated and refracted. Variations in the refractive index  $n$  of the atmosphere cause for the beam to change direction. Because this change in refractive index usually occurs gradually with height above the surface, this also causes for the beam to curve gradually. The refractive index is defined as the ratio of the speed of light in vacuum  $c$  and the phase velocity of light in the medium (in this case the atmosphere)  $v$ , and is thus dimensionless. In this study pressure, air temperature and relative humidity measurements from meteorological ground stations were used to calculate the refractive index:

$$n = 1 + 10^{-6} * \left( \frac{0.776 * P}{T} + \frac{3.73 * 10^3 * Pw}{T^2} \right) \quad (\text{A.1})$$

where the first term is known as the “dry” term and the second as the “wet” term,  $P$  is the atmospheric pressure in Pa,  $T$  is the absolute temperature in K and  $Pw$  is the vapour partial pressure in Pa calculated using:

$$Pw = \frac{RH}{100} * e^{77.3450 + 0.0057 * T - 7235/T} / T^{8.2} \quad (\text{A.2})$$

where  $RH$  is the relative humidity. Typical values for  $n$  near sea level are around 1.0003, or 300 ppm over 1. This is only slightly larger than unity and it is therefore deemed more practical to use refractivity  $N$  which is the exceedance from unity of the refractive index, amplified by 60 dB:

$$N = (n - 1) * 10^6 \quad (\text{A.3})$$

## Appendix A. Calculation of refractivity

---

Normally,  $N$  decreases with height in the atmosphere leading to a downward bending of the radar beam. In order to calculate the variation of  $N$  with height ( $dN/dh$ ), the refractivity values were calculated for various ground stations located at different altitudes surrounding Cimetta. For more details on refractivity calculations and beam propagation the reader is referred to [Kerr \(1987\)](#).

# Bibliography

- Andrieu, H. and Creutin, J. D. (1995). Identification of Vertical Profiles of Radar Reflectivity for Hydrological Applications Using an Inverse Method. Part I: Formulation. *J. Appl. Meteorol*, 34(1):225–239.
- Andrieu, H., Delrieu, G., and Creutin, J. D. (1995). Identification of Vertical Profiles of Radar Reflectivity For Hydrological Applications Using on Inverse Method. Part 2: Sensitivity Analysis And Case-Study. *J. Appl. Meteorol*, 34(1):240–259.
- Arent, D. J., Tol, R. S., Faust, E., Hella, J. P., Kumar, S., Strzepek, K. M., Tóth, F. L., and Yan, D. (2014). Key economic sectors and services. In *Climate Change 2014 Impacts, Adaptation and Vulnerability: Part A: Global and Sectoral Aspects. Contribution of Working Group II to the Fifth Assessment Report of the Intergovernmental Panel on Climate Change*, pages 659–708. Cambridge University Press, Cambridge, United Kingdom and New York, NY, USA.
- Atlas, D. (2002). Radar calibration some simple approaches. *B. Am. Meteorol. Soc.*, 83(9):1313–1316.
- Atlas, D. and Mossop, S. C. (1960). Calibration of a weather radar by using standard target. *B. Am. Meteorol. Soc.*, 41(7):377–382.
- Battan, L. J. (1973). *Radar observation of the atmosphere*. University of Chicago Press.
- Beard, K. V., Bringi, V. N., and Thurai, M. (2010). A new understanding of raindrop shape. *Atmos. Res.*, 97(4):396–415.
- Beard, K. V. and Chuang, C. (1987). A new model for the equilibrium shape of raindrops. *J. Atmos. Sci*, 44(11):1509–1524.
- Bell, C. (2000). *Detection of the Riming Process with a Vertically Pointing Radar*. PhD thesis, McGill University, Montreal, Quebec.
- Bellon, A., Lee, G., and Zawadzki, I. (2005). Error statistics of VPR corrections in stratiform precipitation. *J. Appl. Meteorol*, 44(7):998–1015.
- Beniston, M. (2005). The risks associated with climatic change in mountain regions. In Huber, U., Bugmann, H., and Reasoner, M., editors, *Global Change and Mountain Regions: An Overview of Current Knowledge*, pages 511–519. Springer Netherlands, Dordrecht.

## Bibliography

---

- Beniston, M., Stoffel, M., and Hill, M. (2011). Impacts of climatic change on water and natural hazards in the Alps: Can current water governance cope with future challenges? Examples from the European "ACQWA" project. *Environmental Science and Policy*, 14:734–743.
- Berne, A., Delrieu, G., Andrieu, H., and Creutin, J. D. (2004). Influence of the Vertical Profile of Reflectivity on Radar-Estimated Rain Rates at Short Time Steps. *J. Hydrometeor.*, 5(2):296–310.
- Besic, N., Figueras i Ventura, J., Grazioli, J., Gabella, M., Germann, U., and Berne, A. (2016). Hydrometeor classification through statistical clustering of polarimetric radar measurements: A semi-supervised approach. *Atmos. Meas. Tech.*, 9(9):4425–4445.
- Besic, N., Gehring, J., Praz, C., Figueras i Ventura, J., Grazioli, J., Gabella, M., Germann, U., and Berne, A. (2018). Unraveling hydrometeor mixtures in polarimetric radar measurements. *Atmos. Meas. Tech.*, 11(8):4847–4866.
- Boodoo, S., Hudak, D., Donaldson, N., and Leduc, M. (2010). Application of dual-polarization radar melting-layer detection algorithm. *J. Appl. Meteorol. Clim.*, 49(8):1779–1793.
- Borowska, L. and Zrnic, D. (2012). Use of ground clutter to monitor polarimetric radar calibration. *J. Atmos. Oceanic Technol.*, 29(2):159–176.
- Bowler, N. E., Pierce, C. E., and Seed, A. W. (2006). STEPS: A probabilistic precipitation forecasting scheme which merges an extrapolation nowcast with downscaled NWP. *Q. J. Roy. Meteor. Soc.*, 132(620):2127–2155.
- Brandes, E. A. and Ikeda, K. (2004). Freezing-Level Estimation with Polarimetric Radar. *J. Appl. Meteor.*, 43(11):1541–1553.
- Bringi, V. N. and Chandrasekar, V. (2001). *Polarimetric Doppler Weather Radar : Principles and Applications*. Cambridge University Press, Cambridge, United Kingdom, revised edition.
- Campbell, L. S. and Steenburgh, W. J. (2014). Finescale Orographic Precipitation Variability and Gap-Filling Radar Potential in Little Cottonwood Canyon, Utah. *Weather Forecast*, 29(4):912–935.
- Chen, W.-K. (2013). *The Electrical engineering handbook*. Academic Press.
- Cluckie, I. D., Griffith, R. J., Lane, A., and Tilford, K. A. (2000). Radar hydrometeorology using a vertically pointing radar. *Hydrol. Earth. Syst. Sc*, 4(4):565–580.
- Colle, B. A., Garvert, M. F., Wolfe, J. B., Mass, C. F., and Woods, C. P. (2005a). The 13 – 14 December 2001 IMPROVE-2 Event. Part II : Comparisons of MM5 Model. *J. Atmos. Sci*, 62(10):3535–3558.
- Colle, B. A., Smith, R. B., and Wesley, D. A. (2013). Theory, Observations, and Predictions of Orographic Precipitation. In Chow, F. K., De Wekker, S. F., and Snyder, B. J., editors, *Mountain Weather Research and Forecasting: Recent Progress and Current Challenges*, pages 291–344. Springer Netherlands, Dordrecht.

- Colle, B. A., Wolfe, J. B., Steenburgh, W. J., Kingsmill, D. E., Cox, J. A. W., and Shafer, J. C. (2005b). High-Resolution Simulations and Microphysical Validation of an Orographic Precipitation Event over the Wasatch Mountains during IPEX IOP3. *Mon. Weather. Rev.*, 133(10):2947–2971.
- Colle, B. A. and Zeng, Y. (2004a). Bulk microphysical sensitivities within the MM5 for orographic precipitation. Part I: The Sierra 1986 event. *Mon. Weather. Rev.*, 132(12):2780–2801.
- Colle, B. A. and Zeng, Y. (2004b). Bulk Microphysical Sensitivities within the MM5 for Orographic Precipitation. Part II: Impact of Barrier Width and Freezing Level. *Mon. Weather. Rev.*, 132(12):2802–2815.
- Crane, R. K. (1980). A review of radar observations of turbulence in the lower stratosphere. *Radio Sci.*, 15(2):177–193.
- Cybenko, G. (1989). Approximation by Superpositions of a Sigmoidal Function. *Math. Control. Signal.*, 2:303–314.
- Das, S., Maitra, A., and Shukla, A. K. (2011). Melting layer characteristics at different climatic conditions in the Indian region: Ground based measurements and satellite observations. *Atmos. Res.*, 101(1-2):78–83.
- Davis, A., Marshak, A., Wiscombe, W., and Cahalan, R. (1996). Scale Invariance of Liquid Water Distributions in Marine Stratocumulus. Part I: Spectral Properties and Stationarity Issues. *J. Atmos. Sci.*, 53:1538–1558.
- De Montera, L., Barthès, L., Mallet, C., and Golé, P. (2009). The Effect of Rain–No Rain Intermittency on the Estimation of the Universal Multifractals Model Parameters. *J. Hydrometeor.*, 10(2):493–506.
- Delrieu, G., Caoudal, S., and Creutin, J. D. (1997). Feasibility of using mountain return for the correction of ground-based X-band weather radar data. *J. Atmos. Oceanic Technol.*, 14(3):368–385.
- Dixon, M. J., Hubbert, J. C., and Ellis, S. (2017). A ZDR Calibration Check using Hydrometeors in the Ice Phase. In *AMS 38th Conference on Radar Meteorology*, 28 August-1 September, Chicago (USA).
- Doviak, R. J. and Zrnić, D. S. (2006). *Doppler radar and weather observations, second edition*. Dover Publications.
- Fabry, F. (2004). Meteorological Value of Ground Target Measurements by Radar. *J. Atmos. Oceanic Technol.*, 21:560–573.
- Fabry, F. (2015). *Radar Meteorology; principles and practice*. Cambridge University Press.

## Bibliography

---

- Fabry, F., Bellon, A., Duncan, M. R., and Austin, G. L. (1994a). High resolution rainfall measurements by radar for very small basins: the sampling problem reexamined. *J. Hydrol*, 161(1-4):415–428.
- Fabry, F., Bellon, A., and Zawadzki, I. (1994b). Long Term Observations of the Melting Layer Using Vertically Pointing Radars. Technical Report MW-101, August, Cooperative Centre for Research in Mesometeorology, Montréal.
- Fabry, F. and Zawadzki, I. (1995). Long-term radar observations of the melting layer of precipitation and their interpretation. *J. Atmos. Sci*, 52:838–851.
- Figueras i Ventura, J., Leuenberger, A., Kuensch, Z., Grazioli, J., and Germann, U. (2017). Pyrad: A Real-Time Weather Radar Data Processing Framework Based on Py-ART. In *38th AMS Conference on Radar Meteorology*, 28 August - 1 September 2017, Chicago, IL (USA).
- Figueras i Ventura, J., Schneebeli, M., Leuenberger, A., Gabella, M., Grazioli, J., Raupach, T. H., Wolfensberger, D., Graf, P., Wernli, H., Berne, A., and Germann, U. (2015). The PARADISO campaign: Description and first results. In *AMS: 37th Conference on Radar Meteorology*, page 11B.3, 14 - 18 September, Norman, OK (USA).
- Fraedrich, K. and Larnder, C. (1993). Scaling regimes of composite rainfall time series. *Tellus A*, 45(4):289–298.
- Frei, C. and Schär, C. (1998). A precipitation climatology of the Alps from high-resolution rain-gauge observations. *Int. J. Climatol.*, 18(8):873–900.
- Frei, C., Schöll, R., Fukutome, S., Schmidli, J., and Vidale, P. L. (2006). Future change of precipitation extremes in Europe: Intercomparison of scenarios from regional climate models. *J. Geophys. Res. Atmos*, 111(D6).
- Gabella, M. (2018). On the Use of Bright Scatterers for Monitoring Doppler , Dual-Polarization Weather Radars. *Remote Sens.*, 10(1007):1–14.
- Gabella, M., Boscacci, M., Sartori, M., and Germann, U. (2016). Calibration accuracy of the dual-polarization receivers of the C-band swiss weather radar network. *Atmosphere*, 7(76).
- Gabella, M., Morin, E., Leuenberger, A., Notarpietro, R., Branca, M., Figueras, J., Schneebeli, M., and Germann, U. (2014). High temporal resolution radar observations of various scatterers in the atmosphere at 10 GHz: experiences in Mediterranean semi-arid regions and in the western Alps. In *WMO Technical conference on Meteorological and Environmental instruments and methods of observation, Developments in observing technologies*, 7-9 July, Saint Petersburg (Russia).
- Gabella, M., Sartori, M., Boscacci, M., and Germann, U. (2015). Vertical and horizontal polarization observations of slowly varying solar emissions from operational swiss weather radars. *Atmosphere*, 6(1):50–59.

- Germann, U. (2000). *Spatial Continuity of Precipitation, Profiles of Radar Reflectivity and Precipitation Measurements in the Alps*. PhD thesis, Swiss Federal Institute of Technology (ETH).
- Germann, U., Boscacci, M., Gabella, M., and Sartori, M. (2015). Peak Performance; radar design for prediction in the Swiss Alps. *Meteorological Technology International*, pages 42–45.
- Germann, U., Galli, G., Boscacci, M., and Bolliger, M. (2006). Radar precipitation measurement in a mountainous region. *Q. J. Roy. Meteor. Soc.*, 132(618):1669–1692.
- Germann, U. and Joss, J. (2001). Variograms of radar reflectivity to describe the spatial continuity of Alpine precipitation. *J. Appl. Meteor.*, 40(6):1042–1059.
- Germann, U. and Joss, J. (2002). Mesobeta profiles to extrapolate radar precipitation measurements above the Alps to the ground level. *J. Appl. Meteor.*, 41:542–557.
- Germann, U. and Joss, J. (2004). *Operational Measurement of Precipitation in Mountainous Terrain*, chapter 2, pages 52–77. Springer Berlin Heidelberg.
- Gleick, P. H. and Heberger, M. (2014). Water Conflict Chronology. In *The World's Water*. Pacific Institute.
- Gorgucci, E., Scarchilli, G., and Chandrasekar, V. (1999). A procedure to calibrate multi-parameter weather radar using properties of the rain medium. *IEEE T. Geosci. Remote.*, 37(1):269–276.
- Gourley, J. J., Tabary, P., and Parent du Chatelet, J. (2006). Data quality of the Meteo-France C-band polarimetric radar. *J. Atmos. Oceanic Technol.*, 23(10):1340–1356.
- Gray, W. R., Uddstrom, M. J., and Larsen, H. R. (2002). Radar surface rainfall estimates using a typical shape function approach to correct for the variations in the vertical profile of reflectivity. *Int. J. Remote. Sens*, 23(12):2489–2504.
- Grazioli, J., Tuia, D., and Berne, A. (2015). Hydrometeor classification from polarimetric radar measurements: A clustering approach. *Atmospheric Measurement Techniques*, 8(1):149–170.
- Harris, D., Foufoula-Georgiou, E., Droegemeier, K. K., and Levit, J. J. (2001). Multiscale Statistical Properties of a High-Resolution Precipitation Forecast. *J. Hydrometeorol*, 2(4):406–418.
- Harris, D., Seed, A., Menabde, M., and Austin, G. (1997). Factors affecting multiscaling analysis of rainfall time series. *Nonlinear. Proc. Geoph*, 4(3):137–155.
- Harris, G. N., Bowman, K. P., and Shin, D. B. (2000). Comparison of freezing-level altitudes from the NCEP reanalysis with TRMM precipitation radar brightband data. *J. Climate*, 13(23):4137–4148.

## Bibliography

---

- Harrison, D. L., Driscoll, S. J., and Kitchen, M. (2000). Improving precipitation estimates from weather radar using quality control and correction techniques. *Meteorol. Appl.*, 6:135–144.
- Helmus, J. J. and Collis, S. M. (2016). The Python ARM Radar Toolkit (Py-ART), a Library for Working with Weather Radar Data in the Python Programming Language. *Journal of open research software*, 4(e25).
- Hill, F. F. (1983). The use of annual average rainfall to derive estimates of orographic enhancement over England and Wales for different wind directions. *J. Clim.*, 3:113–129.
- Holleman, I., Huuskonen, A., Gill, R., and Tabary, P. (2010). Operational monitoring of radar differential reflectivity using the sun. *J. Atmos. Oceanic Technol.*, 27(5):881–887.
- Hornik, K., Stinchcombe, M., and White, H. (1989). Multilayer Feedforward Networks are Universal Approximators. *Neural Networks*, 2(359–366).
- Houze, R. A. (2012). Orographic effects on precipitating clouds. *Rev. Geophys.*, 50(1):1–47.
- Houze, R. A. and Medina, S. (2005). Turbulence as a Mechanism for Orographic Precipitation Enhancement. *J. Atmos. Sci.*, 62(10):3599–3623.
- Hubbert, J. C., Bringi, V. N., and Brunkow, D. (2003). Studies of the polarimetric covariance matrix. Part I: Calibration methodology. *J. Atmos. Oceanic Technol.*, 20(5):696–706.
- Huuskonen, A., Kurri, M., and Holleman, I. (2016). Improved analysis of solar signals for differential reflectivity monitoring. *Atmos. Meas. Tech.*, 9(7):3183–3192.
- IPCC (2018). Global Warming of 1.5°C. Summary for Policymakers. In *An IPCC Special Report on the impacts of global warming of 1.5°C above pre-industrial levels and related global greenhouse gas emission pathways, in the context of strengthening the global response to the threat of climate change, sustainable development*, page 32. World Meteorological Organization, Geneva, Switzerland.
- Jarvis, A., Reuter, H., Nelson, A., and Guevara, E. (2008). Hole-filled seamless SRTM data V4. Tech. rep., International Centre for Tropical Agriculture (CIAT).
- Joe, P. and Smith, P. L. (2001). Summary of the Radar Calibration Workshop. In *AMS 30th Conference on Radar Meteorology*, 19–24 July 2001, Munich (Germany).
- Jordan, P., Seed, A., and Austin, G. (2000). Sampling errors in radar estimates of rainfall. *J. Geophys. Res.*, 105(D2):2247–2257.
- Joss, J. and Lee, R. (1995). The Application of Radar-Gauge Comparisons to Operational Precipitation Profile Corrections. *J. Appl. Meteor.*, 34(12):2612–2630.
- Joss, J. and Pittini, A. (1991). Real-time estimation of the vertical profile of radar reflectivity to improve the measurement of precipitation in an Alpine region. *Meteorol. Atmos. Phys.*, 47(1):61–72.



- Joss, J. and Waldvogel, A. (1990). Precipitation measurement and hydrology. In Atlas, D., editor, *Radar in Meteorology: Battan Memorial and 40th Anniversary Radar Meteorology Conference*, pages 557–606, November 9 - 13, Boston, MA (USA). American Meteorological society.
- Kanevski, M., Pozdnoukhov, A., and Timonin, V. (2009). *Machine Learning for Spatial Environmental Data*. Presses polytechniques et universitaires romandes, Lausanne.
- Kerr, D. (1987). *Propagation of short radio waves (Revised edition)*. Stevenage Herts England Peter Peregrinus Ltd.
- Kirstetter, P. E., Andrieu, H., Boudevillain, B., and Delrieu, G. (2013). A Physically based identification of vertical profiles of reflectivity from volume scan radar data. *J. Appl. Meteorol. Clim*, 52(7):1645–1663.
- Kitchen, M., Brown, R., and Davies, A. G. (1994). Real-time correction of weather radar data for the effects of bright band, range and orographic growth in widespread precipitation. *Quart. J. Roy. Meteor. Soc*, 120:1231–1254.
- Kohler, T., Wehrli, A., and Jurek, M. (2014). *Mountains and climate change: A global concern. Sustainable Mountain Development Series*. Bern, Switzerland, Centre for Development and Environment (CDE), Swiss Agency for Development and Cooperation (SDC) and Geographica Bernensia.
- Koistinen, J. (1991). Operational correction of radar rainfall errors due to the radar reflectivity profile. In *Proceedings of the 25th International Conference on Radar Meteorology*, pages 91–94, 24-28 June, Paris (France). American Meteorological Society.
- Koistinen, J., Michelson, D. B., Hohti, H., and Peura, M. (2004). *Operational Measurement of Precipitation in Cold Climates*, chapter 3, pages 78–110. Springer Berlin Heidelberg.
- Lumb, F. (1983). Sharp snow-rain contrasts-an explanation. *Weather*, 38:71–73.
- Mandapaka, P. V., Lewandowski, P., Eichinger, W. E., and Krajewski, W. F. (2009). Multiscaling analysis of high resolution space-time lidar-rainfall. *Nonlinear. Proc. Geoph*, 16:579–586.
- Marigo, G., Robert-Luciani, T., and Crepaz, A. (2008). Snow level forecasting methods and parameters: two practical examples on eastern Italian Alps. In *13th Mtn. Meteor. Conf.*, Whistler, Canada.
- Marshall, J. S., Langille, R. C., and Palmer, W. M. (1947). Measurement of rainfall by radar. *J. Meteorol*, 4:186–192.
- Marshall, J. S. and Palmer, W. M. K. (1948). The Distribution of raindrops with size. *Journal of Meteorology*, 5:165–166.
- Marwitz, J. (1983). The kinematics of orographic flow during Sierra storms. *J. Atmos. Sci*, 40:1218–1227.

## Bibliography

---

- Matrosov, S. Y., Clark, K. A., and Kingsmill, D. E. (2007). A polarimetric radar approach to identify rain, melting-layer, and snow regions for applying corrections to vertical profiles of reflectivity. *J. Appl. Meteorol. Clim*, 46(2):154–166.
- Matsuo, T. and Sasyo, Y. (1981). Melting of Snowflakes below Freezing Level in the Atmosphere. *J. Meteorol. Soc. Jpn*, 59(1):10–25.
- Medina, S., Smull, B. F., Houze, R. a., and Steiner, M. (2005). Cross-Barrier Flow during Orographic Precipitation Events: Results from MAP and IMPROVE. *J. Atmos. Sci*, 62(1985):3580–3598.
- Melnikov, V., Zrnica, D., Free, A., Ice, R., and Macemon, R. (2017). Monitoring Radar Calibration using Ground Clutter. Technical Report September, National Severe Storms Laboratory, Norman, Oklahoma.
- Melnikov, V. M., Zrnica, D. S., Doviak, R. J., and Carter, J. K. (2003). Calibration and Performance Analysis of NSSL's Polarimetric WSR-88D. Technical report, National Severe Storms Laboratory, Norman, Oklahoma.
- Meneghini, R., Eckerman, J., and Atlas, D. (1983). Determination of Rain Rate from a Spaceborne Radar Using Measurements of Total Attenuation. *IEEE T. Geosci. Remote.*, GE-21(1):34–43.
- Meneghini, R., Iguchi, T., Kozu, T., Liao, L., Okamoto, K., Jones, J. a., and Kwiatkowski, J. (2000). Use of the Surface Reference Technique for Path Attenuation Estimates from the TRMM Precipitation Radar. *J. Appl. Meteorol*, 39:2053–2070.
- MeteoSwiss (2016). A modern radar network for Switzerland. Technical report, Federal Office for Meteorology and Climatology MeteoSwiss.
- Mittermaier, M. P. and Illingworth, A. J. (2003). Comparison of model-derived and radar-observed freezing-level heights: Implications for vertical reflectivity profile-correction schemes. *Q. J. R. Meteorol. Soc.*, 129(587):83–95.
- Mohymont, B. and Delobbe, L. (2008). Is the variogram a good tool for assessing the spatial variability of vertical profiles of reflectivity? In *ERAD*, 30 June - 4 July, Helsinki (Finland).
- Montopoli, M., Roberto, N., Adirosi, E., Gorgucci, E., and Baldini, L. (2017). Investigation of weather radar quantitative precipitation estimation methodologies in complex orography. *Atmosphere*, 8(2).
- Mountain Agenda (1998). Mountains of the world: Water towers for the 21st century.
- NCCS (2018). CH2018 - Climate Scenarios for Switzerland. Technical report, National Centre for Climate Services, Zurich.

- Nerini, D., Besic, N., Sideris, I., Germann, U., and Foresti, L. (2017). A non-stationary stochastic ensemble generator for radar rainfall fields based on the short-space Fourier transform. *Hydrol. Earth. Syst. Sc.*, 21(6):2777–2797.
- Nitu, R., Roulet, Y.-A., Wolff, M., Earle, M., Reverdin, A., Smith, C., Kochendorfer, J., Morin, S., Rasmussen, R., Wong, K., Alastrué, J., Arnold, L., Baker, B., Buisán, S., Collado, J., Colli, M., Collins, B., Gaydos, A., Hannula, H.-R., Hoover, J., Joe, P., Kontu, A., Laine, T., Lanza, L., Lanzinger, E., Lee, G., Lejeune, Y., Leppänen, L., Mekis, E., Panel, J.-M., Poikonen, A., Ryu, S., Sabatini, F., Theriault, J., Yang, D., Genthon, C., van den Heuvel, F., Hirasawa, N., Konishi, H., Motoyoshi, H., Nakai, S., Nishimura, K., Senese, A., and Yamashita, K. (2018). WMO Solid Precipitation Intercomparison Experiment (SPICE) (2012 - 2015). Technical report, World Meteorological Organization, Geneva.
- Nykanen, D. K. (2008). Linkages between Orographic Forcing and the Scaling Properties of Convective Rainfall in Mountainous Regions. *J. Hydrometeorol.*, 9(3):327–347.
- Nykanen, D. K. and Harris, D. (2003). Orographic influences on the multiscale statistical properties of precipitation. *J. Geophys. Res.*, 108(D8):8381.
- Praz, C., Roulet, Y. A., and Berne, A. (2017). Solid hydrometeor classification and riming degree estimation from pictures collected with a Multi-Angle Snowflake Camera. *Atmos. Meas. Tech.*, 10(4):1335–1357.
- Purdy, J. C., Harris, D., Austin, G. L., Seed, A. W., and Gray, W. (2001). A case study of orographic rainfall processes incorporating multiscaling characterization techniques. *J. Geophys. Res. Atmos.*, 106(D8):7837–7845.
- Rinehart, R. E. (1978). On the Use of Ground Return Targets for Radar Reflectivity Factor Calibration Checks. *J. Appl. Meteor.*, 17:1342–1350.
- Rinehart, R. E. (2004). *Radar for Meteorologists*. Rinehart, 5 edition.
- Rinehart, R. E. and Frush, C. L. (1983). Comparison of antenna beam patterns obtained from near-field test measurements and ground target scans. In *AMS 21st Conference on Radar Meteorology*, pages 291–295, 19–23 September 1983, Edmonton, AB (Canada).
- Roe, G. H. (2005). Orographic Precipitation. *Annu. Rev. Earth. Pl. Sc.*, 33(1):645–671.
- Rudolph, J. V. and Friedrich, K. (2013). Seasonality of vertical structure in radar-observed precipitation over southern Switzerland. *J. Hydrometeorol.*, 14(1):318–330.
- Rudolph, J. V. and Friedrich, K. (2014). Dynamic and thermodynamic predictors of vertical structure in radar-observed regional precipitation. *J. Climate*, 27(5):2143–2158.
- Rysman, J. F., Verrier, S., Lemaître, Y., and Moreau, E. (2013). Space-time variability of the rainfall over the western Mediterranean region: A statistical analysis. *J. Geophys. Res. Atmos.*, 118(15):8448–8459.

## Bibliography

---

- Ryzhkov, A. V., Giangrande, S. E., Melnikov, V. M., and Schuur, T. J. (2005). Calibration issues of dual-polarization radar measurements. *J. Atmos. Oceanic Technol.*, 22(8):1138–1155.
- Šálek, M., Cheze, J.-L., Handwerker, J., Delobbe, L., and Uijlenhoet, R. (2004). Radar techniques for identifying precipitation type and estimating quantity of precipitation. Technical report, Document of COST Action 717, W G 1.
- Schneebeli, M., Dawes, N., Lehning, M., and Berne, A. (2013). High-resolution vertical profiles of X-band polarimetric radar observables during snowfall in the Swiss Alps. *J. Appl. Meteor. Climatol.*, 52(2):378–394.
- Schneebeli, M., Grazioli, J., and Berne, A. (2014). Improved Estimation of the Specific Differential Phase Shift Using a Compilation of Kalman Filter Ensembles. *IEEE T GEOSCI REMOTE*, 52(8):5137–5149.
- Seliga, T. A. and Bringi, V. N. (1976). Potential Use of Radar Differential Reflectivity Measurements at Orthogonal Polarizations for Measuring Precipitation. *J. Appl. Meteor.*, 15:69–76.
- Silberstein, D. S., Wolff, D. B., Marks, D. A., Atlas, D., and Pippitt, J. L. (2008). Ground clutter as a monitor of radar stability at Kwajalein, RMI. *J. Atmos. Oceanic Technol.*, 25(11):2037–2045.
- Smith, B. (2003). Accuracy and resolution of shuttle radar topography mission data. *Geophys. Res. Lett.*, 30(9):1467.
- Stoelinga, M. T., Stewart, R. E., Thompson, G., and Thériault, J. M. (2013). Microphysical Processes Within Winter Orographic Cloud and Precipitation Systems. In Chow, F. K., De Wekker, S. E., and Snyder, B. J., editors, *Mountain Weather Research and Forecasting: Recent Progress and Current Challenges*, pages 345–408. Springer Netherlands, Dordrecht.
- Stull, R. B. (1988). *An Introduction to Boundary Layer Meteorology*. Springer, Dordrecht.
- Testud, J., Bouar, E. L., Obligis, E., and Ali-Mehenni, M. (2000). The rain profiling algorithm applied to polarimetric weather radar. *J. Atmos. Oceanic Technol.*, 17(3):332–356.
- Thurai, M., Deguchi, E., Iguchi, T., and Okamoto, K. (2003). Freezing height distribution in the tropics. *Int. J. Satell. Co. Netw.*, 21(6):533–545.
- Van der Hoven, I. (1957). Power spectrum of horizontal wind speed in the frequency range from 0.0007 to 900 cycles per hour. *J. Meteorol.*, 14(2):160–164.
- Vaughan, D., Comiso, J., Allison, I., Carrasco, J., Kaser, G., Kwok, R., Mote, P., Murray, T., Paul, F., Ren, J., Rignot, E., Solomina, O., Steffen, K., and Zhang, T. (2013). Observations: Cryosphere. In *Climate Change 2013: The Physical Science Basis. Contribution of Working Group I to the Fifth Assessment Report of the Intergovernmental Panel on Climate Change*. IPCC.
- Verrier, S., Mallet, C., and Barthès, L. (2011). Multiscaling properties of rain in the time domain, taking into account rain support biases. *J. Geophys. Res. Atmos.*, 116(20).

- Vignal, B., Andrieu, H., and Creutin, J. D. (1999). Identification of Vertical Profiles of Reflectivity from Volume Scan Radar Data. *J. Appl. Meteorol.*, 38:1214–1228.
- Vignal, B., Galli, G., Joss, J., and Germann, U. (2000). Three methods to determine profiles of reflectivity from volumetric radar data to correct precipitation estimates. *J. Appl. Meteorol.*, 39(1999):1715–1726.
- Vignal, B. and Krajewski, W. F. (2001). Large-Sample Evaluation of Two Methods to Correct Range-Dependent Error for WSR-88D Rainfall Estimates. *J. Hydrometeorol.*, 2(1994):490–504.
- Vivekanandan, J., Zrnica, D. S., Ellis, S. M., Oye, R., Ryzhkov, A. V., and Straka, J. (1999). Cloud Microphysics Retrieval Using S-Band Dual-Polarization Radar Measurements. *Bull. Amer. Met. Soc.*, 80(3):381–388.
- Vollbracht, D., Sartori, M., and Gabella, M. (2014). Absolute dual-polarization radar calibration : temperature dependence and stability with focus on antenna-mounted receivers and noise source generated reference signal. In *8th European Conference on Radar in Meteorology and Hydrology*, 1-5 September 2014, Garmisch-Partenkirchen (Germany).
- Vulpiani, G., Montopoli, M., Della Passeri, L., Gioia, A., Giordano, P., and Marzano, F. S. (2012). On the Use of Dual-Polarized C-Band Radar for Operational Rainfall Retrieval in Mountainous Areas. *J. Appl. Meteor. Climatol.*, 51.
- Weusthoff, T. (2011). Weather Type Classification at MeteoSwiss - Introduction of new automatic classification schemes. *Arbeitsberichte der MeteoSchweiz*, (235):46.
- Williams, E., Hood, K., Donovan, M., Melnikov, V., Forsyth, D., Zrnica, D., Burgess, D., Douglas, M., Sandifer, J., Saxion, D., Boydston, O., Heck, A., and Webster, T. (2013). End-to-end Calibration of NEXRAD Differential Reflectivity with Metal Spheres. In *AMS 36th Conference on Radar Meteorology*, 16-20 September 2013, Colorado (USA).
- Wolfensberger, D., Scipion, D., and Berne, A. (2016). Detection and characterization of the melting layer based on polarimetric radar scans. *Q. J. Roy. Meteor. Soc.*, 142(August):108–124.
- Wolff, D. B., Marks, D. A., and Petersen, W. A. (2015). General application of the relative calibration adjustment (RCA) technique for monitoring and correcting radar reflectivity calibration. *J. Atmos. Oceanic Technol.*, 32(3):496–506.
- Yuter, S. E. and Houze, R. A. (2003). Microphysical modes of precipitation growth determined by S-band vertically pointing radar in orographic precipitation during MAP. *Q. J. R. Meteorol. Soc.*, 129(588 PART B):455–476.
- Zhang, J. and Qi, Y. (2010). A Real-Time Algorithm for the Correction of Brightband Effects in Radar-Derived QPE. *J. Hydrometeorol.*, 11(5):1157–1171.
- Zittel, W. D., Cunningham, J. G., Lee, R. R., Richardson, L. M., Ice, R. L., and Melnikov, V. (2014). Use of Hydrometeors, Bragg Scatter, and Sun Spikes to Determine System ZDR Biases in the

## Bibliography

---

- WSR-88D Fleet. In *8th European Conference on Radar in Meteorology and Hydrology*, 1-5 September 2014, Garmisch-Partenkirchen (Germany).
- Zrnic, D. S., Balakrishnan, N., Ziegler, C. L., Bringi, V. N., Aydin, K., and Matejka, T. (1993). Polarimetric Signatures in the Stratiform Region of a Mesoscale Convective System. *J. Appl. Meteorol.*, 32(4):678–693.
- Zrnic, D. S. and Ryzhkov, A. V. (1999). Polarimetry for Weather Surveillance Radars. *B. Am. Meteorol. Soc.*, 80(3):389–406.

# Floortje Elisabeth Maria (Floor) van den Heuvel

floorvandenheuvel@hotmail.com

www.linkedin.com/in/FEMvdHeuvel

Nationality: Dutch

DOB: 04.04.1989

## Education & Experience

### June 2019 - Jan 2020

#### Editorial board member

The State of Environmental Science in Svalbard (SESS) report 2019

### June 2015 - June 2019

- Machine learning
- Geostatistics
- Signal processing
- Field work: Alps, Arctic
- Academic / Met service
- Teaching activities

#### PhD student

EPFL Remote Sensing Laboratory & MeteoSwiss (Switzerland)

Supervisors: Dr. Alexis Berne, Dr. Marco Gabella

Title: *“Statistical analysis of the spatial and temporal variability of polarimetric weather radar signals in the Alps”*

- **Teaching assistant** Geneva globals (MA), Spatial statistics and analysis (MA), Remote Sensing (BA), Probabilités et statistique (BA MATH), Introduction to environmental engineering (BA lab courses))

### May 2014 - May 2015

- International collaboration
- Data quality control

#### Internship meteorological data analysis for the WMO Solid Precipitation Intercomparison Experiment (SPICE)

MeteoSwiss (Switzerland)

### Sept 2011 - Feb 2014

- Atmospheric physics
- Climate and environmental modelling
- Interdisciplinary research

#### Msc Environmental Sciences

University of Geneva (Switzerland)

- Title Master thesis: *“Probabilities and circulation patterns related to debris-flow triggering in the Zermatt valley”*

- Supervisors: Dr. Stéphane Goyette and Dr. Markus Stoffel

### Sept 2008 - Jan 2011

#### BA International Relations and International Organisation

University of Groningen (The Netherlands)

- Title Bachelor thesis: *“The African Charter: a panacea for Africa”*

### Sept 2001 - June 2007

#### VWO Gymnasium

Maerlant Lyceum Den Haag (The Netherlands)

Specialisation in Nature and health, core courses: Physics, Mathematics, Chemistry, Biology

## Publications

---

- 2019** van den Heuvel, F., Foresti, L., Gabella, M., Germann, U., and Berne, A.: Learning about the vertical structure of radar reflectivity using hydrometeor classes and neural networks - going beyond an average profile in the Swiss Alps. *Atmospheric Measurement Techniques*, in preparation.
- 2019** van den Heuvel, F., Gabella, M., Sartori, M., and Berne, A.: Temporal monitoring of dual-polarisation weather radar using a single bright scatterer, *Journal of Atmospheric and Oceanic Technology*, in revision.
- 2018** van den Heuvel, F., Gabella, M., Germann, U., and Berne, A.: Characterisation of the melting layer variability in an Alpine valley based on polarimetric X-band radar scans, *Atmos. Meas. Tech.*, 11, 5181-5198, <https://doi.org/10.5194/amt-11-5181-2018>, 2018.
- 2018** Nitu et al.: WMO Solid Precipitation Intercomparison Experiment (SPICE) (2012-2015), World Meteorological Organization (WMO), IOM Report-No.131, [https://library.wmo.int/doc\\_num.php?explnum\\_id=5686](https://library.wmo.int/doc_num.php?explnum_id=5686), 2018.
- 2016** van den Heuvel, F., Goyette, S., Rahman, K., and Stoffel, M.: Circulation patterns related to debris-flow triggering in the Zermatt valley in current and future climates, *Geomorph.* 272, 127-136, <https://doi.org/10.1016/j.geomorph.2015.12.010>, 2016.
- 2016** (non scientific) Elégie pour l'Arctique où la glace fond si vite, *24 Heures Grand Nord project*, 12.07.2016.

### Computer skills

---

- Unix / Linux systems / Bash
- Python
- MATLAB
- IDL, R (Basic)
- ArcGIS, PostGIS, SQL
- LaTeX
- GIT

### Other skills

---

- Geostatistics
- Machine Learning
- Deployment and maintenance of instruments
- Polarimetric weather radar
- Solid precipitation measurement
- Science communication

### Languages

---

- Dutch (native)
- English (fluent)
- French (fluent)
- German (intermediate)
- Italian (beginner)

## Awards

---

- 2019** BCG PhD Scholarship and mentoring program
- 2016** Exposure Science Film Hackathon, winner (expert jury)
-





